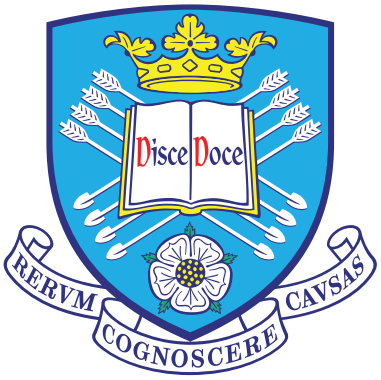

The University Of Sheffield.

Quantum Light with Quantum Dots in III-V Photonic Integrated Circuits

Towards Scalable Quantum Computing Architectures

By

JOHN O'HARA

Faculty of Science
Department of Physics and Astronomy
UNIVERSITY OF SHEFFIELD

Submitted to the University of Sheffield in partial fulfilment of the requirements for the degree of DOCTOR OF PHILOSOPHY

NOVEMBER 2017

ABSTRACT

The work in this thesis is motivated by the goal of creating scalable quantum computers, and equally by the physical understanding that develops alongside and follows from this. The fields of physics and technology are symbiotic, and quantum information processing is a prime example. The field has the potential to test quantum mechanics in new and profound ways.

Here we approach the technological problem by building upon the foundations laid by the semiconductor chip manufacturing industry. This architecture is based on the III-V semiconductors Gallium Arsenide and Indium Arsenide. Combining the two we can create chip-embedded atom-like light sources—quantum dots—that can produce quantum photonic states in lithographically etched nanoscale waveguides and cavities.

We demonstrate the integration of quantum light sources and single-mode beam splitters in the same on-chip device. These are the two primary ingredients that are needed to produce the entangled states that are the basis of this type of quantum computing.

Next we look at the quantum light source in more detail, showing that with cavity-enhancement we can significantly mitigate the detrimental dephasing associated with nanostructures. The source can be used as a means to produce coherently scattered photons in the waveguides. More importantly, the on-demand photons obtained from pulsed excitation are more indistinguishable and thus more suitable for quantum information carrying and processing. Through experiments and simulations, we investigate some aspects of single-photon sources under pulsed excitation, including emission rate, emission number probabilities, and indistinguishability. A new technique to measure very short lifetimes is demonstrated and examined theoretically.

Finally we look at preliminary steps to extend the platform further. The inclusion of photonic crystals and superconducting nanowires provides on-chip filters and detectors, and etched diode structures enable electrical excitation and tunability of the circuit components. These show some clear paths that the work can continue to evolve along.

Acknowledgements

I wish to thank the many people of LDSD, and everyone who helped me over the course of my PhD. In particular my supervisor Mark, Maurice, and postdoc Nikola, for guidance, and others I worked and argued with directly – including Chris, Rikki, Alistair, Feng, Igor, Luke, Zofia, Dom and Catherine. I thank also those who made the samples – Ed, Ben and Deivis; those who made the equipment – Paul and the workshop staff; and those who kept the sweet, sweet liquid helium forever flowing, boiling and condensing – Chris and Phil. Giuseppe attempted to teach me "many, many things", and may have succeeded once or twice, but the jury is still out. I appreciate also the efforts of our collaborators at the University of Glasgow: Robert, Robert, and Chandra. Thanks too to EPSRC for funding the research, which I hope you will find as interesting as I did.

Many others in LDSD I did not have the pleasure to work with, but rather the pleasure to not work with... I mean to say, the pleasure to appreciate the humble coffee bean and tea leaf with, and of course the barley and the grape of a Friday evening in the Uni Arms. There were many laughs and enjoyable times.

I also need to thank the people of the NHS who tidied up my unfortunate ankle more than once, after a simple problem involving mass and gravity became too much for me.

Additional thanks to Alistair and Lisa for housing me for a time, while I put some of these letters and numbers to paper.

Thanks to all my friends, some old, some new.

Lastly, and certainly not least, thanks to my parents and my sister, who encouraged and supported me throughout, as they always have.

PUBLICATIONS AND PRESENTATIONS

Aspects of the work presented in this thesis are associated with the following journal articles and conferences:

Articles

- N. Prtljaga, R. J. Coles, **J. O'Hara**, B. Royall, E. Clarke, A. M. Fox and M. S. Skolnick, *"Monolithic integration of a quantum emitter with a compact on-chip beam-splitter"*, Applied Physics Letters 104, 231107 (2014).

- C. Bentham, I. E. Itskevich, R. J. Coles, B. Royall, E. Clarke, **J. O'Hara**, N. Prtljaga, A. M. Fox, M. S. Skolnick and L. R. Wilson, *"On-chip electrically controlled routing of photons from a single quantum dot"*, Applied Physics Letters 106, 221101 (2015).

- N. Prtljaga, C. Bentham[†], **J. O'Hara**[†], B. Royall, E. Clarke, L. R. Wilson, M. S. Skolnick and A. M. Fox, *"On-chip interference of single photons from an embedded quantum dot and an external laser"*, Applied Physics Letters 108, 251101 (2016).

- F. Liu[†], A. Brash[†], **J. O'Hara**[†], L. M. P. P. Martins, C. L. Phillips, R. J. Coles, B. Royall, E. Clarke, C. Bentham, N. Prtljaga, I. E. Itskevich, L. R. Wilson, M. S. Skolnick, A. M. Fox, *"High Purcell factor generation of coherent on-chip single photons"*, arXiv:1706.04422, (2017). (submitted to Nature Nano.)

- R. Kirkwood, **J. O'Hara**, B. Royall, N. Prtljaga, C. M. Natarajan, M. G. Tanner, A. Casaburi, A. M. Fox, M. S. Skolnick, R. H. Hadfield, *"A scalable fabrication process for superconducting nanowire single photon detectors integrated with GaAs waveguide circuits"*, in prep., (2018).

[†]These authors contributed equally.

Conferences

- A. M. Fox, E. Clarke, R. J. Coles, J. E. Dixon, I. J. Luxmoore, M. Hugues, M. N. Makhonin, **J. O'Hara**, N. Prtljaga, A. J. Ramsay, B. Royall, N. A. Wasley, and M. S. Skolnick, *"GaAs Integrated Quantum Photonic Circuits"*, 15–16. IEEE, 2014.

- C. Bentham , I. E. Itskevich, R. J. Coles, B. Royall, E. Clarke, **J. O'Hara**, N. Prtljaga, A. M. Fox, M. S. Skolnick and L. R. Wilson, *"Electrically Controllable On-Chip Single-Photon Router"*, Oral Presentation, UK Semiconductors 2014.

- A. M. Fox, E. Clarke, R. J. Coles, J. E. Dixon, I. J. Luxmoore, M. Hugues, M. N. Makhonin, **J. O'Hara**, N. Prtljaga, A. J. Ramsay, B. Royall, N. A. Wasley, and M. S. Skolnick, *"Integrated Photonic Devices with Single Quantum Dots"*, CLEO 2015, OSA Technical Digest (online) (Optical Society of America, 2015), paper SW1I.1.

- **J. O'Hara**, N. Prtljaga, C. Bentham, B. Royall, E. Clarke, L. R. Wilson, M. S. Skolnick and A. M. Fox, *"On-chip interference of single photons from an embedded quantum dot and a laser"*, Poster Presentation, IoP SSQP, 2016.

- **J. O'Hara**, N. Prtljaga, C. Bentham, B. Royall, E. Clarke, L. R. Wilson, M. S. Skolnick and A. M. Fox, *"On-chip interference of single photons from an embedded quantum dot and a laser"*, Oral Presentation, PECS XII, 2016.

- **J. O'Hara**, N. Prtljaga, C. Bentham, B. Royall, E. Clarke, L. R. Wilson, M. S. Skolnick and A. M. Fox, *"On-chip interference of single photons from an embedded quantum dot and a laser"*, Oral Presentation, ICPS 33, 2016.

TABLE OF CONTENTS

LIST OF TABLES

LIST OF FIGURES

Part I

Introduction and Background

This part of the thesis contains the motivation and theoretical background for the research. Chapter 1 briefly explains the goals and motivations of quantum information processing. Chapter 2 introduces some concepts from quantum optics necessary for understanding the research in later chapters. Finally, in chapter 3, we look at how quantum optical components and circuits may be realized in III-V semiconductor architectures.

CHAPTER 1

QUANTUM INFORMATION

Much of the work in this thesis is motivated by the goal of demonstrating scalable quantum information processing (QIP) operations, and so in this chapter the subject is introduced. This research is also motivated by the desire to increase our undertanding of the physics of quantum dots (QDs) and quantum electrodynamics (QED).

1.1 Quantum information

The development of computers in the last one hundred (or so) years, along with a theory of information processing, has produced machines capable of reliably performing incredibly long and complex calculations. All of this success was based on pre-quantum assumptions and classical systems. Following Bell's theorem [1], the quantum-mechanical phenomena of interference and entanglement were shown to produce larger correlations between measurements than was predicted by classical physical theory [2, 3], and it was subsequently realized [4–6] that some of the limitations of "classical computers" that were thought to be absolutely fundamental are not so. By exploiting these quantum phenomena it should be possible to perform algorithmic procedures using entangled qubits—the quantum analogue of bits—that are not limited to classical information theory [7–9]. Additionally, as fundamental manufacturing and physical limits of conventional computing are approached in the "death march of Moore's law" [10], the

quantum nature of computing systems cannot be ignored and may as well be embraced and exploited [11].

While quantum information theory is still relatively in its infancy, many quantum algorithms are known [12, 13] which can offer a speed-up on classical methods, such as Shor's algorithm for efficient prime factoring [14]. While some of these have been actually performed, this was using only a few qubits to solve relatively simple and specific problems (the number 21 has been prime-factored with tabletop optics and Shor's algorithm [15], for example), and the construction of a *universal quantum computer* of sufficient size to outperform current state-of-the-art universal classical computers and algorithms remains a significant challenge. Another, and perhaps the first, major application of quantum computers is likely to be the simulation of quantum systems [4]—a task which is difficult on conventional computers—and so assist in the understanding of complex quantum phenomena and the development of new molecules and materials. In addition to its known potential "real-world" applications, the topic of QIP is also highly interesting simply for its own sake, given that it explores phenomena at the cutting edge of quantum physics: large-scale entanglement [16], state teleportation [17], macroscopic superpositions and the nature of measurement and decoherence [18], and the transition from quantum to classical regimes as the system size increases. New insights here will not only increase our fundamental physical understanding, but likely also lead to many unforeseeable new ideas and applications, and indeed new challenges.

1.2 Approaches to quantum computation

The realization that quantum effects fundamentally change certain aspects of computation has led to several distinct approaches/architectures that harness the dynamics of quantum systems in different ways. Some, such as the commercially available D-Wave [19], operate on the principle of finding the minima in a quantum system, a process known as quantum annealing [20, 21]. A global minimum is searched for within the solution space by utilizing quantum fluctuations and adiabatic evolution, and for certain problems this can find a better solution within a certain time than is possible with analogous classical annealing methods. Another approach is to build quantum logic circuits analogous to the classical logic circuits of conventional computers, where instead of the binary basis states, called bits, we use 2-level quantum systems, called qubits. The information is processed by evolving the states through many few-qubit gates.

Qubit-based quantum computing is also known as the discrete-variable approach, in contrast to the use of continuous-variable quantum information, where the relevant

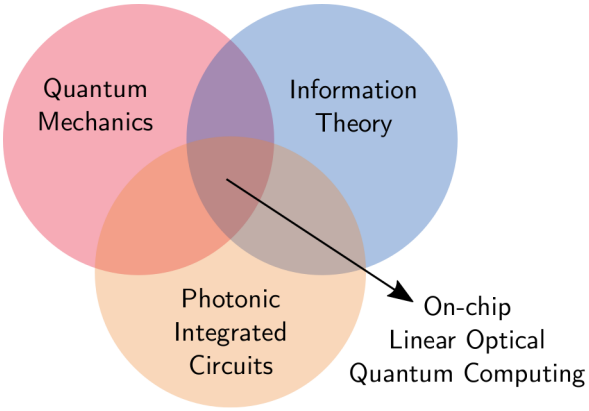

FIGURE 1.1. *On-chip linear optical quantum computing draws from the fields of quantum mechanics, information theory, and photonic integrated circuits.*

observables display a continuum of eigenvalues. The fundamental states are respectively written as:

$$|\psi\rangle_{DV} = c_0 |0\rangle + c_1 |1\rangle \tag{1.1a}$$

$$|\psi\rangle_{CV} = \int_{-\infty}^{\infty} \psi(x) |x\rangle \, dx \tag{1.1b}$$

The electromagnetic field—an example of a quantum harmonic oscillator—can be viewed in both ways. Indeed, the two approaches may be combined in hybrid protocols [22]. We can easily see in this notation the qubit's relation to a bit: whereas a bit is either in the state $|0\rangle$ or $|1\rangle$, a qubit may be in a quantum superposition of these two basis states, with complex amplitudes c_0 and c_1 respectively.

Within the various theoretical paradigms there are many varieties of physical quantum systems under investigation as potential stores and processors of quantum information [23]. There are, for example, trapped ions [24, 25], superconducting junctions [26, 27], spin qubits [28], and the optical networks in semiconductor chips we are interested in here.

1.3 On-chip linear-optical quantum computing

The speed and robustness of photons make them obvious candidates for the transfer of quantum information from one place to another, a task known as quantum communication [29]. Can they also be used for the processing of the information? A potential problem is the fact that light fields interact linearly—i.e. the product of two light fields is

in general the linear superposition of the fields—and information processing is generally based on nonlinear operations in the form of switches. Although nonlinear optical phenomena have been observed, in general it is very difficult to realize high efficiency single photon-photon interactions [30]. For this reason a scheme for efficient computation with linear optics was proposed by Knill, Laflamme & Milburn (KLM) [31]. The realization of the ability to form a complete set of universal quantum gates, for example the CNOT gate [32, 33], using only linear optical interactions, revolutionized optical quantum computing and opened the field of universal linear-optical quantum computing (LOQC) [34–36]. The KLM scheme is an example of measurement-based QIP [37], where the lack of nonlinearity is circumvented by adaptive measurements (with an effective nonlinearity in detection).

Scaling up tabletop quantum logic circuits in their current forms would require much greater resources and would result in impractically large computers. However, if all the quantum computing elements can be placed on a semiconductor chip, as with current conventional computer technology, then it should be much more readily scalable. This is the goal of solid-state LOQC research, where the qubits are realized as the quantum states of single-photons, and the quantum gates are on-chip nanoscale semiconductor structures. In this computing architecture, the photons travel around waveguides and the logic gates are physical components of the photonic integrated circuit (PIC). This is in the contrast to, e.g. trapped-ion architecture, where the qubits are physically localized, and entanglement and other operations are performed by directly operating on the stationary qubits.

In terms of scalability, the size of the individual components is crucial. This is because consistent fabrication of wafers and structures is limited, for technological reasons, to a fixed size. In addition, even if larger structures could be made, cooling the system down to low temperatures becomes more difficult. And as one approaches 0 K, each additional degree of cooling is increasingly hard to obtain.

Many of the components being developed for LOQC should also be useful in related optical circuits, where one stores and manipulates qubits in the form of, say, spins in QDs ("static qubits"), but the quantum information moves around the circuit as the state of photons ("flying qubits") [38]. The closely related field of photon-based quantum simulators [39] also matures alongside this work. There the essential difference is a more focused approach to simulation of quantum systems, rather than universal processing of quantum information. Boson sampling, for example, is closely linked to LOQC [40, 41]. It uses the same components, but tackles a specific problem which is classically difficult. Even the state evolution of small linear optic circuits—not of the order of

complexity required for universal quantum computation—quickly becomes intractable for a powerful classical computer. It has attracted attention mainly as a demonstration of "quantum speed-up" that may be achievable in the relatively short-term (or not so short-term [42]).

1.4 LOQC components

In the original KLM proposal, the linear optical components sufficient for QIP were single-photon sources (SPSs), beam splitters (BSs), phase shifters, and detectors. We shall look at each of these in turn below.

1.4.1 Single-photon sources

A LOQC PIC generally creates a many-photon state by interfering many single-photon states. So the first requirement of the circuit is at least one SPS. These come in two fundamental varieties: deterministic, and probabilistic. In a probabilistic single-photon source, a weak single-photon state is produced, so that mostly there are no photons, and with small probability single photons. This can be managed by heralding – in both spontaneous parametric down-conversion and four-wave mixing, two photons are produced, and one is used to herald the arrival of the other, so that it is known when a single-photon state has been produced in one channel. Deterministic sources, by contrast, produce a single-photon each time they are triggered. This type of light source is usually a quasi-atomic system, for example QDs and colour centres, or indeed atoms. The quality of a SPS can be defined by

$$Q_{SPS} = \eta \cdot \nu \cdot \left[1 - g^{(2)}_{\mathrm{HBT}}(0)\right], \tag{1.2}$$

where η is the probability of emission into the desired spatial mode per trigger, ν the indistinguishability of the photons, and $\left[1 - g^{(2)}_{\mathrm{HBT}}(0)\right]$ the purity of the single-photon states (see section 2.1.5). Only when all three are unity will we get single indistinguishable photons each time we trigger the source. A detailed review of single-photon sources (and detectors) is given in [43].

1.4.2 Qubits and guiding light

In LOQC, a qubit is usually represented by some bipartite degree of freedom of a photon [44]. In the *dual-rail* representation*, the qubit state is determined by the occupation of a

*Some authors use this terminology to refer to representations that use any bipartite degree of freedom of a photon, so that a polarization qubit, for example, would also be called a dual-rail qubit.

photon in one of two spatial modes, a and b, so that the logical states are (cf. equation 1.1a)

$$|0\rangle = |1\rangle_a \otimes |0\rangle_b \equiv |1\rangle_a |0\rangle_b \tag{1.3a}$$
$$|1\rangle = |0\rangle_a \otimes |1\rangle_b \equiv |0\rangle_a |1\rangle_b \tag{1.3b}$$

Alternatively, and equivalently, a qubit may be represented by the polarization degree of freedom of a photon, so that

$$|0\rangle = |H\rangle \tag{1.4a}$$
$$|1\rangle = |V\rangle \tag{1.4b}$$

These representations may be switched between using only a polarizing BS.

In all cases the quantum information is processed by guiding light through a series of optical elements to an array of detectors. For tabletop experiments, the light travels in free space via a network of mirrors. However, this guiding is achieved in a PIC by way of nanoscale waveguides. There are several ways of producing waveguides, and a couple of these are discussed in more detail in chapter 3.

1.4.3 Beam splitters

The optical modes of the circuit are combined using BSs, which usually are of the 4-port variety, so that they have two input and two output modes. The required splitting ratio varies, so that a circuit may require both $50:50$ and $67:33$ splitters, for example [45]. In tabletop experiments, macroscopic semi-reflective surfaces are used, whereas on-chip the nanoscale waveguides are brought together and coupled, either evanescently as in a directional coupler, or by self-imaging as in a multi-mode interferometer. In terms of quantum information all such processes are equivalent and so, for example, any physical realization of a $50:50$ BS can be used to implement the Hadamard operation.

1.4.4 Phase shifters

A phase shift is another basic sub-operation in photonic computing. This element of the circuit varies the phase of one mode relative to another. On-chip this is usually achieved by varying the refractive index of one path—such as by thermal or electro-optical tuning [46, 47]—in order to control the total optical path length (OPL). Another possibility is to use a microelectromechanical systems (MEMS) device that mechanically moves a section of the path such that the total OPL increases or decreases.

Property	Description
Quantum efficiency	The probability of registering a count if a photon arrives at the detector
Jitter	The variation in the time interval between the absorption of a photon and the generation of an output electrical pulse from the detector
Dead time	The time interval that follows the absorption of a photon, during which the detector is unable to reliably register a second photon
Dark counts	The probability of producing an output pulse in the absence of a photon
Spectral range	The wavelength range over which the detector can reliably detect photons
Photon-number resolution	The ability to resolve the number of photons that are absorbed in a given detection event

TABLE 1.1. *Properties of a single-photon detector.*

1.4.5 Single-photon detectors

We begin the circuit with SPSs, and at the end we need single-photon detectors. Ideally these would be of unit efficiency, and produce an electrical pulse with no time delay variation. The requirements on detectors for scalability are very demanding, and the development of a robust, scalable detection system is crucial. Table 1.1 summarizes the properties relevant to single-photon detectors [48].

1.5 LOQC feasibility

The operations in a LOQC circuit are linear, and because of this the gates can only be implemented non-deterministically. With some probability a gate will succeed in its intended operation, and this success is determined by whether or not ancillary photons are detected. Thus, although we have said that a qubit is represented by the state of a single photon, hundreds of photons may be needed in practice to end up with the equivalent of a single functional qubit. However, this overhead is highly dependent on the exact scheme of computation, and increasingly efficient proposals are still being described. For example, in [49], less than 20 physical photons are needed per final qubit.

But why bother when a deterministic matter qubit gate does not have this probabilistic overhead? The answer is that in LOQC, the stochastic noise levels should be able to be

lowered several orders of magnitude below what is achievable with matter-based qubits [50]. Furthermore, the primary components of PICs are being investigated and improved continuously for classical computing and other photonic uses anyway. It is therefore not unreasonable to expect that the technology will continue to improve rapidly, both in the number and quality of devices on a single chip.

The field of LOQC has been active for over 15 years, and optimism remains over the possibility to implement advanced linear optical QIP protocols in PICs. The use of photons for quantum technologies [51] remains a promising field of research.

1.6 LOQC in this thesis

In this thesis we make progress towards LOQC circuits in the III-V semiconductor architecture. In chapter 5 we integrate SPSs with waveguides and BSs, demonstrated for the first time through on-chip Hong-Ou-Mandel (HOM) interference, a key effect in LOQC. In chapter 6 we improve the quality of the solid-state SPS through its inclusion in an on-chip waveguide-coupled nanoscale cavity, and so produce highly indistinguishable single photons as is required for QIP with photonic states. The single photons also need to be "on-demand", a requirement that chapter 7 investigates in more detail. Finally, in chapter 8, we look at progress towards integrating the remaining components, demonstrating on-chip detectors and the use of diode wafers to improve reliability and scalability.

CHAPTER 2

QUANTUM OPTICS

The field of quantum optics has been developing from the birth of quantum theory until the present day. While the discretization of radiation energies and the introduction of the photon is what started the quantum revolution, in much of early quantum theory the rigorous application of quantized fields was not required. Later, after quantum electrodynamics successfully merged electromagnetism and special relativity, the implications for non-relativistic systems were investigated. The boundaries and properties of non-classical and classical fields began to be explored, at first theoretically, and afterwards experimentally. Similarly, the implications of a fully quantized field on light-matter interactions were seen on paper and then in the lab. Today the field of quantum optics and its application to quantum information continues to develop [52], with quantum states of light being explored and measured in novel ways, and the interaction of light with matter are being pushed to greater extremes. In the first part of this chapter we review some of the work on quantum fields that is relevant to the research of Part II. We then look at light-matter interactions in the quantum picture, first examining a bare two-level system, then adding a resonant monochromatic field, and finally adding a cavity.

2.1 Quantum optical fields

In optical quantum information processing (QIP), we generally use the single-photon state as the building block to produce two-photon states, three-photon states, and so on. So to begin we want to be able to excite the field into the pure number state $|1\rangle$, and for this state not to dephase over the course of the information transfer or processing. The state of the field can can be analyzed by performing correlation measurements.

2.1.1 Fock states

The quantum optical field is an example of a quantum harmonic oscillator. A single optical mode of angular frequency ω_a has the Hamiltonian

$$H = \hbar\omega_a \left(N + \tfrac{1}{2}\right), \tag{2.1}$$

and the energy eigenvalues

$$E_n = \left(n + \tfrac{1}{2}\right)\hbar\omega_a, \quad n = 0,1,2,3..., \qquad \text{[J]} \tag{2.2}$$

where N is the number operator and yields the number of photons n that the field contains. When the field contains 0 photons we see that it still has an energy $\frac{1}{2}\hbar\omega_a$, the *zero-point* or *vacuum field* energy, and that this is the lowest energy state of a ladder with equidistant energy spacing $\hbar\omega_a$. The creation and annihilation* operators, $a^\dagger$ and a, (collectively the ladder operators) move the system up and down the ladder respectively. The number operator can also be constructed through $N = a^\dagger a$. The Fock states, or number states, are then $|n\rangle$, and form an orthonormal basis for the field. Any state of the mode can be expressed as a superposition of the number states, and the general (normalized) state is

$$|\psi\rangle = \sum_{n=0}^{\infty} c_n |n\rangle, \text{ where } \sum_{n=0}^{\infty} |c_n|^2 = 1. \tag{2.3}$$

For the single-photon state only the complex amplitude $|c_1|$ is non-zero, and therefore its magnitude is unity. States with large $|c_0|$, small $|c_1|$, and vanishing amplitude for the other terms are sometimes called "weak single-photon states". However they more closely approximate a zero-photon state, since the highest probability is to be in the vacuum state.

*Or "destruction".

2.1.2 Coherent states

The coherent states $|\alpha\rangle$ are the eigenstates of the annihilation operator – destruction of a photon leaves the state unchanged and yields the eigenvalue α:

$$a|\alpha\rangle = \alpha|\alpha\rangle . \tag{2.4}$$

The coherent states' expansion in Fock space are given by [53, p. 78]

$$|\alpha\rangle = e^{-\frac{1}{2}|\alpha|^2} \sum_{n=0}^{\infty} \frac{\alpha^n}{\sqrt{n!}} |n\rangle . \tag{2.5}$$

The occupation probabilities in the number state basis form a Poissonian distribution of mean value α. When $\alpha \ll 1$, we have an example of the so-called "weak single-photon state" mentioned above.

2.1.3 First-order correlation measurements

We can probe the quantum states of optical fields through the correlations that we measure. Correlation measurements of the electric fields produce what are known as *first-order correlation functions**, and are denoted $G^{(1)}$, or $g^{(1)}$ if normalized. As a function of time t and delay τ between the first detection (on one detector) and the second detection (on the other), it is given by [54, p. 17]:

$$g^{(1)}(t, t+\tau) = \frac{\langle \mathcal{E}^*(t)\mathcal{E}(t+\tau)\rangle}{\langle \mathcal{E}^*(t)\mathcal{E}(t)\rangle}. \tag{2.6}$$

where $\mathcal{E}$ is the electric field amplitude. This is the quantity that is probed with a Mach-Zehnder interferometer (figure 2.1(a)), where the field is split with one beam splitter (BS) and recombined with another†. By varying the arm length of one path, we vary the electric field in time. When recombined, the two fields interfere, and if we measure the resulting field with a single photodetector, we will see the intensity periodically vary as a function of delay. The decay of the interference contrast as the delay is varied directly corresponds to the decay of the field coherence in time. For any real source, $g^{(1)}(t, t+\infty) = 0$.

2.1.4 Beam splitters and photodetectors

A beam splitter (BS) is an optical element that combines four electromagnetic field modes. If a photon is incident from any one of these modes its amplitude is split amongst two

*Sometimes called first-order coherence.

†Or equivalently with the same beam splitter in a Michelson interferometer.

Experiment	Source fields	Beam splitter operations	# Photodetectors	Correlation
MZ	1	2	1	$g^{(1)}(\tau)$
HBT	1	1	2	$g^{(2)}(\tau)$
HOM	2	1	2	$g^{(2)}(\tau)$

TABLE 2.1. *Comparison of different correlation measurement schemes. MZ = Mach-Zehnder; HBT = Hanbury Brown & Twiss; HOM = Hong-Ou-Mandel.*

corresponding output modes. A photodetector is an element in the field mode that can absorb a photon's worth of energy from the field. Photodetectors do not necessarily distinguish between the absorption of one photon and the absorption of two (or more) photons, often due to technical limitations.

In regards to Hanbury Brown & Twiss (HBT) correlation measurements described below (section 2.1.5.1), the BS is useful because in general we do not have number-resolving detectors that can tell us directly the time-dependence of the number state of the field. Using a BS, we can divide the field in two and correlate the output of two detectors. However, in the case of the Hong-Ou-Mandel (HOM) effect (section 2.1.6), the BS is essential because its operation produces the two-mode superposition state.

2.1.5 Second-order correlation measurements

The correlation of photon number is a *second-order correlation measurement*—a correlation of the the electric field to the second power—and is denoted $G^{(2)}$. As a function of time t and delay τ between the first detection (on one detector) and the second detection (on the other), it is given by

$$\begin{aligned} G^{(2)}(t,t+\tau) &= \langle a^\dagger(t)a^\dagger(t+\tau)a(t+\tau)a(t)\rangle \\ &= \langle n(t)n(t+\tau)\rangle \end{aligned} \tag{2.7}$$

When normalized

$$g^{(2)}(t,t+\tau) = \frac{\langle n(t)n(t+\tau)\rangle}{\langle n(t)\rangle \langle n(t+\tau)\rangle} \tag{2.8}$$

A lack of second-order correlation yields $g^{(2)}(t,t+\tau) = 1$. For any real source, $g^{(2)}(t,t+\infty) = 1$.

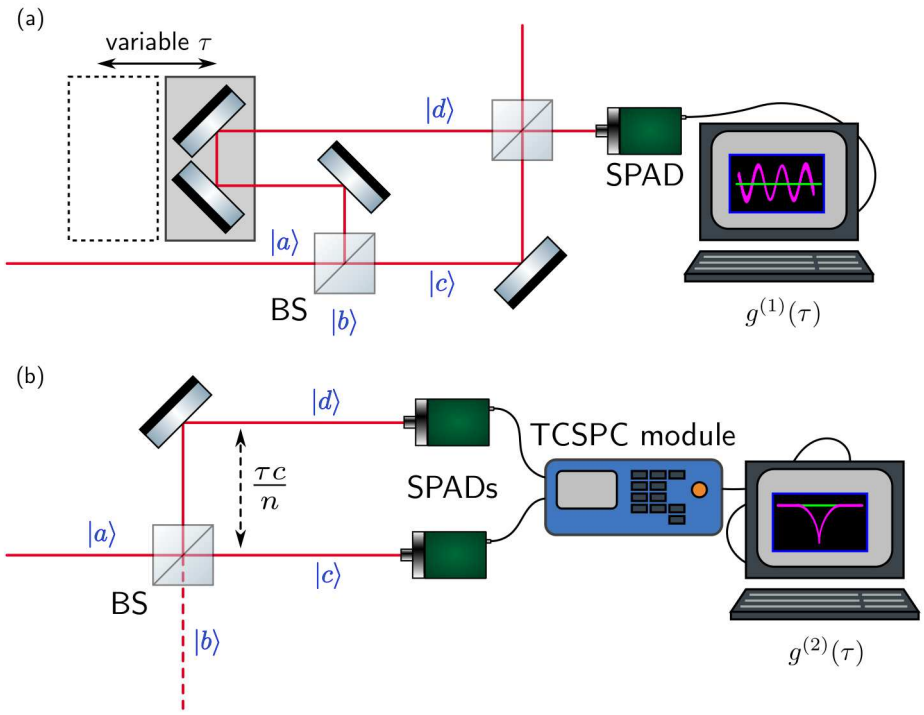

FIGURE 2.1. *Typical experimental arrangements for performing correlation measurements. (a) With this Mach-Zehnder geometry, $g^{(1)}(\tau)$ may be determined by looking at how the visibility of the interference fringes changes as the length of one of the paths between the beam splitters is varied. (b) In a $g^{(2)}(\tau)$ measurement, the physical path difference is often fixed, and a time correlation circuit electronically determines the difference in the arrival time of two photons. In a HBT measurement, only one of the input paths is used, whereas in a HOM measurement, both are used. BS = beam splitter; SPAD = single-photon avalanche diode; TCSPC = time-correlated single-photon counting.*

2.1.5.1 Hanbury Brown & Twiss: Antibunching

When we divide a single field mode using a BS, and observe the intensity correlations of the two output modes, we are performing a Hanbury Brown & Twiss (HBT) experiment [55] (figure 2.1(b)). The correlations tell us something about the statistical distribution of photons in the original field. If the field consists only of excitations to the single-photon state, we should only detect one photon at a time, so that detection of a photon in one of the output modes should be anticorrelated with the detection of a photon in the other. This phenomenon is known as antibunching. In contrast to thermal sources, which tend to produce many photons at the same time—so that a single detection is correlated with further detections—single-photon and few-photon sources have gaps in the photon distribution. A field in an n-photon Fock state has [54, p. 163]

$$g^{(2)}_{\mathrm{HBT}}(\tau = 0) = \frac{n(n-1)}{n^2}. \tag{2.9}$$

This is 0 for a single-photon state, 0.5 for a two-photon state, and asymptotically approaches 1 as $n \to \infty$. A coherent state has $g^{(2)}_{\mathrm{HBT}}(\tau) = 1$ for all τ, since, as previously mentioned, the photon number distribution is Poissonian. This means the separation between photons is random, and detection of one photon gives no information about detection of a second photon. For this reason, a system showing $g^{(2)}_{\mathrm{HBT}}(\tau)$ values below unity is said to produce a "non-classical" sub-Poissonian field. Antibunching and sub-Poissonian statistics are closely related, but are not equivalent [56]. Antibunching requires $g^{(2)}_{\mathrm{HBT}}(\tau = 0) < 1$, whereas sub-Poissonian implies that $g^{(2)}_{\mathrm{HBT}}(\tau) < 1$ for some τ. Super-Poissonian fields are those that show bunching of photons, of which the output of a thermal source is an example. $g^{(2)}_{\mathrm{HBT}}(\tau)$ are measured for quantum dots (QDs) and lasers in chapter 5.

2.1.5.2 Experimental considerations

One obvious concern is that in an experimental situation we will have background light and imperfect detectors. In the latter case a non-ideal quantum efficiency does not affect the statistical properties of the data, but rather only increases the time required to collect them. The detector time response, however, does add an uncertainty in the arrival time of the photons, and this time broadening is convolved with any feature in the incident field. Another aspect of real detectors is the production of dark counts—counts even when no photon is absorbed. As this characteristic is (approximately) spectrally uniform and temporally random, it behaves as a kind of environmental background light (B),

and so the two can be treated together, and corrected using the formula [57]

$$g^{(2)}(\tau) = \left[c(\tau) - (1-\rho^2)\right]/\rho^2 \tag{2.10}$$

where $c(t)$ is the coincidence count rate normalized to the equivalent Poissonian source, and the signal (S) to total counts ($S+B$) is given by $\rho = S/(S+B)$.

2.1.6 Hong-Ou-Mandel: Interference

There are a number of ways to produce entangled photonic states, but the method which is most relevant to scalable linear-optical quantum computing (LOQC) is the Hong-Ou-Mandel (HOM) effect [58]. Consider a BS with two input modes, a and b, and two output modes, c and d. What happens when single-photon states are incident from a and b simultaneously? In the case that they are *distinguishable*, they always behave as independent photons, and we are essentially doing two overlapping HBT experiments, and this will result in a cross-correlation of the input fields. However, when two *indistinguishable* photons enter, something more interesting occurs. Because bosonic states have overall symmetric wavefunctions, and because there is a phase shift associated with reflection, the two states corresponding to the cases when the two photons leave via different outputs interfere destructively. The only possibility is that they exit together through the same output port, forming the superposition:

$$|1\rangle_a |1\rangle_b \xrightarrow{\text{BS}} c_1 |2\rangle_c |0\rangle_d + c_2 |0\rangle_c |2\rangle_d \tag{2.11}$$

The output is no longer a combination of single-photon states, but a bi-photon path-entangled state. For a 50/50 BS, the superposition is equal, i.e. $c_1 = c_2 = \frac{1}{\sqrt{2}}$. In this case one observes with equal probability either two photons in mode c or two photons in mode d.

Time-resolved two-photon interference (TPI) was theoretically studied in [59], with the prediction of quantum beating when the two initial photons have different frequencies. This was subsequently observed [60]. For realistic sources we often have to include the effect of dephasing in the theoretical analysis [61], although it is the goal of the fabricator and experimenter to minimize dephasing as much as possible, owing to its detrimental effect.

Scaling the TPI effect up to many-photon interference is the basis of LOQC and boson sampling [41]. It is therefore very important to our work and appears throughout this thesis. In chapter 5 we show HOM interference between QDs and a laser using an on-chip beam splitter. Chapter 7 shows and discusses a pulsed HOM measurement.

Finally, a device shown in chapter 8 has been designed with the intention of enabling fully on-chip $g^{(2)}(\tau)$ measurements, in particular those showing quantum interference.

2.1.7 Visibility of interference

The $g^{(1)}$ and the HOM measurements are examples of interferometry of the first and second power of the electric field respectively. The degree of interference in both cases is quantified in terms of a visibility $V(\tau)$:

$$V(\tau) = \frac{I(\tau)_{\max} - I(\tau)_{\min}}{I(\tau)_{\max} + I(\tau)_{\min}} \tag{2.12a}$$

$$V(\tau) = \frac{|g^{(2)}_{\mathrm{HOM}}(\tau)_{\perp} - g^{(2)}_{\mathrm{HOM}}(\tau)_{\parallel}|}{g^{(2)}_{\mathrm{HOM}}(\tau)_{\perp}} \tag{2.12b}$$

The former is how the visibility is usually defined in a $g^{(1)}$ experiment, where $I(\tau)$ refers to the intensity of interference fringes, and the latter is the usual definition used for quantifying the success of a HOM. $g^{(2)}_{\mathrm{HOM}}(\tau)_{\perp}$ is the second-order correlation observed when modes a and b are purposefully made distinguishable, often by making the polarizations perpendicular (as in chapter 7). $g^{(2)}_{\mathrm{HOM}}(\tau)_{\parallel}$ is what is observed when conditions are optimized for interference (often by matching polarizations), and so in the ideal case the photons are completely indistinguishable. In the numerator we have taken the absolute value of the difference of the two measurements, since as we will see in chapter 5, indistinguishability may result in the observation of bunching or antibunching. Typically the maximum visibility is observed at zero delay, i.e. $V_{\max} = V(\tau = 0)$. A comparison of relevant $g^{(1)}$ and $g^{(2)}$ measurements is given in table 2.1.

2.2 Cavity quantum electrodynamics

In this section we ultimately want to understand the dynamics of a resonantly excited quantum emitter in a cavity, a system which we study experimentally in chapters 6 and 7. We start with a simple two-level system (2LS) spontaneously decaying into free space, then add a (near-)resonant field, and finally look at the effect of a single-mode cavity. Mostly this development follows the formalism in [53, 62], with additional clarification from [54, 63–65].

2.2.1 A 2-level system

Here we look at the description of an isolated 2LS, and the parameters which describe its evolution. The system is a single charged particle that has two energy eigenstates. We

will call the lower energy level its ground state, $|g\rangle$, and its higher energy level its excited state, $|e\rangle$. When in its excited state, it has energy E_2, and may decay to its ground state, of energy E_1, by emission of a photon or through some non-radiative process. The energy lost in this process is absorbed by a much larger reservoir (of harmonic oscillators), so that the 2LS is effectively isolated.

2.2.1.1 An unperturbed two-level system

To simplify our quantum description of the 2LS, the zero for energy is set midway between the energies E_1 and E_2. Then the Hamiltonian reads

$$H_A = \tfrac{1}{2}\hbar\omega_a\sigma_z, \tag{2.13}$$

where $\hbar\omega_a$ is the energy difference of the levels, and σ_z is one of the pseudo-spin operators:

$$\sigma_z \equiv |e\rangle\langle e| - |g\rangle\langle g| \tag{2.14a}$$
$$\sigma_+ \equiv |e\rangle\langle g| \tag{2.14b}$$
$$\sigma_- \equiv |g\rangle\langle e| \tag{2.14c}$$

For a 2LS in a state described by the density operator ρ, the expectation value $\langle\sigma_z\rangle$ gives the population difference. The operators σ_+ and σ_- are the raising and lowering operators for the system, although so far we have not introduced a mechanism by which the system may move between energy levels.

The transition dipole moment is given by

$$\vec{\mu}_{12} \equiv q\langle g|\hat{r}|e\rangle\,, \qquad [\mathrm{C\,m}] \tag{2.15}$$

where q is the charge and $\hat{r}$ the co-ordinate operator of the quantum particle. This vector gives the strength of the 2LS's interaction with an electric field $\vec{\mathcal{E}}$ in the *dipole approximation**[63, p. 149], where we assume that the emitter's spatial extent is much less than that of significant variations in the field.

2.2.1.2 Energy decay

Experimentally we know that an atom in an excited state will evolve towards its ground state. In radiative decay, the system moves to a lower energy configuration through the emission of a photon. This decay process is spontaneous, that is to say random. However,

*Or *long-wavelength approximation*.

repeated measurements produce an exponential decaying probability distribution with time constant τ_r — the average time between excitation and emission. The inverse of this, the spontaneous emission rate*, as given by the Weisskopf-Wigner approximation, is

$$\Gamma_r = \frac{1}{\tau_r} = \frac{n}{4\pi\epsilon_0}\frac{4\omega_a^3|\vec{\mu}_{12}|^2}{3\hbar c^3} \qquad [s^{-1}] \quad (2.16)$$

where n is the index of refraction, ϵ_0 is the vacuum permittivity, and c the speed of light in vacuum. We can see that if we measure the emission rate and energy, we can find the magnitude of the dipole moment. In chapter 7 we do just this, as well as investigating the effects of additional levels on the emission rate.

In addition to emitting a photon, the excited state can return to its ground state by, for example, phonon emission. Such processes are called non-radiative relaxation, and occur at a rate Γ_{nr}. The total lifetime of the state T_1 is then given by

$$\frac{1}{T_1} = \Gamma_1 = (\Gamma_r + \Gamma_{nr}). \qquad [s^{-1}] \quad (2.17)$$

Depending on whether or not the excited and ground states adhere to radiative selection rules [54, p. 55], and also to what extent non-radiative channels are available, either the radiative or non-radiative decay channels can dominate.

Now let's consider the second-order correlation functions of the field produced by such an emitter. If the 2LS is continuously pumped, then after an emission event the system may immediately be re-excited. Thus the detection of a photon only guarantees that a second won't be detected instantaneously, with the probability of a second detection recovering exponentially with the time constant of the excited state. In the simplest case, the $g^{(2)}(\tau)$ is given by

$$g^{(2)}(\tau) = 1 - e^{-\frac{|\tau|}{T_1}}. \quad (2.18)$$

In chapter 5 we show and discuss situations in which this simple formula does not completely capture the dynamics of the field.

An emitter that decays exponentially through the processes described above displays a Lorentzian spectrum, with a full width at half maximum (FWHM) γ_1 in angular frequency ($\mathrm{rad\,s^{-1}}$) equal to Γ_1. This superficially simple but non-trivial equivalence of the inverse lifetime Γ_1 and emission linewidth γ_1 has been verified experimentally with atoms to a very high degree of accuracy [66]. However, there are additional processes that can affect the linewidth without affecting the lifetime, which we will now look at.

*Which is also the *Einstein A coefficient*.

2.2.1.3 Phase decay

The emitter may be involved in elastic interaction events that do not cause depopulation but yet affect the relative phase of the excited and ground states – in other words, they damp the emitter polarization. Such processes are known as pure dephasing. The pure dephasing rate γ_2^*, and its inverse, the pure dephasing time T_2^*, capture the total effect of these processes towards decoherence. However, depopulation also contributes to dephasing. The *total* dephasing rate γ_2 and *total* coherence time T_2 are then given by

$$\gamma_2 = \left(\frac{\gamma_1}{2} + \gamma_2^*\right) \qquad [\mathrm{rad\,s^{-1}}] \quad (2.19)$$

and

$$\frac{1}{T_2} = \left(\frac{1}{2T_1} + \frac{1}{T_2^*}\right). \qquad [\mathrm{s^{-1}}] \quad (2.20)$$

If there are no dephasing processes, or if $T_1 \ll T_2^*$, we see that $T_2 = 2T_1$. In this case the emitter displays lifetime-limited coherence*, i.e. decoherence occurs only through depopulation, either by spontaneous emission or non-radiative relaxation. For solid-state emitters, which are housed in a crystal environment, pure-dephasing processes are a significant concern. Phonons can, for example, significantly disrupt the system at temperatures not far above 0 K. In the presence of dephasing the linewidth is no longer the inverse lifetime, but γ_2. This is detrimental to photon indistinguishability. In chapters 6 and 7 we see how, through the use of a cavity and Purcell enhancement (section 2.2.3.1), we can overcome non-radiative dephasing.

Table 2.2 summarizes these processes, and figure 2.2 shows how they manifest themselves in the decay and spectrum of the emission.

2.2.1.4 Master equation for a decaying 2LS

The state of any quantum system can be described by a density matrix, in analogy to the statistical mechanics approach. The following Lindblad-form master equation describes the time evolution of the system's density matrix ρ under the decay processes outlined above [53, p. 43]:

$$\begin{aligned}\dot{\rho} = &-\frac{i}{2}\omega_a\left[\sigma_z, \rho\right] \\ &+ \frac{\gamma_1}{2}\left(2\sigma_-\rho\sigma_+ - \sigma_+\sigma_-\rho - \rho\sigma_+\sigma_-\right) + \frac{\gamma_2^*}{2}\left(\sigma_z\rho\sigma_z - \rho\right).\end{aligned} \quad (2.21)$$

*Or equivalently, *transform-* or *Fourier-limited coherence*, in reference to the Fourier transform. The same idea may also be referred to, less generally, as *radiatively-limited coherence*, when appropriate.

Process	Timescale (s)	Linewidth (rad/s)	Description
Spontaneous emission	$1/\Gamma_r$	γ_r	Spontaneous radiative emission
Non-radiative relaxation	$1/\Gamma_{nr}$	γ_{nr}	System returns to ground state without emission of a photon
Population decay	T_1	γ_1	Excited system returns to ground state by any means
Pure dephasing	T_2^*	γ_2^*	Decay of excited-ground coherence without depopulation
Dephasing	T_2	γ_2	Total decay of excited-ground coherence (polarization)
Photoluminescence	T_1	$2\gamma_2$	Combined effect of all processes

TABLE 2.2. *Processes and timescales relevant to understanding the coherence of an emitter.*

This equation is for 0 K (no thermal photons at optical frequencies affecting the level populations—the reservoir state is that of the vacuum electromagnetic field), and we have ignored the (small) frequency shifts of ω_a upon inclusion of damping. We assume γ_1 can be modelled as a single exponential decay, so that one process dominates. The same is true of the γ_2^* term. The reservoirs which absorb the decays are assumed to be *Markovian*. This means that correlations in the reservoir decay much faster than that of the system, so that the system does not influence its future state through lasting modifications of the reservoir states.

2.2.2 2-level system with a (near-)resonant field

Now we irradiate our system with a monochromatic field. The field may be treated semi-classically or quantum mechanically, depending on the problem. Classically, a monochromatic electric field can be described by

$$\vec{\mathcal{E}}(t) \equiv 2\mathcal{E}\cos(\omega_l t + \phi)\hat{e}, \qquad [\mathrm{NC}^{-1}] \quad (2.22)$$

where $\mathcal{E}$ is a real amplitude, ω_l and ϕ the angular frequency and phase, and $\hat{e}$ a unit polarization vector.

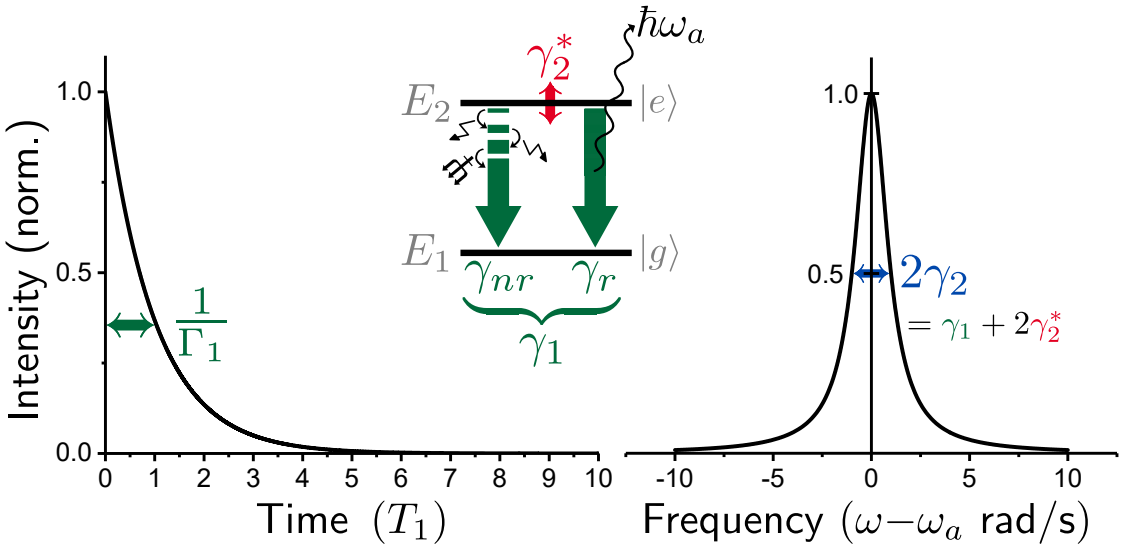

FIGURE 2.2. *2-level system energy level schematic (inset, middle), and the temporal (left) and spectral (right) profiles of the emission.*

2.2.2.1 Rabi frequency

With the addition of a resonant field, $\omega_l = \omega_a$, the system Hamiltonian becomes

$$H_S = \tfrac{1}{2}\hbar\omega_a\sigma_z - \mu\mathcal{E}\left(e^{-i\omega_a t}\sigma_+ + e^{i\omega_a t}\sigma_-\right), \tag{2.23}$$

where $\mu \equiv \hat{e}\cdot\vec{\mu}_{12}e^{i\phi}$. We have used the dipole approximation as before, and now what is known as the rotating-wave approximation (RWA) has been applied. In the RWA, we discard fast dynamics that occur at $(\omega_l + \omega_a)$ frequencies (or timescales of $\sim$ fs at optical frequencies), dynamics that are anyway not resolved experimentally [63, p. 151]. We can define an angular frequency from the energy of the interaction term:

$$\Omega \equiv 2\frac{\mu\mathcal{E}}{\hbar}. \qquad [\mathrm{rad\,s^{-1}}] \tag{2.24}$$

This is the Rabi frequency. The laser causes the 2LS to cycle between the ground and excited states at this angular frequency, so that, for an initial ground state, the occupation of the states may be determined by

$$\langle\sigma_z(t)\rangle = \langle e|\rho(t)|e\rangle - \langle g|\rho(t)|g\rangle = -\cos(\Omega t). \tag{2.25}$$

Off resonance the Rabi oscillations occur at the higher *generalized Rabi frequency*

$$\tilde{\Omega} = \sqrt{\Omega^2 + (\omega_l - \omega_a)^2}, \qquad [\mathrm{rad\,s^{-1}}] \tag{2.26}$$

with a reduced amplitude $\Omega^2/\tilde{\Omega}^2$.

2.2.2.2 Pulses

Rabi oscillations are shown and modelled in chapter 7. The oscillations in that case are only transiently induced, and so the experimental signature is the variation of the photoluminescence (PL) intensity resulting from different degrees of population transfer. If the pulse is a Gaussian, it has an electric-field amplitude temporal profile $\mathcal{E}(t)$ given by

$$\mathcal{E}(t) = \frac{\hbar}{2\mu}\Omega(t) = \frac{\hbar}{2\mu}\frac{\Theta}{\sqrt{\pi w^2}} e^{-\left(\frac{t-t_{\mathrm{P}}}{w}\right)^2}, \qquad [\mathrm{NC}^{-1}] \quad (2.27)$$

where t_{P} is the time corresponding to the arrival of the pulse maximum; w is a measure of the width of the pulse, related to the FWHM T_{P} through

$$w = \frac{T_{\mathrm{P}}}{\sqrt{4\ln(2)}}; \qquad [\mathrm{s}] \quad (2.28)$$

and Θ is the *pulse area*. The pulse area is obtained by integrating the Rabi frequencies over time (equation (7.1)). A pulse area of $\pi/2$ swaps the populations of the levels of the 2LS*. If the electric field amplitude has a Gaussian profile, the envelope of the corresponding intensity profile is also a Gaussian, but with a FWHM which is $\sqrt{2}$ smaller. Pulse areas and the effect of pulse duration are further discussed in chapter 7.

2.2.2.3 Master equation for resonance fluorescence

Now we wish to recover the energy and phase damping. For transitions at optical frequencies, where $\Omega \ll \omega_a$, the damping terms for resonance fluorescence (RF) are approximately the same as for spontaneous emission (SE). Then the master equation becomes [53, p. 50]

$$\begin{aligned}\dot{\rho} = &-\frac{i}{2}\omega_a\left[\sigma_z,\rho\right] \\ &+\frac{i}{2}\Omega\left[e^{-i\omega_a t}\sigma_+ + e^{i\omega_a t}\sigma_-,\rho\right] \\ &+\frac{\gamma_1}{2}(2\sigma_-\rho\sigma_+ - \sigma_+\sigma_-\rho - \rho\sigma_+\sigma_-) + \frac{\gamma_2^*}{2}(\sigma_z\rho\sigma_z - \rho).\end{aligned} \quad (2.29)$$

The second line describes the classical incident field.

*This is because of the factor of 2 in equation (2.24). If the factor of 2 is not used, as is often the case, the pulse area to swap the populations would be π. We use the latter convention in chapter 7.

2.2.2.4 Optical Bloch equations

The expectation values for the operators of equation (2.14) evolve according to

$$\langle \dot{\sigma}_z \rangle = i\Omega e^{-i\omega_a t} \langle \sigma_+ \rangle - i\Omega e^{i\omega_a t} \langle \sigma_- \rangle - \gamma_1 \big(\langle \sigma_z \rangle + 1 \big) \tag{2.30a}$$

$$\langle \dot{\sigma}_+ \rangle = i\omega_a \langle \sigma_+ \rangle + \tfrac{i}{2}\Omega e^{i\omega_a t} \langle \sigma_z \rangle - \gamma_2 \langle \sigma_+ \rangle \tag{2.30b}$$

$$\langle \dot{\sigma}_- \rangle = -i\omega_a \langle \sigma_- \rangle - \tfrac{i}{2}\Omega e^{-i\omega_a t} \langle \sigma_z \rangle - \gamma_2 \langle \sigma_- \rangle \tag{2.30c}$$

These are known as the optical Bloch equations, where here we have included the decay of energy (γ_1) and phase (γ_2) – see table 2.2.

2.2.2.5 Absorption spectrum and power broadening

The linewidth of an emitter may be defined and measured in several different ways. For example, the emitter may be excited resonantly and the scattered field separated in energy by a grating, obtaining the emission spectrum. Alternatively, a narrow laser, much less than the linewidth, may be frequency scanned across the emitter. In the latter case we obtain the frequency dependence of the absorption cross-section – the absorption spectrum $s_{abs}(\omega_l)$ – which is proportional to the excited state population as a function of laser frequency: $\rho_{ee}^{t\to\infty}(\omega_l)$. It is then given (semi-classically) by [64, p. 77]

$$s_{abs}(\omega_l) \propto \rho_{ee}^{t\to\infty}(\omega_l) = \frac{\Omega^2/(2\gamma_1\gamma_2)}{1 + ((\omega_l - \omega_a)/\gamma_2)^2 + \Omega^2/(\gamma_1\gamma_2)}. \tag{2.31}$$

The absorption cross-section is a Lorentzian with a power-dependent energy FWHM equal to $2\hbar\gamma_2\sqrt{1+\Omega^2/(\gamma_1\gamma_2)}$. At low power, $\Omega^2 \ll \gamma_1\gamma_2$, this gives the linewidth $2\hbar\gamma_2$. However, at high power, $\Omega^2 \gg \gamma_1\gamma_2$, the linewidth becomes $\propto 2\hbar\Omega$, and the excited state attains a maximum average population of $\frac{1}{2}$.

2.2.2.6 The quantized field and dressed states

We have so far been treating the radiation field in a classical manner. In the quantized picture, the system Hamiltonian H_S is the sum of the Hamiltonians for the 2LS, the field, and for their interaction [67, p. 190]. A fully quantized version of Hamiltonian (2.23) then reads:

$$H_S = \tfrac{1}{2}\hbar\omega_a\sigma_z + \hbar\omega_a a^\dagger a + \hbar g(a\sigma_+ + a^\dagger\sigma_-) \tag{2.32}$$

where $a^\dagger$ and a are the creation and annihilation operators of the field mode, and the 2LS is coupled to the mode with an angular frequency g. This coupling frequency is also known as the single-photon Rabi frequency, although, comparing with equation (2.23), we see that under these definitions $\Omega = 2g$.

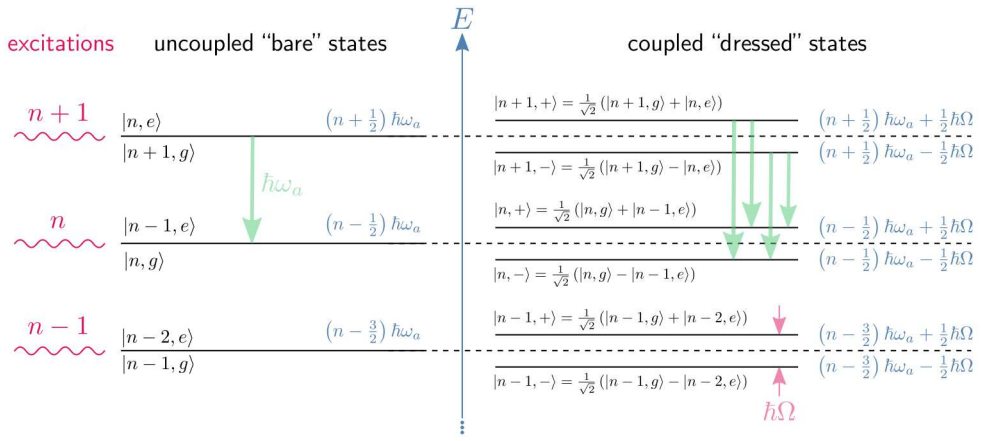

FIGURE 2.3. *The dressed states of the coupled 2LS and resonant field. The splitting of the bare energy states into pairs gives rise to four possible transitions down the Fock ladder. One of these transitions is a Rabi energy higher than the bare transition energy, and one is a Rabi energy lower – this results in the Mollow triplet (figure 2.4).*

We now treat the incident laser field as constructed from n-photon Fock states $|n\rangle$ with energy $E_n = n\hbar\omega_l$*. For an uncoupled resonant field the "bare" states $|n\rangle\,|g\rangle$ and $|n-1\rangle\,|e\rangle$ are degenerate – they both contain an energy $\left(n-\frac{1}{2}\right)\hbar\omega_a$. However the coupling of the 2LS and the field removes this degeneracy, and an *avoided crossing* appears in the structure of the system. At resonance, and for each Fock state of the incident field, the eigenstates of the coupled system become even and odd superpositions of the respective "bare" states. These polaritonic *dressed states* are given by

$$|n,\pm\rangle = \frac{1}{\sqrt{2}}\left(|n,g\rangle \pm |n-1,e\rangle\right), \tag{2.33}$$

with corresponding energies for high n of

$$E_{n,\pm} \approx \left(n-\tfrac{1}{2}\right)\hbar\omega_a \pm \tfrac{1}{2}\hbar\Omega. \qquad \text{[J]} \tag{2.34}$$

The states of the coupled system are now in pairs for each Fock state of the field, with the constituents of each pair separated in energy by $\hbar\Omega = 2\hbar g$, as shown in figure 2.3.

*The zero for energy is as before.

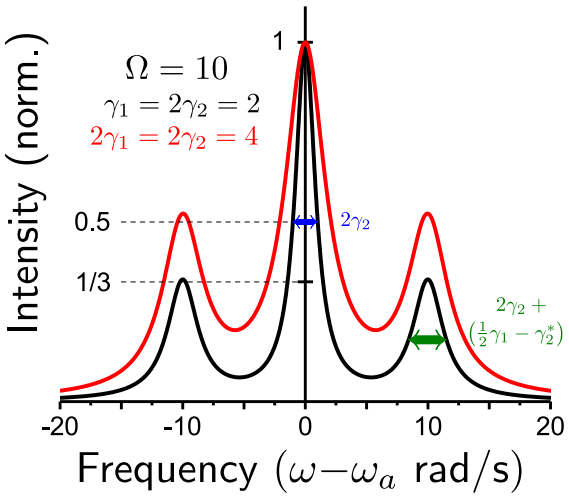

FIGURE 2.4. *The incoherently scattered spectrum showing the Mollow triplet for the lifetime-limited case $\gamma_1 = 2\gamma_2$, and also for $\gamma_1 = \gamma_2$. Here the parameters Ω, γ_1, and γ_2 are given in units of* $\mathrm{rad\,s^{-1}}$*, but it is the relative values which are of importance.*

2.2.2.7 Scattered spectrum

Now we consider the spectrum of the fluorescence* when a resonant monochromatic field is incident upon the 2LS. In a quantum mechanical treatment, the scattered light consists of two parts, namely coherent and incoherent scatter [68], and each component has a signature spectrum [69]. The incoherent part arises from the SE – a photon is absorbed and re-emitted. In the case of coherent scattering, also known as resonant Rayleigh scattering (RRS)†, the 2LS is not excited and the scattered field has the same coherence as the incident field. However, the statistical properties do change – the coherent scatter is still antibunched on the time scale of the excited-state lifetime T_1.

Incoherent spectrum Although the incoherent scatter arises from ordinary SE, its spectrum is not simply that of the freely decaying 2LS encountered above. The incident field is affected by its interaction with the 2LS, which damps both its energy and phase,

*Here by *fluorescence* we mean all of the scattered field that has interacted with the 2-level system, both elastically and inelastically. Some authors reserve *fluorescence* for inelastic processes that involve absorption and re-emission, e.g. [64].

†Although here mostly the terms *coherent scattering* and *resonant Rayleigh scattering* are used interchangeably, in other works the same process may also be referred to as *elastic scattering* or the *Heitler regime*, e.g. [70].

so that [71]

$$\Omega_{\mathrm{d}} = \sqrt{\Omega^2 - \tfrac{1}{4}(\gamma_1 - \gamma_2)^2}, \qquad [\mathrm{rad\,s^{-1}}] \quad (2.35)$$

gives the damped Rabi frequency. When Ω is large enough that the damped Rabi frequency becomes real, the coupled system is split into the dressed states as described in the previous section (and as shown in figure 2.3). We then have three possible transitions, of frequencies $\omega_a - \Omega_{\mathrm{d}}$, ω_a, and $\omega_a + \Omega_{\mathrm{d}}$. The incoherent spectrum $s_{\mathrm{inc}}(\omega)$ then consists of three Lorentzians known as the *Mollow triplet*:

$$\begin{aligned} s_{\mathrm{inc}}(\omega) \propto \frac{1}{2}\frac{\gamma_s}{\frac{1}{4}\gamma_s^2 + (\omega - \omega_a - \Omega_{\mathrm{d}})^2} + \frac{\gamma_c}{\frac{1}{4}\gamma_c^2 + (\omega - \omega_a)^2} \\ + \frac{1}{2}\frac{\gamma_s}{\frac{1}{4}\gamma_s^2 + (\omega - \omega_a + \Omega_{\mathrm{d}})^2}, \end{aligned} \quad (2.36)$$

where, with the addition of phase damping we have [65, 72]

$$\gamma_c = 2\gamma_2 \qquad [\mathrm{rad\,s^{-1}}] \quad (2.37a)$$

$$\gamma_s = 2\gamma_2 + (\tfrac{1}{2}\gamma_1 - \gamma_2^*) \qquad [\mathrm{rad\,s^{-1}}] \quad (2.37b)$$

for the FWHMs of the central and side peaks respectively. This suggests that $\frac{3}{2}$ is the maximum width of the side-peaks relative to the central peak, and for higher rates of pure dephasing the linewidth decreases (relative to the central). Nevertheless the side-peaks still contain half the incoherent scatter and thus their relative amplitude increases as their relative linewidth decreases, so that they may become more prominent. The Mollow triplet is shown in figure 2.4 for the lifetime-limited case $\gamma_1 = 2\gamma_2$, and also for $\gamma_1 = \gamma_2$.

Coherent spectrum The coherent spectrum is given by

$$s_{\mathrm{coh}}(\omega) \propto \delta(\omega - \omega_a), \quad (2.38)$$

i.e. it is a delta function about the central frequency ω_a. A real laser is not perfectly monochromatic, and the coherent scatter is not a delta function but has the linewidth and coherence of the laser.

Total spectrum The total scattered spectrum is then the sum of the coherent and incoherent spectra. The relative intensities of the two components is determined by the degree to which the 2LS is saturated, and as such is a function of Ω, γ_1 and γ_2, and the

laser detuning $\omega_a - \omega_l$. For zero laser detuning, the ratio of the coherent scatter intensity I_{coh} to the total (coherent plus incoherent) I_{total} is given by

$$\frac{I_{\text{coh}}}{I_{\text{total}}} = \frac{\gamma_1}{2\gamma_2} \frac{1}{1 + \Omega^2 / (\gamma_1 \gamma_2)}. \tag{2.39}$$

Recalling that $\gamma_1 \leq 2\gamma_2$, with the equality holding in the lifetime-limited case, it follows that a high fraction of coherent scatter is only possible when the system is close to the lifetime limit of coherence. At this limit

$$\frac{I_{\text{coh}}}{I_{\text{total}}} = \frac{1}{1 + 2\Omega^2 / \gamma_1^2}, \tag{2.40}$$

giving an independent measure of γ_1, and hence also T_1, provided Ω is known.

2.2.2.8 Scattered power

In all cases the scattered power

$$P = \Gamma_1 \hbar \omega_a \langle e | \rho_{ss} | e \rangle , \qquad \text{[W]} \tag{2.41}$$

where ρ_{ss} is the steady state value. This shows that, even in the low Ω regime, where most of the scattered field is elastically scattered without exciting the 2LS, the total scattered power is still determined by the excited state's average occupation and lifetime. Indeed, the coherent scatter is antibunched just as the SE is, with the timescale given by Γ_1 – a rather interesting and counter-intuitive result.

We investigate the resonant interaction of a field and a QD in a nanocavity in chapter 6. We observe the Mollow triplet at high powers, and at low powers we see a large fraction of coherent scattering. Together these, along with the equations described above, allow us to determine T_1 and T_2 for the system.

2.2.3 2-level system with a (near-)resonant field in a cavity

We now move into the regime of cavity quantum electrodynamics (cavQED), where the addition of a cavity can enhance the field amplitude to the point where single-photons—or even the vacuum field—have obvious effects.

A single-mode cavity confines one mode of the electromagnetic field to an effective volume V_m. The degree of confinement is given by the quality factor $Q = \omega_c / (2\kappa)$, where ω_c is the mode's central angular frequency, and 2κ its linewidth in angular frequency*.

*The factor of 2 is maintained because we are using the convention that there are two loss channels (ordinarily two cavity mirrors), each with a corresponding κ.

Recall that the coupling constant $g = \mu\mathcal{E}$. With the cavity confinement

$$g = \sqrt{\frac{\omega_c \left|\vec{\epsilon}(\vec{r}_0) \cdot \vec{\mu}\right|^2}{2\hbar\varepsilon_0 n^2 V_m}} \qquad [\mathrm{rad\,s^{-1}}] \quad (2.42)$$

where $\vec{\epsilon}(\vec{r}_0)$ is the field at the dipole position $\left(\vec{\mathcal{E}}(\vec{r}_0)\right)$ normalized to the cavity field maximum ($\vec{\mathcal{E}}_{\max}$), and we have given the cavity a refractive index n. From this we see that as the mode volume is reduced the coupling is increased, which is a consequence of the fact that the electric field amplitude of a photon is enhanced if it is confined to a smaller region. The qualitative effect of the cavity on the resonant dynamics is determined by the interplay of three processes: emitter decay (γ_1), cavity decay (2κ), and the coupling between emitter and cavity (g). By looking at the different possible limits of the relative magnitude of these three variables, we can identify different dynamical regimes. When [73]

$$16g^2 < (2\kappa - \gamma_1)^2, \quad (2.43)$$

we say the system is *weakly coupled*, and when the inequality doesn't hold we say the system is *strongly coupled*. We will now examine these regimes in more detail.

2.2.3.1 Weak coupling regime

In the weak coupling regime, system losses are greater than system interactions. Damping due to both cavity losses and emitter losses means that the system decays before the emitter and cavity have time to repeatedly interact. However, the cavity modifies the electromagnetic field mode by confining it, and this increases its amplitude and therefore interaction with the embedded dipole. One result of the increased interaction is an enhanced spontaneous emission rate.

In the *small-solid angle approximation*, the cavity is assumed to be approximately one-dimensional, enhancing a single spatial mode but leaving the bare decay rate Γ_r^b essentially unaffected. Then the enhanced decay rate is $\Gamma_r^{cav} = \Gamma_r^b(1 + F_{\mathrm{P}})$, where F_{P} is the *cavity Purcell factor* [74], and in this case is also the *spontaneous emission enhancement factor* due to the cavity. This approximation is often acceptable in macroscopic optical cavities. However in single-mode microscopic cavities, such as the photonic crystal cavities (PhCCs) that we will study later, the cavity occupies almost all the surrounding space, and the *large-solid angle approximation* may be more valid – when the free space modes are unavailable, we have $\Gamma_r^{cav} = \Gamma_r^b(0 + F_{\mathrm{P}})$, so that $F_{\mathrm{P}} = \Gamma_r^{cav}/\Gamma_r^b$. One consequence of the latter case is the possibility of an inhibited spontaneous emission rate when $F_{\mathrm{P}} < 1$

[75–77]. This occurs when the emitter is detuned far from the cavity mode, reducing the cavity mode interaction.

Including the detuning and spatial overlap of the 2LS with respect to the cavity mode, the cavity Purcell factor F_P is given according to [78]:

$$F_P = \frac{3Q}{4\pi^2 V_m} \frac{(2\kappa)^2}{4(\omega_a - \omega_c)^2 + (2\kappa)^2} \frac{|\vec{\mu} \cdot \vec{\mathcal{E}}(\vec{r}_0)|^2}{|\vec{\mu}|^2 |\vec{\mathcal{E}}_{\max}|^2} \tag{2.44}$$

where V_m is given in cubic wavelengths.

At zero dipole-cavity detuning and for perfect dipole positioning and orientation, the Purcell factor is

$$F_P = \frac{3}{4\pi^2} \frac{Q}{V_m} = \frac{2g^2}{\kappa\gamma_1} = 2C, \tag{2.45}$$

where C the cooperativity. In chapters 6 and 7 we investigate a QD-nanocavity system that displays a very high coupling with a relatively high cavity loss rate. The result is a large Purcell factor in the weak coupling regime. We will return to these equations in 7 in order calculate the relevant system parameters.

2.2.3.2 Strong coupling regime

This is also known as the regime of vacuum Rabi splitting [79], since when inequality (2.43) does not hold, the system is always observed to have a Rabi splitting. Even the presence of a single-photon splits the excited state and we have emission at the frequencies $\omega_a + g$ and $\omega_a - g$, giving the vacuum Rabi doublet. If the dipole energy is tuned across the cavity mode, an avoided crossing will be observed.

2.2.3.3 Saturation photon number

If we are dealing with an enhanced photon interaction with the 2LS, we might ask how many photons are needed in the cavity, on average, in order to maintain a saturated transition. The saturation photon number n_0, is given by [80, 81]

$$n_0 = \frac{\gamma_2 \gamma_1}{4g^2}. \tag{2.46}$$

Clearly the higher the coupling rate relative to the dipole decay rates, the lower the number of photons in the cavity at saturation. It may seem strange that this expression does not contain the cavity decay rate 2κ. Changing 2κ does not change the average number of photons at saturation, however a higher 2κ will require a higher photon flux into and out of the cavity in order to maintain n_0. This may be important in terms of the signal-to-noise ratio, especially for on-chip applications.

2.2.3.4 Master equation for resonance fluorescence with coherent driving of a cavity mode

We arrive at the final Lindblad-form master equation that we will consider [62, p. 210]:

$$\begin{aligned}\dot{\rho} = &-\frac{i}{2}\omega_a[\sigma_z,\rho] - i\omega_c[a^\dagger a,\rho] \\ &+ g[a^\dagger\sigma_- - a\sigma_+,\rho] - i[\bar{\mathcal{E}}_0 e^{-i\omega_l t}a^\dagger + \bar{\mathcal{E}}_0^* e^{i\omega_l t}a,\rho] \\ &+ \frac{\gamma_1}{2}(2\sigma_-\rho\sigma_+ - \sigma_+\sigma_-\rho - \rho\sigma_+\sigma_-) + \frac{\gamma_2^*}{2}(\sigma_z\rho\sigma_z - \rho) \\ &+ \kappa(2a\rho a^\dagger - a^\dagger a\rho - \rho a^\dagger a).\end{aligned} \tag{2.47}$$

It is valid for 2LS cavity quantum electrodynamics (QED) with coherent driving of the cavity mode. It is used to investigate a variety of phenomena in chapter 7.

2.2.4 Other processes

As stated previously, the system is assumed to be at 0 K. We have avoided considering the effects of phonons on the evolution of the system. Although they can modify the dynamics in interesting and significant ways not far above 0 K, we will not need to consider them for the theoretical treatment of the described experiments. In chapter 6, however, they make clear modifications to the emission spectrum.

CHAPTER 3

III-V ARCHITECTURE FOR QUANTUM OPTICS & QUANTUM INFORMATION

Linear optical quantum circuits are but one way of realizing quantum information carrying and processing. And the fundamental components of such a circuit can themselves be realized physically in a number of ways. This chapter concerns the theory of the components of an on-chip linear optical quantum circuit based on a III-V semiconductor architecture, and the basic interactions within it. The main results of the previous chapter—single-photon states, spontaneous emission enhancement [82], strong-coupling [83], coherent scattering—can all be achieved on the nanoscale with photonic integrated circuits (PICs), paving the way towards scalable quantum optical circuits.

3.1 Fitting linear-optical quantum computing on a chip

Although all of the fundamental components of linear-optical quantum computing (LOQC) were quickly demonstrated experimentally, and even though operational gates could be constructed, the problem with these early tabletop demonstrations was scalability. Indeed, scalability is the primary issue facing quantum computing in general. In some cases this may due to difficulties in maintaining quantum coherence as the number of qubits increases, but in the case of the probabilistic measurement-based LOQC, the difficulty is in the size, number, and efficiency of components that is needed. Hence the

Component	Implementation	In this thesis
Single-photon sources	In(Ga)As quantum dots	Chapters 5, 6, 7, and 8
Waveguides	GaAs ridges and nanobeams; photonic crystal waveguides	Chapters 5, 6, 7, and 8
Beam splitters	Directional couplers, multi-mode interferometers	Chapters 5 and 8
Phase shifters	Electro-optic modulators; temperature-tunable pads; microelectromechanical systems	–
Spectral filters	1D photonic crystal cavities in waveguides	Chapter 8
Single-photon detectors	Waveguide-coupled superconducting nanowire single-photon detectors	Chapter 8

TABLE 3.1. *How the fundamental LOQC components may be realized in this III-V architecture, and the relevant chapters in this thesis.*

move towards integrated waveguide circuits [45], of which the two main wafer materials are silicon and the III-V semiconductor Gallium Arsenide (GaAs) [84, 85]. Both systems have relative advantages and disadvantages, with the silicon platform's most severe disadvantage being the lack of a direct electronic band gap and the resulting difficulty in producing on-chip on-demand single-photon sources. GaAs readily supports sources that produce sub-μm photons, whereas silicon is restricted to $> 1.1\,\mu m$. Thus GaAs is more compatible with silicon single-photon avalanche diodes (SPADs), while silicon is more compatible with the best fiber technology.

In the III-V architecture we have quantum dots as single-photon sources, etched GaAs as waveguides and cavities, and nanowires as on-chip detectors. Table 3.1 gives a simple overview of the architecture, and in the rest of the chapter we explore this in more detail.

3.2 Semiconductor quantum dots

The key advantage of III-V semiconductors is the existence of a direct band gap that enables efficient photon absorption and generation. When a three-dimensional confining potential is introduced by embedding a nanoscale amount of some material (InAs) within another material of larger band gap (GaAs), we create an optically active artificial

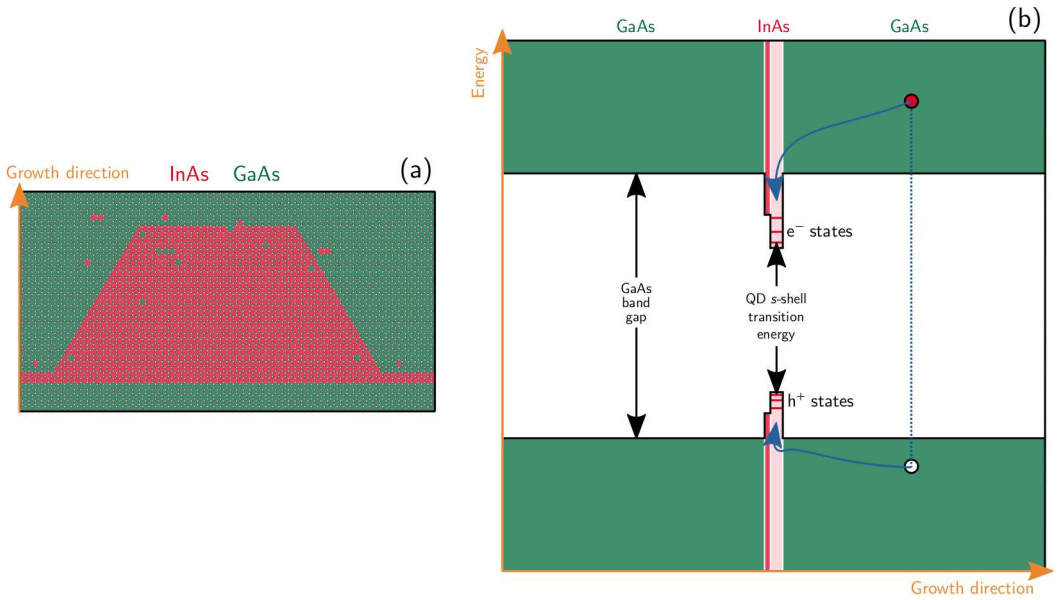

FIGURE 3.1. *(a) A Stranski–Krastanov In(Ga)As quantum dot is a pyramidal island, consisting of hundreds of thousands of atoms, that sits atop a relatively thin "wetting layer" of InAs. It is surrounded by GaAs. (b) This structure creates a 3D potential well with quantized atom-like energy levels.*

atom known as a quantum dot (QD).

3.2.1 Growth

The QDs that we will be concerned with are of the Stranski–Krastanov (SK) type. These are defined by a growth method in which a layer of InAs is deposited slowly onto a GaAs substrate. The lattice mismatch of the two materials results in a strain, and after no more than a few complete layers of InAs (the wetting layer), the InAs begins to self-assemble into nanoscale pyramidal islands. These are then capped with more GaAs. The final structure is a truncated pyramid consisting of hundreds of thousands of atoms, figure 3.1(a). In practice, some intermixing occurs so that we end up with InAs/GaAs QDs, often referred to as In(Ga)As QDs. The advantage of SK QDs is their high emission rate and coherence. The disadvantage is that the growth method results in random variation in the size and position of the QDs, creating a challenge for scalability.

3.2.2 Electronic states

The three-dimensional confinement results in an atom-like potential for the electrons, figure 3.1(b). In the electron-hole picture, an electron (e^-) excited from the valence to conduction band leaves behind a positively charged quasiparticle called a hole (h^+). If the two particles are bound by a Coloumb interaction, they are known as an exciton (X). Because of the small spatial extent of a QD, an electron excited within it predominantly forms an exciton rather than an unbound electron and hole. Light-holes relax to heavy-hole states, and so the lowest energy exciton is the electron–heavy-hole exciton. An alternative way for the QD to become populated is through the creation of high-energy excitons or (initially) unbound electron-hole pairs, which then lose energy and become trapped in the potential well. The neutral (electron–heavy-hole) excitonic state $|X\rangle$ and crystal ground state $|g\rangle$ are the upper and lower levels of the fundamental radiative two-level system (2LS) in this architecture.

3.2.2.1 Neutral exciton degeneracies

The system deviates from the ideal 2LS in a number of ways. Firstly, the neutral excitonic state is composed of two spin-half particles, an electron and a (heavy) hole, and these can both have spin either up or down. For example, if the hole has spin up and the electron spin down, we have the state $|\Uparrow\downarrow\rangle$. The energy eigenstates are superpositions of the spin states, so that the four energy states are:

$$\frac{1}{\sqrt{2}}\left(|\Uparrow\downarrow\rangle + |\Downarrow\uparrow\rangle\right) \tag{3.1a}$$

$$\frac{1}{\sqrt{2}}\left(|\Uparrow\downarrow\rangle - |\Downarrow\uparrow\rangle\right) \tag{3.1b}$$

$$\frac{1}{\sqrt{2}}\left(|\Uparrow\uparrow\rangle + |\Downarrow\downarrow\rangle\right) \tag{3.1c}$$

$$\frac{1}{\sqrt{2}}\left(|\Uparrow\uparrow\rangle - |\Downarrow\downarrow\rangle\right) \tag{3.1d}$$

The first two states are known as the bright states because they are able to make a radiative transition to the ground state. The remaining two are known as dark excitons because they are forbidden from relaxing via such optical emission. These properties arise from selection rules – only certain sets of quantum numbers for the initial and final states will result in a non-vanishing electric-dipole matrix element [54, p. 55]. The bright and dark doublets are split by the dark-bright energy splitting [86, 87]. Because we are interested in photonic states, we are primarily concerned with the bright states.

Although the dark and bright states may interact via spin flips, these processes normally occur on a timescale much longer than that of radiative decay [88–90], and for the most part we can ignore the existence of the dark states. In typical SK In(Ga)As dots the bright states have a fine-structure splitting (FSS) of several μeV to several hundred μeV [91, 92]. The degeneracy of the states is lifted by the structural asymmetry of the QD, with the large range resulting from growth variation. When we talk of the neutral exciton in the 2LS approximation, we generally only consider the ground state and a bright exciton.

3.2.2.2 Other states

In addition to the aforementioned ground and neutral excitonic states, a QD may contain a single excited electron or hole. This can occur, for example, when an exciton is created in bulk and the electron and hole relaxation times differ, or in multi-layer structures if the tunnelling rates differ. Then the electron must wait for the hole to relax, or vice versa, before recombination can occur [93]. Additional excited charge carriers may be present alongside a neutral exciton, so that we have a negative trion (X^-) when there is an extra electron, and a postive trion (X^+) when there is an extra hole. When two excitons are present, we have a biexciton (XX) [94–96]. Because of the Pauli Exclusion Principle, the spin state must be $|\Uparrow\Downarrow\uparrow\downarrow\rangle$. The biexciton decays to the exciton and then the ground state.

Thus far we have been considering electrons and holes in the first excited state, which from atomic physics is often called the s-shell. Just as with electrons in atoms, electrons and holes in dots may be further excited to p, d, f, etc., shells [97, 98]. These tend to lie from a few meV to a few tens of meV above the s-shell, until they eventually merge with the InAs wetting layer.

3.2.3 Carrier dynamics

In addition to knowing the electronic states, we need to be aware of the state dynamics, i.e. whether the electrons (and holes) can move between the states, what mediates the transition, and the typical timescales and linewidths of these transitions. For a transition to occur with significant probability it must be energetically allowed and adhere to selection rules. The mediator may for example be the optical field, phonons [99, 100], spin flips [101], or spin precession. In certain cases, tunnelling of carriers may be a significant source of population change [102].

Normally it is desirable that the carrier dynamics solely consist of fast relaxtion to the s-shell, and s-shell radiative recombination. In chapter 7 we will see that for the sample in question, this is not the case, and so there is a clear difference between

resonant *s*-shell and non-resonant excitations in the time-resolved photoluminescence (TRPL). Throughout the experiments we find that the emission rate and coherence under resonant excitation differs in favourable ways from quasi- or non-resonant methods.

3.2.4 Optical properties

An excitonic state is quasistable, and after a period of time the excited electron will fall back into the vacant state that it left, a process known as electron-hole recombination. In radiative recombination, this accompanies the emission of a photon. The two bright states emit linearly polarized photons that are orthogonally polarized to each other. If the FSS is smaller than the linewidth, the emission from the degenerate states is circularly polarized, and the biexciton cascade produces two photons of different energy but which are entangled [103, 104]. If the FSS is larger than the linewidth, the cascade may go through either of the bright excitons, and the two photons always share the same linear polarization. The trions have no FSS, and so when recombination occurs, circularly polarized light is emitted, leaving the additional excited carrier. The helicity of the emission is dependent on the spin of the additional carrier, and the degeneracy of the two spin states (at zero magnetic field) results in (on-average) unpolarized emission [105, 106].

The temporal and spectral properties of QD emission are well described by the theoretical treatment given in section 2.2.1. As such, in the ideal case we have monoexponential decay, a Lorentzian lifetime-limited lineshape, and antibunched single-photon statistics. In chapter 5 we will see the effect of uncorrelated electrons and holes on the $g^{(2)}_{\mathrm{HBT}}(\tau)$ resulting from recombination in a trion, and how this varies between wetting layer and *p*-shell excitation. The QD investigated in chapters 6 and 7 is a neutral exciton with FSS, with the two linear emission channels each aligned to a linear polarized nanocavity mode.

3.2.5 Environmental effects

Embedding our single-photon sources (SPSs) in a solid state environment, while crucial for scalability, presents difficulties. To exploit quantum effects, we need to shield the system from interactions with its larger environment. Such interactions affect the state occupations and phases in a random way, and constitute what is known as *decoherence* – and any quantum information processing (QIP) protocol will fail under severe decoherence because the quantum state will evolve in an unpredictable and useless way. Having our light source as part of a macroscopic crystal lattice opens the door to

lattice interactions (phonons), which may make the source unusable except at extremely low temperatures. One way to mitigate these effects is by reducing the emitter lifetime through the Purcell effect to far below that of dephasing timescales – this is explored in chapters 6 and 7.

3.3 Guiding light

Like an electrical chip, a photonic chip needs to be able to guide its information carriers around in complex nanoscale networks. Here, this can be achieved by exploiting the large refractive index contrast between GaAs and the surrounding vacuum, creating waveguides of sub-wavelength thickness but of arbitrary length and complexity. Additionally, they may be evanescently coupled to create beam splitters (BSs) of arbitrary splitting ratio.

3.3.1 Single-mode nanobeam waveguides

Fundamentally we want to guide light around the circuit in a single mode with a low loss rate. This can be achieved with a nanobeam waveguide, where the wafer is etched to leave a freestanding "optical wire" of the material, cladded on all sides by the vacuum. The high index contrast of GaAs ($n \sim 3.4$ at 4 K) and the vacuum ($n \sim 1$) enables efficient confinement via total internal reflection. If the dimensions are chosen so that only one polarization mode is supported, then we have a single-mode waveguide. With these materials, and at (free space) wavelengths of $\sim$900 nm, this can be achieved using a waveguide depth of 140 nm and a width of 280 nm, as used in chapters 5 and 8.

Losses may occur through absorption or scattering. The absorption into GaAs is weak (below its band gap) and realistically a much greater amount of loss occurs through the sidewalls of the waveguide, especially where fabrication imperfections have produced roughness and other defects for the light to scatter off.

3.3.2 Directional coupler

A directional coupler (DC) is formed by bringing two waveguides into close proximity so that the evanescent field modes overlap. When this occurs we no longer have individual waveguide modes, but two "supermodes" that encompass both waveguides, as shown in figure 3.2. The symmetric and antisymmetric supermodes have different amplitudes inside (and outside) the waveguides, and so have different refractive indices and phase velocities through the coupled region. A photon incident from one waveguide excites a

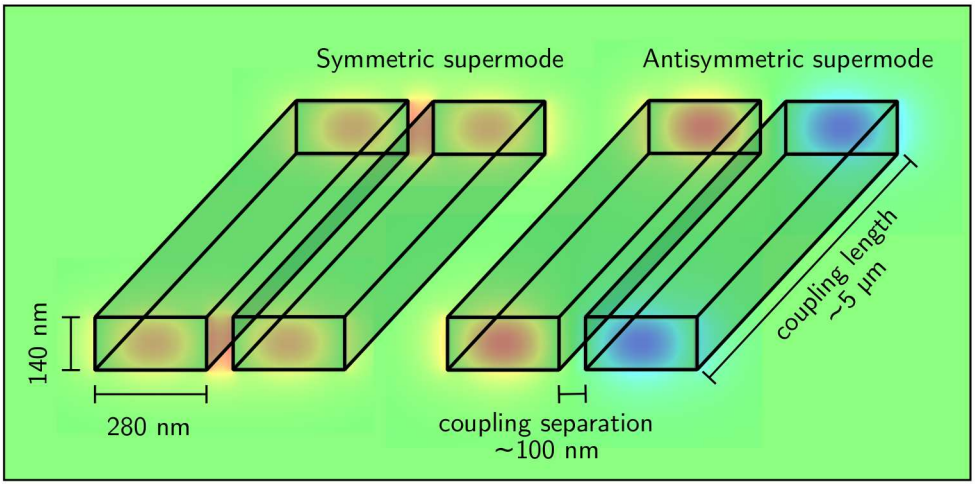

FIGURE 3.2. *When two single-mode waveguides are brought together, so that their evanescent fields couple, the result is the two "supermodes" of the directional coupler. Optical power transfers between the individual waveguides.*

superposition of the supermode states. If the parameters of the coupling region—length, separation, depth, thickness—are such that at the end the phase difference between the two supermodes is $\pi/2$, the device acts as a 50:50 beam splitter. In particular, if the effective refractive index difference between the supermodes is Δn, a mode of free-space wavelength λ_0 entering through one input will be in an equal superposition of both waveguide modes after a length

$$L_{50:50} = \frac{\lambda_0}{\pi \Delta n} \arcsin\left(\sqrt{0.5}\right). \tag{3.2}$$

Free-standing single-mode DCs have been integrated with SPSs [107]. Rib waveguide directional couplers have also been demonstrated [108] with single-mode operation [109]. The DC is a major component of the devices investigated in chapters 5 and 8.

3.4 Photonic crystals

The previous section examined components which operated on the principle of total internal reflection. A photonic crystal, in contrast, uses interference to produce the desired modes and remove undesired modes. The formation of a photonic band gap means that, in the ideal case, light can be guided without any absorption [110]. For if a defect is introduced, such as by removing a line of holes, the mode is supported within

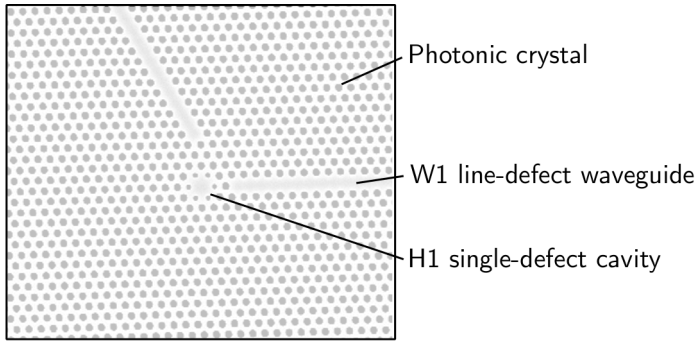

FIGURE 3.3. *An example of a photonic crystal with purposeful defects.*

the defect, and forbidden outside it. The use of photonic crystal defects to construct nanophotonic circuits for a variety of applications is reviewed in [111].

Examples of defects are shown in figure 3.3. In fact this is the structure that is measured in chapters 6 and 7. Although here the cavity-coupled waveguides are produced by creating W1 line-defects in photonic crystals (PhCs), they are interfaceable with the nanobeam waveguides discussed above and used in chapters 5 and 8. This allows us, in principle, to combine the cavity system with the DC devices. Additionally, in 8 we show a device that transitions from nanobeams to W1 waveguides and back again – the W1s are used as structural support for the suspended nanobeams. Advanced circuits will likely exploit the capabilities of both systems in these ways.

3.5 Grating couplers

At least at this stage of III-V development, it is often necessary to couple light on and off the chip. If the QD is to be optically excited, we need to guide a laser onto the sample, for example. And if the photoluminescence (PL) is in a waveguide mode, then, in the absence of on-chip detectors, we need to couple it off chip in order to measure it. Sometimes it is possible to couple light on and/or off chip in the plane of the device, and this is known as *edge coupling* – but often this is not possible, or else there are too many devices to make it practical. The solution is to use *surface coupling* devices like grating couplers [112]. These use an in-plane Bragg stack to destructively interfere the propagating mode and scatter the light in the vertical plane. As the light may equally be scattered upwards or downwards, a reflective coating may be added to the substrate beneath in order to gather more light. The sacrificial AlGaAs layer seen in all structures

FIGURE 3.4. *The grating design used for devices in chapters 5 and 8.*

in this thesis has a depth such that constructive interference should occur in the upwards scattering direction. Such structures are able to produce modes propagating vertically enabling efficient coupling to lenses and optical fibers.

All of the samples in this thesis make use of semi-circular $\lambda/2n$ gratings similar to that in [113]. In chapters 5 and 8, a slightly modified version with an additional period and expanded waveguide end is used. This design is shown in figure 3.4. In measurements not shown, it was found to have approximately double the coupling efficiency of the standard design, which has a $\lambda/2n$ waveguide end region and one less period. Increasing the waveguide end region further to $5\lambda/2n$ was found to offer no further improvement over $3\lambda/2n$, while a second additional period negatively affected coupling. It should be noted however that the in and out coupling will be affected by the spot size, objective lens numerical aperture, beam angle, etc., and so it is difficult to state absolutely a particular design's superiority. Another consideration is that this modified design was found to also increase the degree of reflection back into the waveguide, which could be restrictive for some applications. The device in chapters 6 and 7 uses the standard design.

3.6 Diodes

Being a semiconductor, GaAs can be positively or negatively doped, and the components described above can all be fabricated within diode structures. This enables electrical control of various parameters and functions. Diode structures are used to tune QD emission energies via the quantum-confined Stark effect (QCSE) in chapters 6 and 7,

and in chapter 8 we explore some possible future applications of electrical control. One of these is electroluminescence (EL), where the QDs are excited electrically rather than optically.

3.7 Hybrid systems

The unit of interest in QIP is the qubit, and what physical form it takes during the computation is irrelevant. Thus we have the possibility of hybrid systems, where the qubit may mutate between various forms as it travels the circuit, taking the advantages that each form offers when appropriate. In GaAs architecture using QDs, one form could be the spin of the exciton in the QD. Morphing between "flying" photonic and "static" spin qubits is one avenue of hybridization [38, 114, 115]. In this case it is necessary to design the structures such that spin states are converted to path states, and vice versa. Such coupling is possible between QDs and both types of waveguides – nanobeams and W1s – used in this thesis [116, 117]. Assembling hybrid plasmonic-dielectric components is also being explored [118].

Part II

Research

This part of the thesis contains some of the research performed over the course of the PhD. Chapter 4 introduces computational and experimental methods which are generally applicable to all of the research. Chapter 5 describes the interference between a quantum dot and a laser using an on-chip beam splitter. In chapter 6, coherent scattering from a quantum dot in a cavity is guided on-chip and demonstrates that the source has lifetime-limited coherence. Chapter 7 then investigates the same waveguide-coupled quantum dot–cavity system's performance as an on-chip on-demand single-photon source, with discussion of general aspects of such sources under pulsed excitation. Finally, chapter 8 looks at the further integration of essential on-chip linear-optical quantum computing components, including single-photon sources, beam splitters, filters, and on-chip superconducting nanowire single-photon detectors.

CHAPTER 4

METHODS

In this chapter we briefly describe some important computational, fabrication, and experimental methods that are generally applicable to the work in the chapters which follow. We begin with the computational methods used to simulate the properties and behaviour of the samples. Afterwards we look at how the samples are fabricated, and finally at how they may be measured.

4.1 Simulation tools

The first step in the experimental work is to perform simulations of the sample to be studied. This needs to be approached in a variety of ways. The devices are complex and have functional and behavioural properties that are sometimes best understood in different theoretical paradigms. For example, some properties of the light emission from a quantum dot (QD) require a quantum optics approach, but the propagation through waveguides and photonic crystals of arbitrary dimension cannot easily be simulated and studied in this way. Instead, we use Maxwell's equations. Maxwell's equations, however, are not very helpful when we consider the collection efficiency through a lens to an optical fiber mode. So even when considering purely optical properties, we have to move between theoretical regimes.

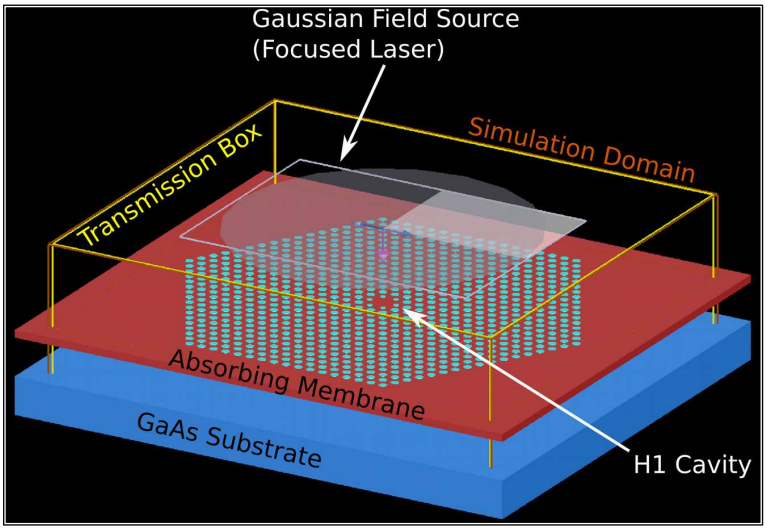

FIGURE 4.1. *Schematic of the FDTD simulation used to estimate the laser coupling efficiency for the sample in chapters 6 and 7 (Dr Rikki Coles).*

4.1.1 Finite-difference time-domain method

Although we wish to study and exploit quantum effects, the basic operation and behaviour of nanophotonic structures like waveguides and cavities is understood in terms of Maxwell's equations. These equations can be solved numerically for arbitrary structures and fields using the finite-difference time-domain (FDTD) method. In this technique, the structure is analyzed using a three-dimensional mesh. Each compartment defined by the mesh is treated as an individual block, and the solution at the boundaries is computed and iterated at finite time steps. A smaller mesh gives greater detail in the structure of the electromagnetic field, but requires greater computational resource.

FDTD was used to simulate the waveguide and directional coupler behaviour for the sample in chapter 5. These simulations were performed by Dr Nikola Prtljaga. The waveguide-coupled H1 sample investigated in chapters 6 and 7 was designed with the aid of FDTD by Dr Rikki Coles. In addition, the coupling into and out of the sample was also simulated. These simulations were performed using commercial-grade simulators [119] and commercial-grade eigenmode solvers [120]. Post-fabrication simulation was also useful to account for fabrication imperfections – in chapter 7 for example, we use the fabricated mode volume rather than the design.

4.1.2 Quantum Toolbox in Python (QuTiP)

To model the quantum behaviour of the light-matter system we require a suitable Hamiltonian. If we want to include dissipation and damping of the system we can for example solve a suitable Lindblad master equation for the system to find the evolution of the density matrix. The quantum toolbox in python (QuTiP) [121, 122] is a dedicated python package for quantum simulations and the solution of Hamiltonians and master equations.

In section 2.2.3.4 we arrived at the master equation for two-level system (2LS) cavity quantum electrodynamics (QED) with coherent driving of the cavity mode. To solve this in QuTiP, we first define the state space as a tensor product of the "atomic" state space and the field state space. For a 2LS the space is two-dimensional. For the field it is potentially infinite, so we must choose where to truncate the Fock space. Larger Fock spaces will be necessary for accurate representation of strong optical fields, but require more computational resource. Next we define the system Hamiltonian for the evolution of states in this space. For modelling of pulsed excitation, the Hamiltonian contains a time-dependent part corresponding to the incident pulse. Decoherence and damping is added to the system through the inclusion of collapse operators.

Once the state space, system Hamiltonian and collapse operators are provided, they may be solved with QuTiP's built-in solvers. The master equation solver calculates the time evolution of every element of the density matrix, and through that one can obtain expectation values of specified operators. It also possible to solve via the Monte Carlo method, where the system is "trialled" a number of times, with each run giving a single possible *quantum trajectory*. This may be useful if analytic solutions are not possible, or to see quantum jumps more directly.

QuTiP was used to model the behaviour of the cavity QED system—comprised of the single QD and waveguide-coupled H1 cavity—in chapter 7.

4.2 Sample fabrication

After a successful simulation of desired behaviour, the next step is to make the sample. A key advantage of semiconductor chip based quantum information processing (QIP) technology is that it borrows manufacturing methods from the well-established and continually advancing microprocessor industry. This has focused on silicon wafer growth and patterning for classical computing components, but the design and manufacturing approach is generally applicable to most chip technologies, including III-V

semiconductors.

4.2.1 Wafer growth

Naturally formed crystals often contain defects due to variable growth conditions and the presence of contaminants. Such defects are detrimental to the quality and reproducibility of device structure and performance. For this reason synthetic crystals are grown with an emphasis on clean conditions and controllable environmental parameters. In addition, for multi-layered structures like those used here, it is necessary to be able to grow crystals of different chemical composition on top of one another, often with monolayer precision. A growth method that meets these requirements is molecular beam epitaxy (MBE) [123, 124], and all the wafers used in this thesis were grown using this method by Dr Edmund Clarke at the National Epitaxy Facility in Sheffield.

4.2.2 Nanolithography

Once we have a suitable wafer, many nominally identical devices are patterned through nanolithography techniques. For the creation of the large diode structures, photolithography provides adequate resolution, but for the patterning of the nanoscale waveguides and photonic crystals we require electron beam lithography (EBL). In this case, and after the wafer is cleaned and heated to remove surface contaminants, it is spin-coated with an electron beam resist such as ZEP-520A. The sample is subsequently baked to improve adhesion of the resist to the surface, leaving a film of thickness $\sim 300\,\mathrm{nm}$. Then, under vacuum, the resist is exposed to an electron beam according to a designed pattern. For a "positive resist", of which ZEP-520A is an example, the electron beam targets regions which are to be etched away. A typical dose might be $70\,\mu\mathrm{C\,cm^{-2}}$ using a $30\,\mathrm{kV}$ beam. Feature sizes down to $\sim 10\,\mathrm{nm}$ can be defined in this way. The regions of resist that have been exposed to the electron beam experience chain-scission and become soluble in the developer solution o-Xylene. Once developed it is ready to be etched.

4.2.3 Etching

The developed resist protects selected parts of the surface from the subsequent inductively coupled plasma (ICP) reactive-ion etching (RIE) step. In this etching step, ions bombard the surface vertically from above, carving out the devices with vertical sidewalls. Afterwards, the remaining photoresist is decomposed with ultraviolet light and removed chemically with *N*-methyl-2-pyrrolidinone. The freestanding structures are

created through the removal of the $Al_{0.6}Ga_{0.4}As$ layer with a 40 % hydrofluoric acid solution. Lastly, the sample is rinsed with solvents.

4.2.4 Supercritical point drying

If the freestanding structures are of large aspect ratio, then it may be necessary to add an additional *supercritical point drying* step at the end. In this procedure, the liquid solvents used to clean the sample are purged with acetone. This is then diluted under pressure with liquid CO_2, which is subsequently further pressurized and heated to become supercritical. Upon reducing the pressure by venting the chamber, the CO_2 becomes gaseous and is expelled. This method dries the sample without exposing it to the anisotropic and destructive surface tensions of an evaporating liquid.

4.2.5 Finishing touches

When the wafer patterning has been completed, the final touches can be added. Often metal contact pads need to be evaporated onto the surface to enable electrical input and output. Again this is achieved using photoresist masks. The post-growth lithography and processing of the wafers was primarily performed by Dr Benjamin Royall, Dr Deivis Vaitiekus and Dr Christopher Bentham. Optical and scanning electron microscope (SEM) images are taken throughout the process to analyse the success of each step.

4.3 Experimental

4.3.1 Cryostats and optics

All of the experiments to be described were conducted using liquid helium based cooling systems. The more sensitive measurements were performed with the sample held in a liquid helium bath cryostat. This includes all of the measurements in chapters 5, 6, and 7. If long term positional stability is not crucial, a flow cryostat can be used – this was the case for photoluminescence (PL) maps in chapter 8.

4.3.1.1 Bath cryostat

The bath cryostat consists of a 90 l dewar and a 1.4 m long, 10 cm diameter insert tube. This is pumped to 1 mPa, before a small amount of helium gas is added to mediate heat exchange between the tube contents and the helium reservoir, and so the sample cools to approximately the temperature of liquid helium – about 4 K. The helium reservoir boils

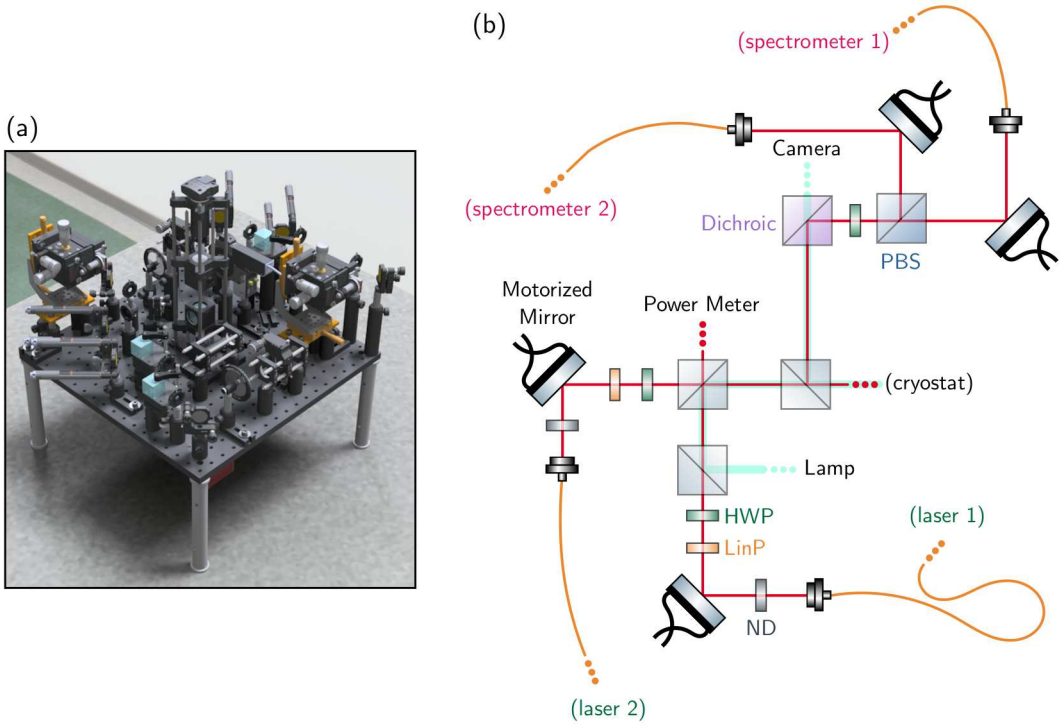

FIGURE 4.2. *(a) Render of the optical breadboard which is mounted atop the dewar (Dr Nikola Prtljaga). (b) A simplified schematic showing the two excitation paths and two collection paths, each with a motorized mirror. Except where indicated, the beam splitters are non-polarizing. ND = neutral density filter; LinP = linear polarizer; HWP = half-wave plate. PBS = polarizing beam splitter.*

off over a period of around 2 weeks, and needs topped up before the system warms to room temperature. Within the tube, a cage system holds the sample mount, optics, and ensures alignment with the optical breadboard that sits atop the dewar. The tube optics consists of the objective, and two relay lenses which effectively remove the tube length and allow a larger scanning range [125].

The top breadboard is shown schematically in figure 4.2(b). The dual excitation and collection paths with motorized mirrors enabled the measurements in chapter 5. A simpler optical setup was used in the work of chapters 6 and 7, and is shown, along with further illustration of the setup, in figure 6.3.

4.3.1.2 Flow cryostat

The flow cryostat cools the sample using a constant flow of liquid helium through one end of a copper plate. The other end of the plate supports and cools the sample. Such cryostats are small, portable and allow relatively easy changing of samples compared to the bath system. The primary disadvantage is that the mechanical stability is generally poorer and compromised by the pumping of helium around the system. A breadboard similar to that shown in figure 4.2 may be used, although it will require the addition of an objective lens, which will now be at room temperature. This means that specialized lenses designed for cryogenic temperatures are not needed.

4.3.2 Measurement techniques

4.3.2.1 Time-correlated single-photon counting

As discussed in chapter 2, a key tool in the investigation of quantum light fields is the second-order correlation measurement. Experimentally this is realized using time-correlated single-photon counting (TCSPC) equipment [126]. The photon module accepts the output pulses from the two detectors. One of the channels is used as the "start" and the other as the "stop". When the start signal is received, a voltage is ramped from a minimum to maximum value over a set period of time. The stop signal halts this process, and the final voltage therefore indicates the time between start and stop signals. The time resolution achievable in this way is at the few ps level, and experimentally the time resolution is more often limited by the timing jitter (response time) of the detectors. The data is binned in time to produce a histogram, and this histogram is proportional to the second-order correlation function of the original field. All of the correlation measurements were obtained in this way. Another mode of operation is first-in first-out (FIFO), where every event is timestamped so that a correlation can be algorithmically generated at the end of the experiment, allowing relatively long correlation over μs to ms ranges.

4.3.2.2 Time-resolved photoluminescence

Time-resolved photoluminescence (TRPL) has many similarities with TCSPC and so often uses the same equipment. In this case however, a pulsed laser is used to excite the system of interest, and at the same time a small amount is clipped off to a photodiode. For every laser pulse, the photodiode outputs an electrical pulse which is used as the "start" signal in the measurement. The "stop" signals arrive from the single-photon

detector when it detects photons from the sample. In this way we can map out the probability of emission as a function of the time delay relative to the excitation pulse. Examples are found in chapters 5 and 7, with chapter 7 also providing further discussion and simulations of the TRPL technique.

4.3.2.3 Spectrometry

A fundamental task in optics is the separation of a light field into its constituent energies via spectrometry. In a spectrometer (spectrograph), a diffraction grating achieves this spatially, and a pixelated charge-coupled device (CCD) image sensor can then display the intensity of the field as a function of wavelength. A common spectrometer may achieve resolutions of 20 µeV or less. When spectral filtering needs to be used in conjunction with single-photon detectors, a monochromator is needed. This can be achieved by focusing the diffraction grating output onto an exit slit rather than the CCD. The exit slit selects a portion of the input spectrum, and this is sent to the detector. Such filtering was used for all the single-photon avalanche diode (SPAD) measurements in this thesis, unless indicated otherwise.

4.3.2.4 Photoluminescence excitation spectroscopy

Usually the PL spectra are taken with the excitation laser tuned to an energy above the band gap of GaAs, or in the InAs wetting layer, so that charge carriers may relax and excite all states in the QD ensemble. If the excitation laser energy is continuously scanned, from just below the wetting layer and down to the *s*-shell emission energy, the emission intensity will be weak except at some specific excitation resonances. These correspond to the the energy of higher orbital shells in the QDs, or longitudinal optical (LO) phonon resonances. This was how the *p*-shell resonance of chapter 5 was located.

4.3.2.5 Fabry–Pérot Interferometry

Fabry–Pérot interferometry is often used when the resolution afforded by a spectrometer is not high enough. A Fabry–Pérot cavity has a narrow transmission linewidth, and by scanning its central transmission frequency (by scanning its length) across the emission line, it is possible to map out the lineshape. A synchronization signal is used to correlate the transmission detection time to cavity length and thus frequency. A scanning Fabry–Pérot interferometer (FPI) produces a spectrum that repeats every free spectral range (FSR) of the cavity. Therefore it is best at measuring linewidths greater than its transmission linewidth, but much smaller than its FSR. Fabry–Pérot interferometry

was used to measure linewidths of QDs in chapter 5, and underpinned the coherent scattering work in chapter 6.

4.3.2.6 Raster maps

To map out QD ensembles in an unpatterned wafer, the excitation and collection spots must be scanned together across the surface. Usually it is easier to keep these fixed in place and scan the sample underneath by stepping the piezoelectric positioners. For mapping the propagation of light through the etched nanostructures, however, it is not possible to move the structure itself, as one spot must be fixed in place, and the other moved independently. The excitation or collection spot must be scanned across an area of $1000\,\mu m^2$ or more. This is enabled by motorized mirrors in the excitation and collection paths, as shown in figure 4.2(b). The raster scan results in a PL map if the signal is filtered at the PL wavelength. Such maps are found in chapters 5 and 8. Alternatively a laser transmission map can be produced for a device by scanning the collection spot, with the laser spot fixed at a chosen location on the device. Filtering the collection at the laser wavelength then gives a map for this specific wavelength.

4.3.2.7 Polarization control

Polarization control of input and output fields is achieved through linear polarizers, quarter-wave and half-wave plates, and other optics if necessary. This allows us to align to nanostructures – such as the linearly polarized gratings (figure 5.4) and cavities (figure 6.5) – to obtain maximum coupling efficiency. Additionally, when collecting via a non-polarized channel, such as from directly above a QD, recording the emission intensity as function of polarizer angle allows us to obtain the polarization of the PL as function of emission energy. This is useful for identifying specific transitions. For example, as discussed in chapter 3, a charged exciton (trion) state shows unpolarized emission, and the neutral exciton (if there is fine-structure splitting (FSS)) shows two orthogonally linear polarized emission lines with an energy splitting. Emission lines resulting from cascades may be identified through their energy-polarization relationships, as in the case of biexciton to exciton to ground decay. The polarization optics used in chapter 5 are shown in figure 4.2(b), while those used in chapters 6 and 7 are shown in figure 6.3. In the latter case they are mainly used to filter out the excitation laser, as discussed in the next section.

4.3.2.8 Resonance fluorescence

Exciting a quantum emitter with a resonant field presents significant experimental challenges. We require that both the laser and the emitter be frequency stable to within the linewidth of the emitter. When we are studying the field produced by the single-photon source (SPS), we need to reject the excitation field, which is complicated by the geometry of planar nanoscale structures. The need to couple light into single modes on-chip means that spatial separation is often not possible. Where possible, light scattered from the surface can be rejected by using polarization filtering. Here, the excitation and collection are cross-polarized, although this has the obvious disadvantage of losing half the collection signal. The optics used are also strongly wavelength dependent so that it works much better for narrow continuous-wave (CW) laser fields, and less well for pulsed excitation. Polarization filtering of the resonant excitation laser was used throughout the measurements of chapters 6 and 7. In that sample, because of the diode structure, it was possible to perform differential measurements – detuning the SPS to quantify the laser background, and then subtracting it.

CHAPTER 5

ON-CHIP INTERFERENCE BETWEEN A SINGLE-PHOTON SOURCE AND A LASER

One of the most fundamental operations in linear-optical quantum computing (LOQC) is the interference that occurs when identical photons enter the two input ports of a beam splitter (BS). This phenomenon, the Hong-Ou-Mandel (HOM) effect, was first demonstrated in 1987, and much effort is under way to make devices that can exploit the effect to create ever larger and more useful entangled states. In this chapter we show the successful on-chip interference of a quantum dot (QD) and a laser, marking a step towards this goal. This work is described in [127].

5.1 Towards scalable quantum dot interference

In our LOQC circuit, we want to have on-chip light sources producing single photons that coalesce through the action of on-chip BSs. This is a challenging goal and therefore it has been approached incrementally. First, the HOM effect was shown with a single QD and off-chip beam splitter using pulsed excitation [128]. Later, time-resolved continuous incoherent [129], resonant (in cavity) [130] and electrical [131] excitation were explored. An obvious step is to use two different quantum dots located in different wafer chips, although with the interference still occurring off-chip, as in [132–134]. The next step is to have both QDs on the same chip [135]. Lastly we would want to perform the interference on the GaAs chip [46]. In fact, this goal has not yet been achieved with two separate QDs.

Reference	Year	Sources	Excitation	On-chip BS
[128]	2002	1 QD	Pulsed	N
[129]	2008	1 QD	CW	N
[136]	2009	1 QD, 1 L	CW	N
[132]	2010	2 QD*	Pulsed	N
[46]	2014	SPDC	CW	Y
This work [127]	2016	1 QD, 1 L	CW	Y
[135]	2016	2 QD**	CW	N

TABLE 5.1. *Development towards scalable on-chip on-demand HOM interference with QDs. *QDs in different chips. **QDs on same chip. BS = beam splitter; CW = continuous-wave; L = laser; SPDC = spontaneous parametric down-conversion.*

In this chapter, however, we make a step towards this by observing HOM interference between a laser and a quantum dot using a monolithically integrated beam splitter. Some of this development is summarized in table 5.1.

5.2 Laser-dot interference

Previously laser-dot interference had been shown off-chip [136–138]. In these experiments the light from the QD is extracted off-chip and interfered with a laser on a macroscopic cube BS. Building upon the first monolithic integrations of QDs with BSs [107, 108], we couple the laser onto the same chip as the QD, and the interference occurs on the chip through the action of a microscopic directional coupler (DC) BS.

5.3 Sample design

The fundamental design of the device is described in this section, and also in [107].

5.3.1 Wafer

Through molecular beam epitaxy (MBE), a GaAs (100) substrate was topped with a 1000 nm thick sacrificial layer of $Al_{0.6}Ga_{0.4}As$, and this in turn supports a final layer of GaAs of thickness 140 nm. This top layer contains In(Ga)As QDs at its centre. The wafer structure is shown schematically in figure 5.1(a).

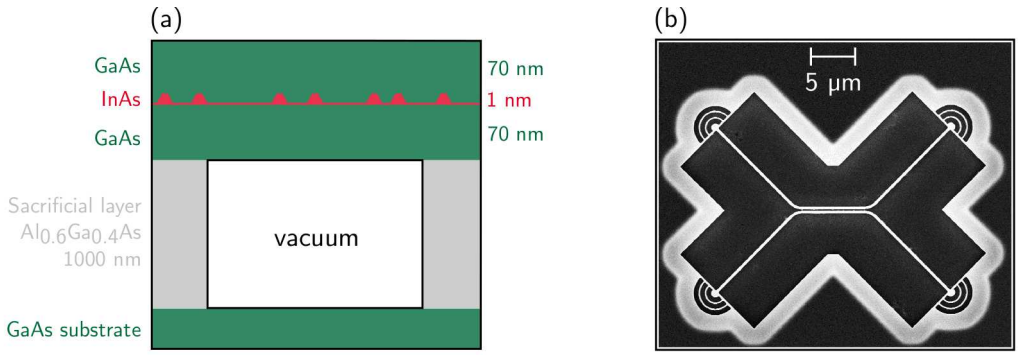

FIGURE 5.1. *(a) A schematic cross-sectional view of the wafer as seen from the side of a waveguide. Once the AlGaAs is removed we are left with a suspended layer of GaAs containing quantum dots. (b) SEM image of a fabricated device.*

5.3.2 Etched structures

The selective etching of the top GaAs layer, along with the removal of the sacrificial layer (as described in chapter 4), forms suspended nanobeam waveguides containing QDs. The waveguides have a width of 280 nm and a depth of 140 nm, and so carry only one transverse electric (TE) polarization mode at the QD wavelengths. To improve the rejection of scattered laser, the input and output arms of the coupler were lengthened compared to those in [107]. The sample contains devices with 5 µm, 10 µm or 20 µm long input/output arms, so that the distance between input and output gratings was tens of microns. Devices have DC coupling lengths L of 6 µm, 7 µm or 8 µm, and coupling separations s of between 50 nm and 140 nm. Simulations by Dr Nikola Prtljaga, figure 5.2, show the required coupling region parameters for 50 : 50 splitting as a function of wavelength. In addition, a slightly modified grating design is used to approximately double the efficiency of coupling light onto and off of the chip. In total the sample contains 540 individual DC devices; figure 5.1(b) shows a scanning electron microscope (SEM) image of a single device.

For the device investigated in detail below, the input/output waveguides are 10 µm long, the coupling region has length L of 7 µm and separation s of 70 nm.

5.4 Quantum dot selection

The high density of QDs in the wafer means that each device contains many dots. Even the reduction in number brought about by the etched waveguides leaves many within

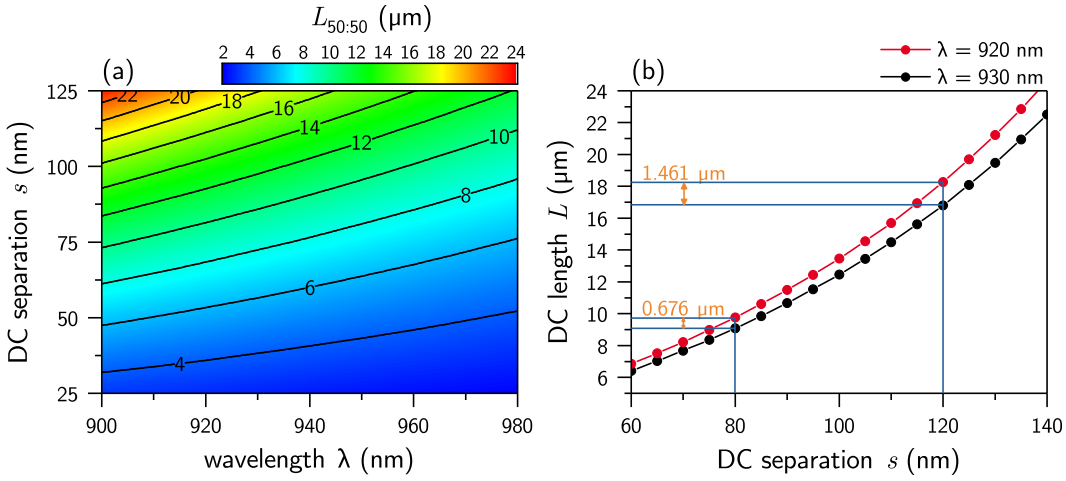

FIGURE 5.2. *(a) Simulations of the coupling length required for 50:50 splitting as a function of wavelength and the separation between the waveguides in the coupling region. The waveguide width is* 280 nm *and the depth* 140 nm*. Some specific lengths are labelled. (b) A different view of the same simulation data, focusing on two wavelengths and the variation between them. As the separation gets larger, the difference in length required for 50:50 splitting also increases.*

the $\sim 1\,\mu$m diameter excitation laser spot. A suitable QD is one that is spectrally isolated from others in its spatial region, and so is usually to be found on the edge of the normal distribution of energies resulting from the Stranski–Krastanov (SK) growth method. We also want the QD to be relatively bright to make correlation measurements less time-consuming, and of course this is important for potential quantum information processing (QIP) applications. Other considerations might be how the dot energy relates to available excitation lasers and detector efficiencies. In this case we also require that its emission wavelength is such that it will experience close to 50:50 splitting by the DC device that it is coupled to.

To find suitable QDs in a device, the wetting layer excitation laser spot could be stepped along an input/output arm. However it was more efficient to perform a photoluminescence excitation spectroscopy (PLE) scan (section 4.3.2.4) by exciting a grating with a tunable continuous-wave (CW) titanium-sapphire (Ti:S) laser, since this excites many QDs along the waveguides. In either case the emission spectra from the two corresponding output arms were simultaneously observed using two spectrometers (figure 5.4(b)). These were calibrated so as to provide a good indication of the splitting at the DC level.

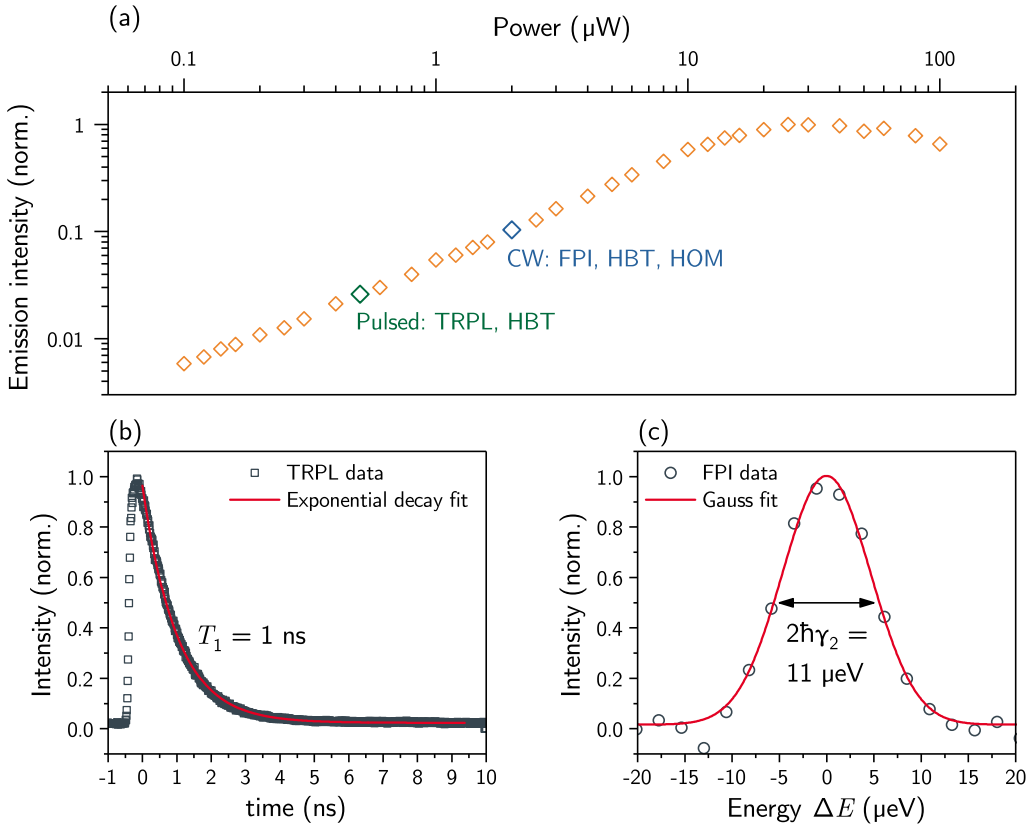

FIGURE 5.3. *(a) Power dependence of the emission intensity of the QD under CW wetting layer excitation. The powers used for subsequent measurements are indicated. (b) Time-resolved photoluminescence measurement. The QD shows a mono-exponential decay with lifetime 1 ns. (c) Fabry–Pérot interferometry reveals that the QD emission has a Gaussian lineshape with FWHM 11 μeV.*

5.5 Power dependence, lifetime and linewidth

The power dependence, lifetime and linewidth of a single QD in an arm of one device are shown in 5.3. The QD is excited from directly above, and the emission intensity saturates at a CW wetting layer excitation power of $\sim 20\,\mu$W. The time constant of the photoluminescence (PL) is 1 ns, from which we can infer that the radiative lifetime of the excited state is also 1 ns – typical for this type of QD. The linewidth, as determined by Fabry–Pérot interferometry, is 11 μeV. No fine-structure splitting (FSS) splitting is evident, and this, along with the linear power dependence, indicates a trion state.

The fact that the lineshape is Gaussian rather than Lorentzian tells us that the primary cause of broadening is not pure dephasing and probably it is due to charge fluctuations

in the quantum dot environment [139]. This occurs on timescales longer than the excited state lifetime, and is not uncommon in etched structures, where the surfaces may act as charge traps [140, 141].

5.6 Waveguiding

Spectra collected from above the QD, from the grating coupler closest to the QD, and from the two output ports are shown in (figure 5.4(b)). We see that the spectrum is reproduced in all locations, with a relative variation in intensity depending on the wavelength, as expected for the DC. The fields projected from the gratings are linearly polarized orthogonal to their respective waveguide's orientation i.e. they preserve the waveguide polarization. The two output fields are cross-polarized, and so enable a polarizing beam splitter to efficiently separate the fields on the top breadboard (figure 4.2(b)).

For the same device, figure 5.5(a) shows the laser transmission from port a to port c, relative to the total transmission $c + d$, as a function of laser wavelength. At the QD wavelength, the splitting is $R : T = 55 : 45$, where R is the reflectance and T the transmittance. In figure 5.5(b), a raster scan of the collection spot, while filtering at the QD wavelength, yields a PL map of the device. The two output ports are illuminated almost equally by the QD, which can also be seen at its position in the waveguide on the logarithmic colour scale.

5.7 HBTs: First-order correlations

To assess the single-photon purity of the selected QD we perform a Hanbury Brown & Twiss (HBT) measurement using the on-chip BS. Changes in the excitation parameters can modify the $g^{(2)}_{\mathrm{HBT}}(\tau)$ in a number of ways. The $g^{(2)}_{\mathrm{HBT}}(0)$ value or the antibunching time constant may change. In addition, there may be bunching with a power dependent amplitude and time constant. In order to correctly analyse the data we will collect in the HOM experiment, we excite the dot under the same conditions in both cases. These conditions are

- Excitation temporal profile: Continous wave.
- Excitation energy: Wetting layer (840 nm).
- Excitation power: 2 µW (well below saturation).

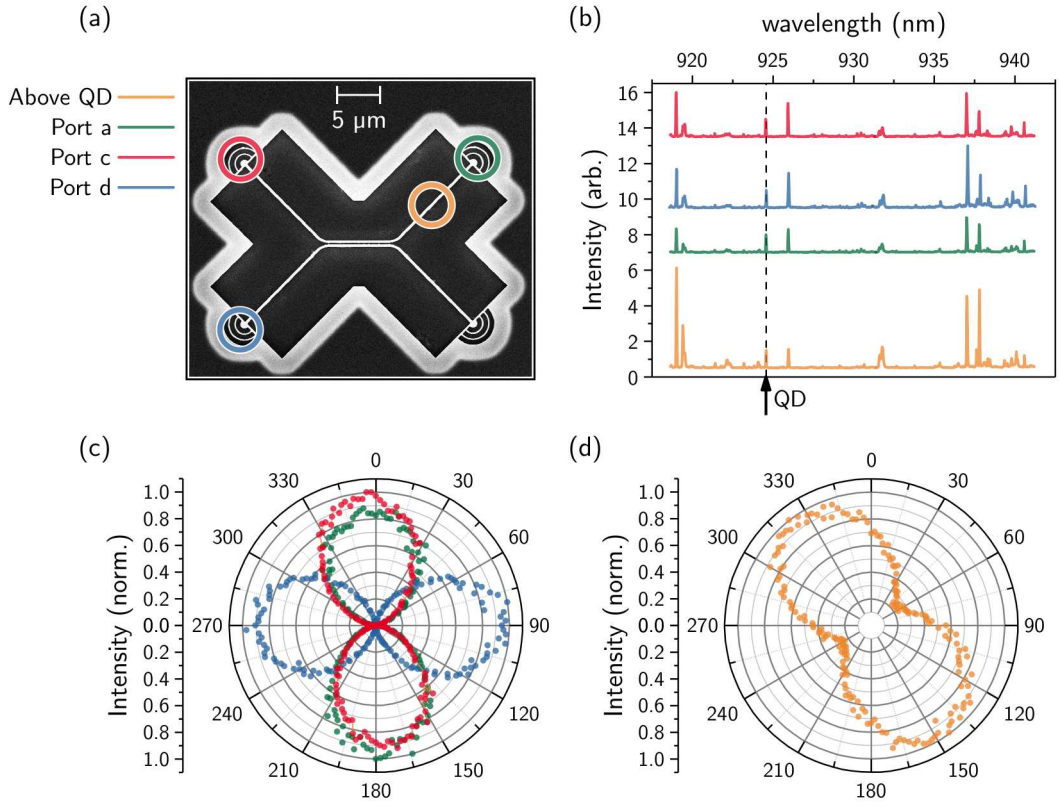

FIGURE 5.4. *Spectral and polarization measurements of the device. In all cases the QD is excited from directly above and via the wetting layer. (a) An SEM image of the directional coupler device. The QD position is indicated by an orange circle midway between the coupler region and an outcoupler (port a) denoted by a green circle. (b) Spectra of the QD emision from three ports and when collecting from the waveguide above the QD. The QD wavelength is indicated by an arrow and a dashed line. (c) Polarization of the emission from the output ports. The emission is linearly polarized along an axis perpendicular to the corresponding waveguide's spatial direction. (d) Polarization of the emission collected from the waveguide above the QD. It is somewhat polarized along a random axis.*

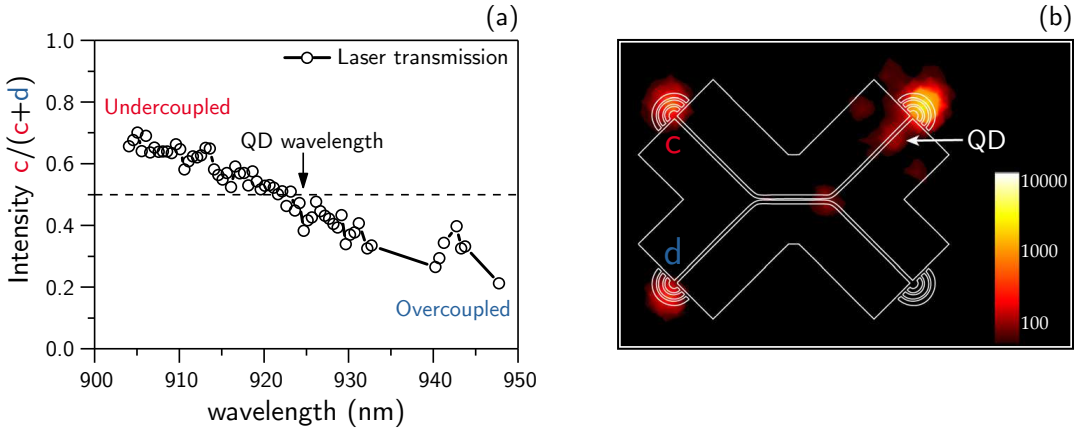

FIGURE 5.5. *(a) Laser transmission through the device. The laser enters through port a, and the relative intensity observed at ports c and d varies with wavelength. At the QD wavelength the splitting ratio is 55:45. (b) Photoluminescence map of the device filtered at the emission wavelength. The QD is excited from directly above and via the wetting layer. An approximately equal amount of the emission exits from ports c and d. Note that the colour scale is logarithmic.*

- Excitation polarization: Linear (aligned for maximum emission).

The wetting layer excitation energy enables the excitation laser to be easily removed from the collection path using the monochromator. The $g^{(2)}_{\mathrm{HBT}}(\tau)$ (without background subtraction) for the QD under these conditions, $g^{(2)}_{\eta}(\tau)$, is shown in figure 5.6.

The data is well accounted for by a fit using

$$g^{(2)}_{\eta}(\tau) = \left(1 - (A+B)e^{-\frac{|\tau|}{\tau_A}} + Be^{-\frac{|\tau|}{\tau_B}}\right) \circledast R_f(\tau), \tag{5.1}$$

where A and B are the amplitudes of the antibunching dip and bunching peak respectively, and τ_A and τ_B are the time constants for these two features. $R_f(\tau)$ is the combined detector response function of the two detectors. Since the individual detectors have approximately Gaussian response functions, the combined response function is also a Gaussian, ad given by

$$R_f(\tau) = Ze^{-4\ln(2)\left(\frac{|\tau|}{F}\right)^2}, \tag{5.2}$$

where Z is the amplitude and F the full width at half maximum (FWHM). In this case $F = 874\,\mathrm{ps}$, and we extract $A = 0.94$, $\tau_A = 2.97\,\mathrm{ns}$, $B = 0.34$ and $\tau_B = 6.5\,\mathrm{ns}$. The relatively

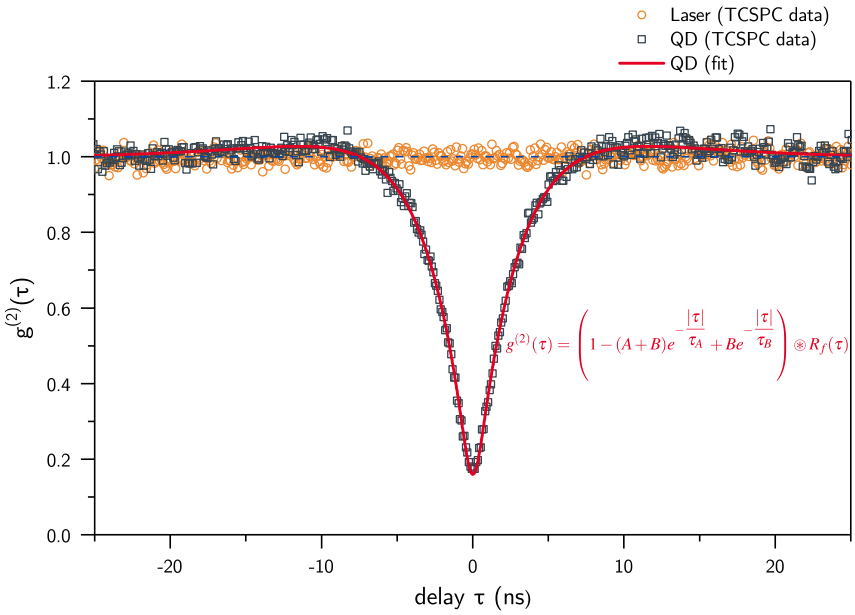

FIGURE 5.6. *Time-correlated single-photon counting (TCSPC) measurements of the QD and laser emission, acquired using the on-chip beam splitter. The Hanbury Brown & Twiss configuration correlates the output fields c and d, and yields a $g^{(2)}(\tau)$ that reveals the statistics of the input fields—the QD mode a is strongly antibunched with a deconvolved $g^{(2)}(0)$ of 0.94; the laser field b is unity for all τ.*

small amount of bunching and its long time-constant mean that the parameters B and τ_B are quite dependent on each other, and so these cannot be pinned down with great accuracy. We also need to characterize the resonant laser, and this is also shown in figure 5.6. Ideally, as discussed in section 2.1.5.1, we should have the laser's second-order correlation functio $g_\alpha^{(2)}(\tau) = 1$ for all τ. This is indeed so, at least to within the noise limit and time range of the experimental procedure.

5.8 Bunching and antibunching

As a slight digression, but to highlight some finer points of the $g^{(2)}(\tau)$ measurements, we will analyse the results of the HBT in more detail. The antibunching time constant τ_A was found to be several times that of the lifetime as measured in the time-resolved photoluminescence (TRPL) measurement of figure 5.3(b). This implies the antibunching is not purely radiative, and that some other process must extend the duration between emission events. Additionally, this, or another process causes bunching. Figure 5.7(a)

shows the HBT under pulsed wetting layer excitation (500 nW), with pulses arriving every 12.5 ns, and figure 5.7(b) shows a simple model to explain the observations. Firstly, the individual peak widths are as expected from the independently measured radiative lifetime of 1 ns convolved with the detector response. However, the peaks nearest $\tau = 0$ show signs of suppression, even at 12.5 ns and 25 ns. This can be modelled by an additional non-radiative antibunching of time constant 14 ns, which implies that most of the antibunching amplitude arises from this process. These observations are in agreement with those of [142], who analyzed their system with a random population model [143], where the QD may capture and lose electrons, holes, and correlated electron-hole pairs, at different rates. In addition to the expected radiative antibunching, their model predicts additional non-radiative antibunching for non-resonant excitation, as here, and an additional bunching component in the case of quasi-resonant or resonant excitation. Note also that in the experimental data, the baseline level around the central peak close to $\tau = 0$ is smaller than the baseline between the other peaks. This effect is explained in [144], and there found to be inversely proportional to T_{rep}/T_1, where T_{rep} is the time between pulses.

Moving to a quasi-resonant CW p-shell excitation, figure 5.8, we indeed see pronounced bunching. In [145] and [146], similar curves were obtained and explained by random population models. The inset to the figure shows that the additional non-radiative antibunching seen under wetting layer excitation is not present.

5.9 Laser-dot Hong-Ou-Mandel

As noted in section 2.1.7, the visibility of Hong-Ou-Mandel interference is usually defined in terms of two measurements, $g^{(2)}_{\text{HOM}}(\tau)_{\parallel}$ and $g^{(2)}_{\text{HOM}}(\tau)_{\perp}$. In the former case the two fields are combined at the beam splitter in such a way as to produce the maximum possible interference; in the latter case the two fields are purposefully made completely distinguishable so that no interference occurs. Then comparison of the two eliminates irrelevant artefacts or confounding variables and gives us a measure of the interference visibility $V(\tau)$.

Since distinguishability can arise through a difference in a single observable, there are a number of ways to produce the control measurement $g^{(2)}_{\text{HOM}}(\tau)_{\perp}$. The easiest way to make the two input fields completely distinguishable is through cross polarization. However it is not possible to do this with on-chip single-mode BSs, and so here we detune the laser in energy to prohibit interference. So to be clear we will refer to $g^{(2)}_{\text{HOM}}(\tau)_{\parallel}$ as $g^{(2)}_{\text{HOM}}(\tau)_{\text{ON}}$, meaning the laser is on-resonance with the QD, and $g^{(2)}_{\text{HOM}}(\tau)_{\perp}$

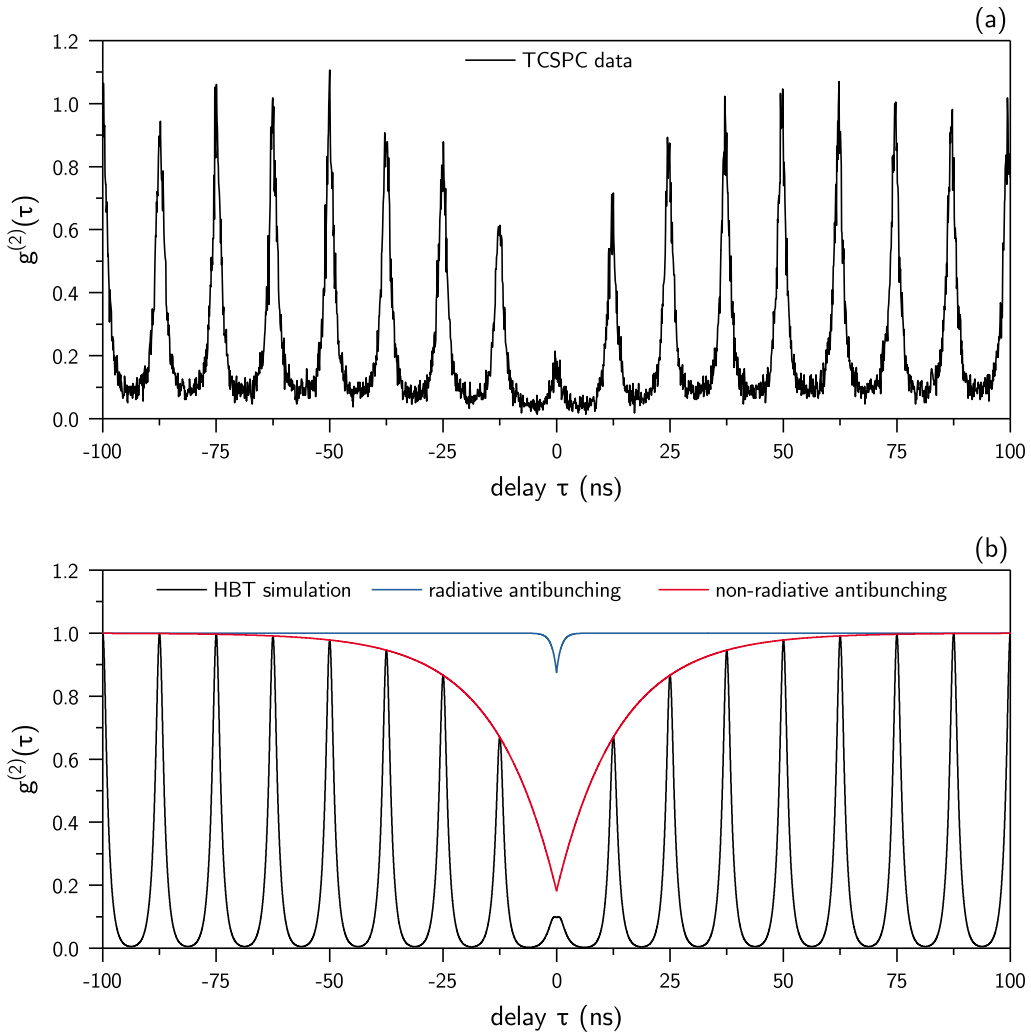

FIGURE 5.7. *(a) TCSPC measurement of the QD second-order correlation under pulsed wetting layer excitation. (b) A simple model of how such a $g^{(2)}(\tau)$ arises. Notably, although the individual peak widths are determined by the measured radiative lifetime, the antibunching is mostly determined by another non-radiative process.*

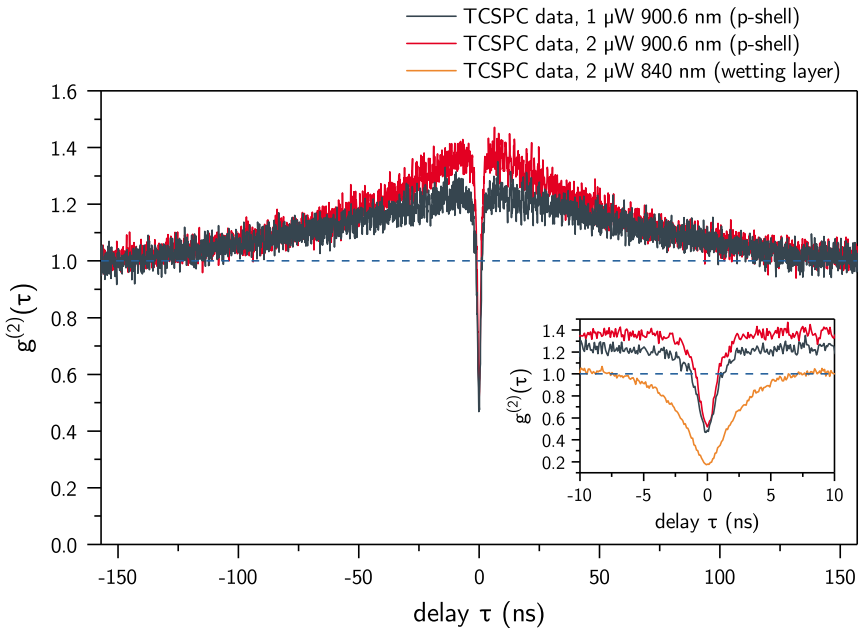

FIGURE 5.8. *TCSPC measurement of the QD second-order correlation under CW p-shell excitation. Inset: A zoom of the central region close to $\tau = 0$, also showing the data from the wetting layer excitation measurement. The bunching is more pronounced in the p-shell case, while both the amplitude and timescale of antibunching are reduced.*

as $g^{(2)}_{\mathrm{HOM}}(\tau)_{\mathrm{OFF}}$, meaning the laser is detuned. In the described measurements we detune by 29 μeV, far outside the linewidth of the QD of 11 μeV, but still within the filtering window of 90 μeV – this is important so that the coincidence count rate is not artificially reduced due to clipping. The tuning/detuning of the laser to and from the QD was automated to occur every 30 min, so that slow experimental drift would not affect comparison of the measurements. The total integration time in each case was typically tens of hours.

The QD was excited from above with wetting layer excitation, and the laser was coupled in through the grating of port *b*. Figure 5.9 shows the "ON" and "OFF" HOM measurements for a QD:laser ratio η/α^2 of unity, i.e. the total intensity of the laser (proportional to α^2) at the outputs was set to equal that of the QD (proportional to η). The calculated visibility is shown in the inset, and all three datasets are accompanied by a theoretical prediction of the respective curves. The theoretical curves arise from the following equation [136]

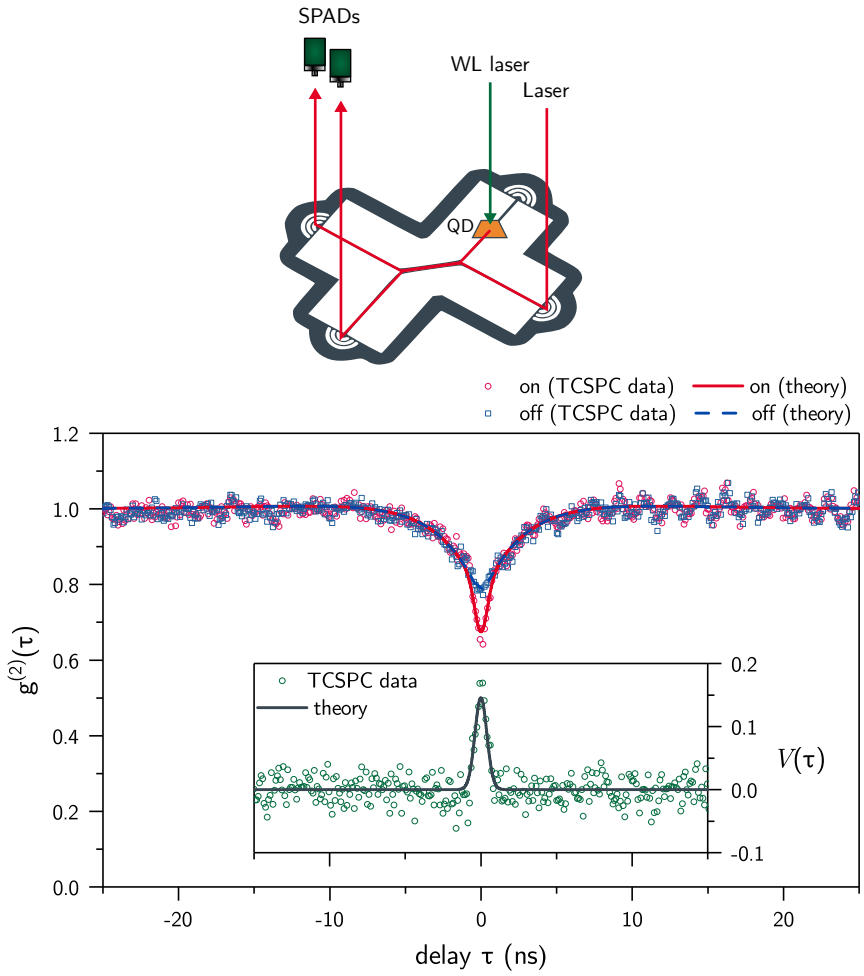

FIGURE 5.9. *Laser-dot HOM with laser/dot intensity ratio of unity. The experimental scheme is sketched above.*

$$g^{(2)}_{\eta\alpha}(\tau) = \left(\frac{g^{(2)}_{\mathrm{SPS}}(\tau)\left(\frac{\eta}{\alpha^2}\right)^2 + \left(\frac{\eta}{\alpha^2}\right)\left(\frac{T^2+R^2}{TR} - 2\Upsilon^2(\tau)\right) + 1}{\left(\frac{\eta}{\alpha^2}\right)^2 + \left(\frac{\eta}{\alpha^2}\right)\left(\frac{T^2+R^2}{TR}\right) + 1} \right) \circledast R_f(\tau). \tag{5.3}$$

where, as before, $R_f(\tau)$ is the detector response function and R and T are the reflectance and transmittance of the BS, and

$$\Upsilon^2(\tau) = \gamma^2 \cos^2(\phi) \cos\left(\frac{\Delta E \cdot \tau}{\hbar}\right) e^{-\frac{|\tau|}{T_2}}. \tag{5.4}$$

Here γ, ϕ and ΔE represent the spatial overlap, relative polarization, and energy difference of the QD and laser modes. Since we are dealing with single-mode waveguides, γ and ϕ are assumed to be unity. T_2 is the QD coherence time*. $\Upsilon(\tau)$ is then the total indistinguishability as a function of delay.

Comparable measurements are shown for additional η/α^2 ratios in figure 5.10. The laser power was adjusted in each case, so the QD excitation conditions did not change. In general the agreement with equation (5.3) is excellent.

5.9.1 Equation analysis

Figure 5.11 shows the variation in maximum HOM visibility as a function of several parameters that enter into equation (5.3). The values used in the experiments are indicated by red dots. It can be seen that most parameters are close to optimized for visibility, and that improvements are mainly to be found through either reducing the detector response time (jitter) F, or reducing the QD linewidth. This amounts to the same thing, which is to make the interference resolvable by the detectors – and for infinitely fast detectors, any finite coherence time will result in "perfect visibility". So although the linewidths of the two sources differ by several orders of magnitude, the time resolution of the experiment is such that we can probe the mutual coherence on a timescale below that even of the coherence time of the QD, and thus we can observe a high visibility at short delays due to the strong temporal filtering [60]. If, for example, we were to compare the total change in coincidence counts between "ON" and "OFF" integrated over a time range comparable to the coherence time of the laser, we would see that the effect of this dip is negligible.

The value obtained through equations (5.3) and (2.12b), even for complete interference, varies depending on the QD:laser ratio η/α^2. For $\eta = \alpha^2$, for example, the formula maximally yields $\frac{2}{3}$. This approaches unity for $\eta \gg \alpha^2$, assuming $g_\eta^{(2)}(0) \sim 0$. However, in doing so, the actual absolute difference between "ON" and "OFF" values decreases, and may become difficult to resolve. This is reflected in the peak and decline of the visibility in panel 5.11(a) for increasing QD:laser ratio. Overall, the degree of interference is proportional to higher values obtained by equation (2.12b), assuming a fixed η/α^2, but is

*A difficulty arises in calculating the coherence time, since the result is different for Lorentz and Gaussian lineshapes, and here we have a Gaussian or Voigt lineshape resulting from the wandering of a Lorentzian. In the CW HOM experiment, assuming a Gaussian lineshape overestimates the visibility, and wandering outside of the laser linewidth will reduce the visibility. Here we have converted the total linewidth to coherence time using the Lorentz formula, and this gives good agreement with the experimental data. This in turn implies that the Lorentz component contains most of the width, and so is greater than the Gaussian wandering width.

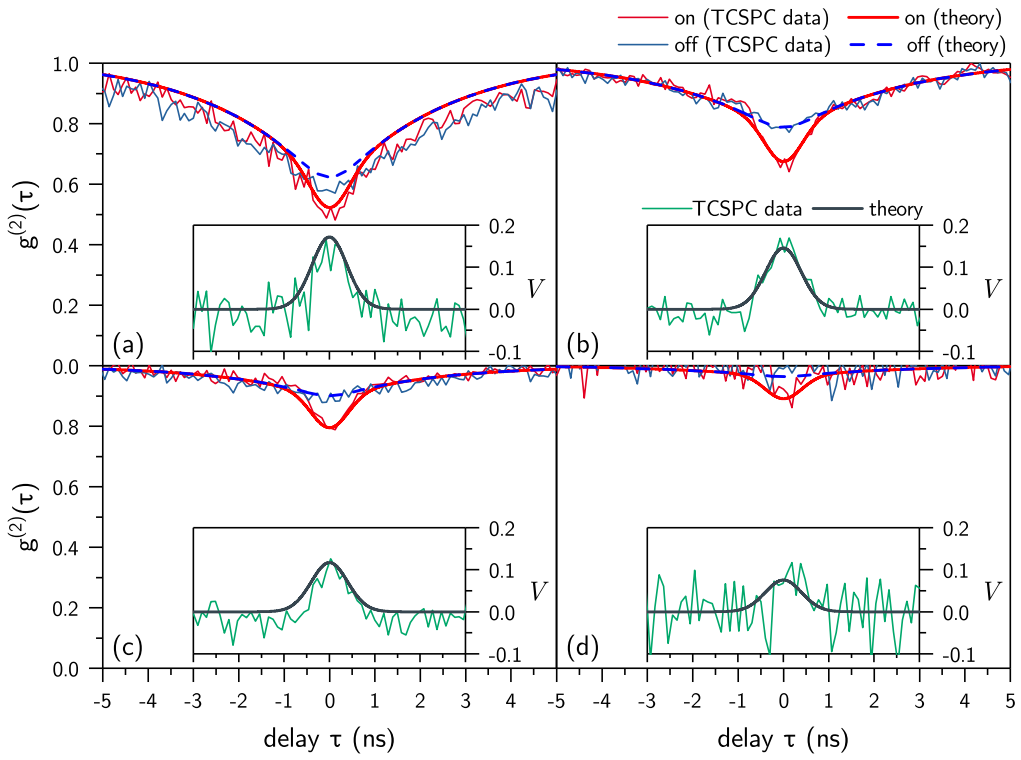

FIGURE 5.10. *Laser-dot HOM with various laser/dot intensity ratios. (a)* $\eta/\alpha^2 = 2$. *(b)* $\eta/\alpha^2 = 1$. *(c)* $\eta/\alpha^2 = 0.5$. *(d)* $\eta/\alpha^2 = 0.25$. *Figure (b) is that shown in figure 5.9. In the case of (a), the deviation of the "ON" and "OFF" data from the theory may be due to an average* $\eta/\alpha^2 > 2$, *because of experimental drift. The insets show the visibility of interference according to application of equation* (2.12b) *to both the data and the simulated* $g^{(2)}_{HOM}(\tau)$ *curves.*

not absolutely so. This is related to the fact that, according to equation (5.3), interference of the laser with the QD leaves the laser and QD coincidence count rates unaffected. The "1"s in the numerator and denominator arise from the laser $g^{(2)}_{\mathrm{HBT}}(\tau)$ of unity for all τ.

Figure 5.11(i) shows that at the detuning of 29 μeV, some interference still occurs, and so the visibility could be improved slightly by making the "OFF" measurement more distinguishable. In figure 5.12 it is shown that with reduced detector timing jitter, it would be possible to observe evidence of quantum beating in the $g^{(2)}(\tau)$ curves at this detuning. However these features get washed out with slower detectors, and with this experimental system they were not visible at all.

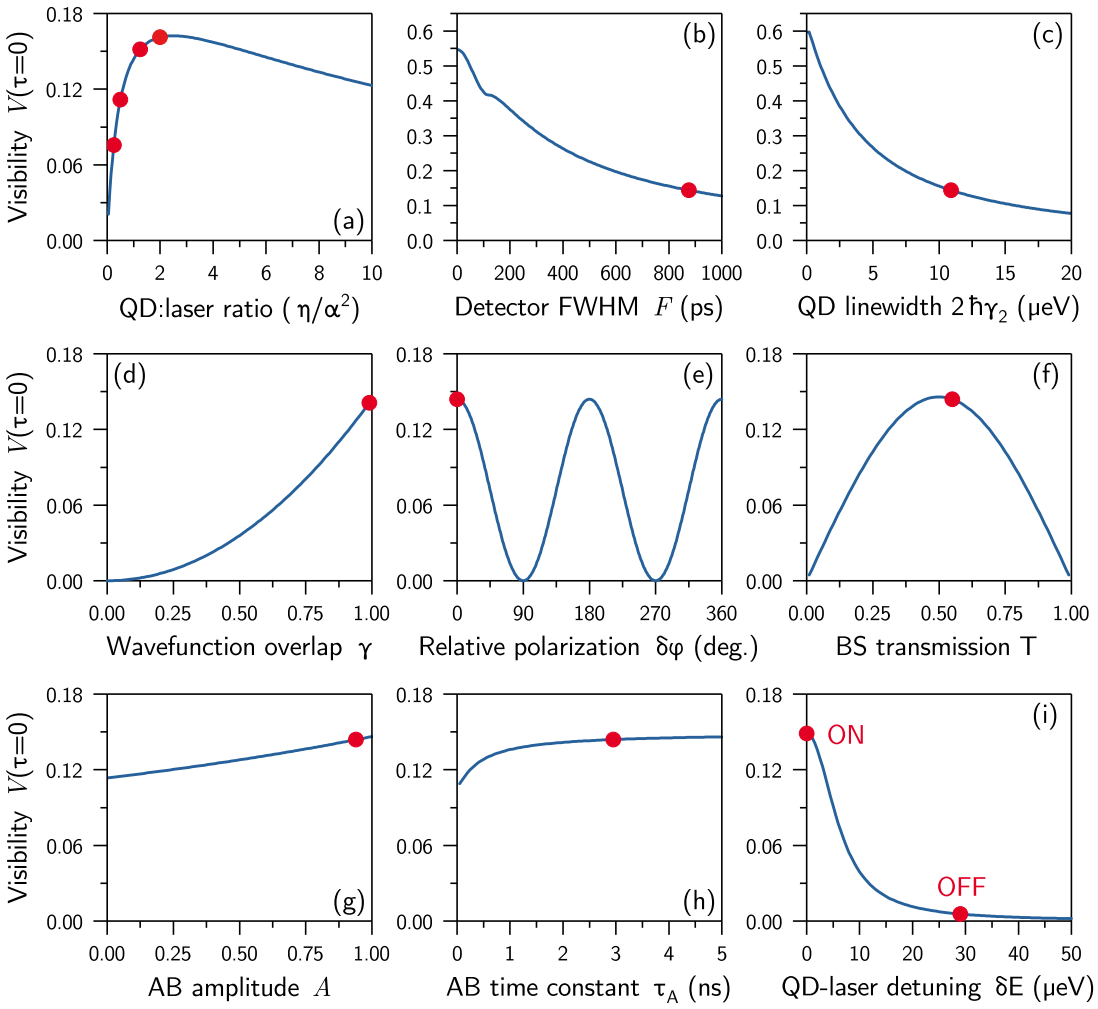

FIGURE 5.11. *Laser-dot interference parameter dependence, according to equation* (5.3). *Unless the independent variable, the value(s) of a particular parameter (both in these simulations and in the experiment) is indicated by the red dots. In the case of (i), $\gamma = 0$ for the "OFF", and the two red dots show the δE values used for "ON" and "OFF". It is clear that the main gains are to be found through reducing either the QD linewidth or the detector response time. AB = antibunching; BS = beam splitter.*

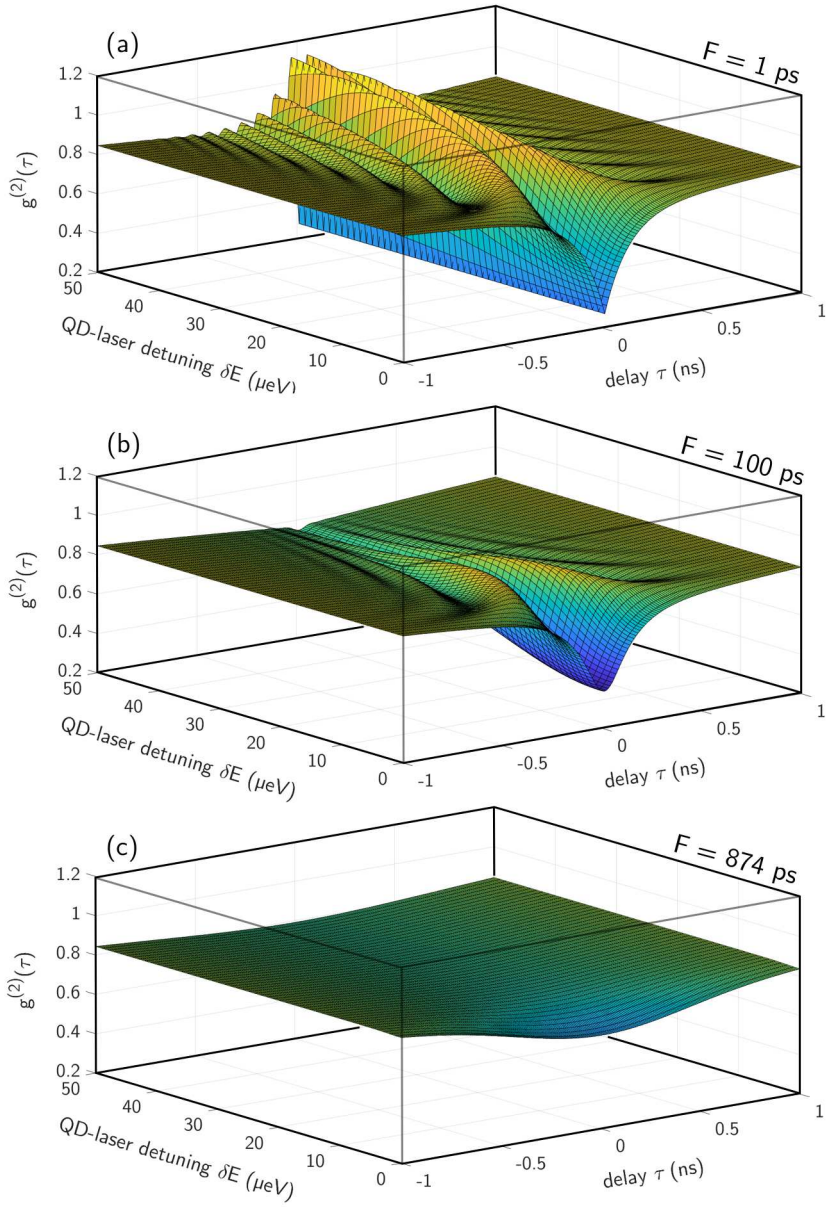

FIGURE 5.12. *Effect of combined detector response F on HOM visibility and beating. (a) With time resolution (1 ps) far below the QD coherence time, visibility of interference is high close to zero delay, and beating is readily observed for non-zero δE. (b) As the detector response gets larger (100 ps), visibility reduces and beats are washed out. (c) For the experimental time resolution (874 ps), visibility is limited and beats are not observable.*

5.10 Other devices, quantum dots, and observations

The measurement procedure described above was also performed on another QD in a different directional coupler device. In that case the visibility, again from equation (2.12b), was $\sim 7\,\%$ (not shown). This was as expected from the theory, given the beam splitter ratio of 60 : 40 and, more importantly, the larger QD linewidth of 17 µeV.

Additionally, an experiment was carried out whereby the laser was input through port d, so that it was combined with this other QD in mode a*. A measurement procedure analogous to the HOM was then performed on the output from port a, using an off-chip BS to enable the time-correlated single-photon counting (TCSPC). In this case we might expect to see no difference between "ON" and "OFF". However, as figure 5.13(a) shows, this is not the case. An increased degree of bunching, or perhaps it is better to say a reduced degree of antibunching, is observed when the laser transmission is on-resonance with the QD. As both fields enter a single BS from the same mode, the bunching cannot be a consequence of the HOM effect (as in [137]). More probably it is due to the interaction of the laser directly with QD states rather than with its emission. This is supported by the fact that the visibility of this (relative) bunching reduces as the QD excitation laser approaches saturation, even while keeping the η/α^2 ratio constant (inset of figure 5.13(a)). This behaviour implies that the (relative) bunching is not related to stimulated emission (as in [147]). An alternative explanation might be that at higher powers the linewidth of the QD emission (or the degree of spectral wandering) increased, however Fabry–Pérot interferometer (FPI) measurements at these powers (not shown) show that the linewidth changed by at most a couple of µeV from 1 µW to 5 µW, and so this is unlikely to be the cause of the decreased visibility of interference. Therefore this observation is likely related to the charge carrier effects seen in section 5.8. As the wetting layer power approaches saturation, the resonant laser will contribute less to the excitation, and so the resonant bunching will be less prominent.

In figure 5.13(b), which is an experimental configuration analogous to that of [137], we see bunching as expected from the HOM coalescence into an output mode. It is interesting that the two configurations of figures 5.13(a) and (b) give a very similar result for quite different reasons.

*This was initially performed as part of a QD-laser energy alignment procedure.

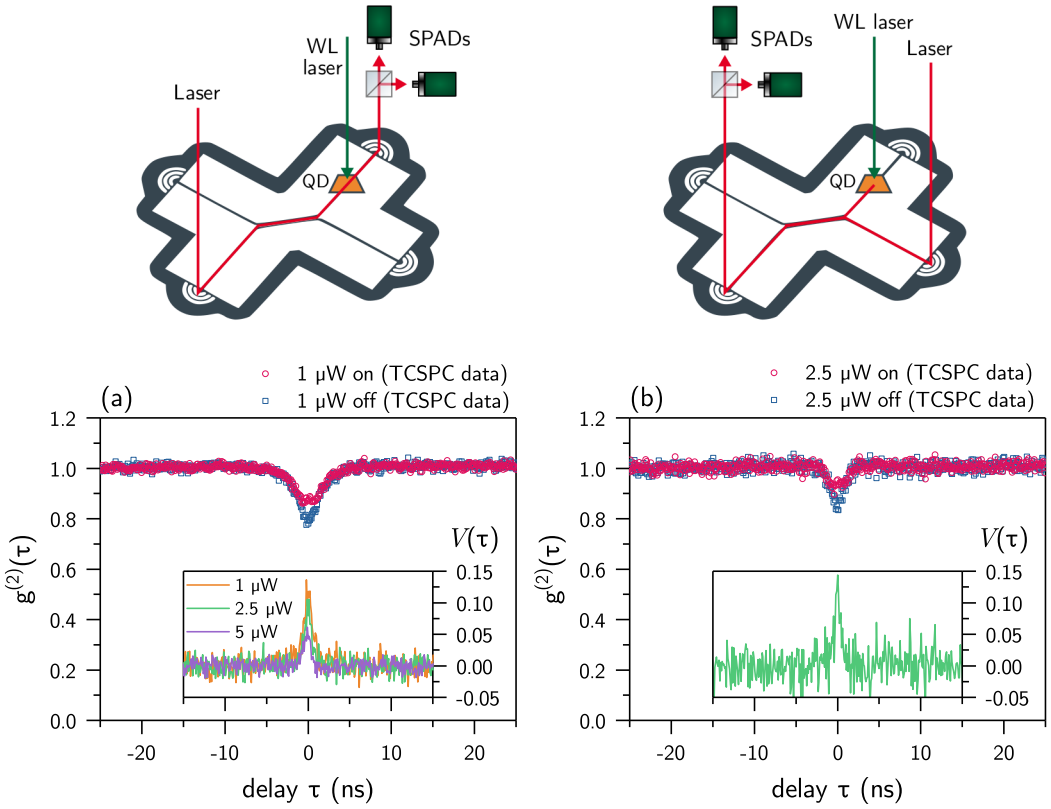

FIGURE 5.13. $g^{(2)}(\tau)$ *data for a different directional coupler device with a different QD. The data was obtained through the same measurement procedure as the previous figures, but with different experimental configurations, which are shown on top. In all cases, the powers refer to that of the wetting layer (WL) laser exciting the QD, and the resonant laser intensity is set to match the QD. (a) The laser passes through the QD before the beam splitter. In this case we see that, unlike the previous measurements, the "ON" measurement is more bunched than the "OFF". HOM bunching is not expected here, and so the observations are probably a consequence of resonant interaction with the QD. (b) Here the statistics of one output field of a HOM experiment are measured. The increased bunching is expected due to the coalescence of photons into the output modes.*

5.11 Conclusion and outlook

In this chapter we have demonstrated the monolithic integration of a QD with a beam splitter. We have seen the effect of uncorrelated electrons and holes on the $g^{(2)}_{\mathrm{HBT}}(\tau)$ resulting from recombination of the trion state, and how this differed for wetting layer and p-shell excitation. We have demonstrated the device's capability as both an on-chip source of single photons and on-chip beam splitter by performing a Hong-Ou-Mandel interference measurement. The visibility of interference was limited by detector response, and could be improved with state-of-the-art detectors. Nevertheless, while this is true for laser-QD interference, the important parameters for QD-QD interference are ultimately the $T_2/(2T_1)$ ratio and the long timescale spectral wandering of the single-photon source (SPS). In the next chapter we look at these and how they both may be optimized through the Purcell effect. In future, this will allow us to create ideal QD SPSs that are monolithically interfaceable with on-chip beam splitter devices such as that described here. In turn this would enable scalable on-chip LOQC circuits, suitable for advanced quantum photonic processing networks.

However, as mentioned in chapter 3, the growth method of SK QDs results in variation in QD energies and positions. This complicates matters when we look towards demonstrating QD-QD interference. One alternative route is to use a train of photons from the same QD, but with an on-chip delay instead of macroscopic delays as in current state-of-the-art work [148]. The fabrication of a suitable delay would be greatly facilitated with shorter QD lifetimes – in the next chapter we also show a very short lifetime through the Purcell effect.

CHAPTER 6

On-chip Generation and Guiding of Frequency-tunable Coherent Single-photons

The quantum mechanical treatment of the interaction of light and matter [68, 69] produced some surprising results, namely that the scattered light can be considered partly *coherent* and partly *incoherent*, with each component having a characteristic spectrum. The theory considered the scattering of a monochromatic beam from an atom, and subsequent experiments with lasers and atoms, and more recently, quantum dots (QDs), have confirmed the validity of this treatment and its predictions. In this chapter, we describe and discuss the observation of coherent scattering from a QD in a photonic crystal cavity (PhCC), which is further coupled to photonic crystal (PhC) waveguides, enabling the on-chip guiding of the narrow-linewidth and antibunched coherent scattered field. This work is described in [149].

6.1 Sample design

The sample we will look at consists of QDs embedded in H1 PhCCs [150] that have been etched out of a *p-i-n* wafer. The two near-degenerate cavity modes are each coupled to a PhC waveguide, allowing on-chip guiding of the cavity emission. The sample design, structure and mounting are described in more detail below, and further information can be found in [151, 152].

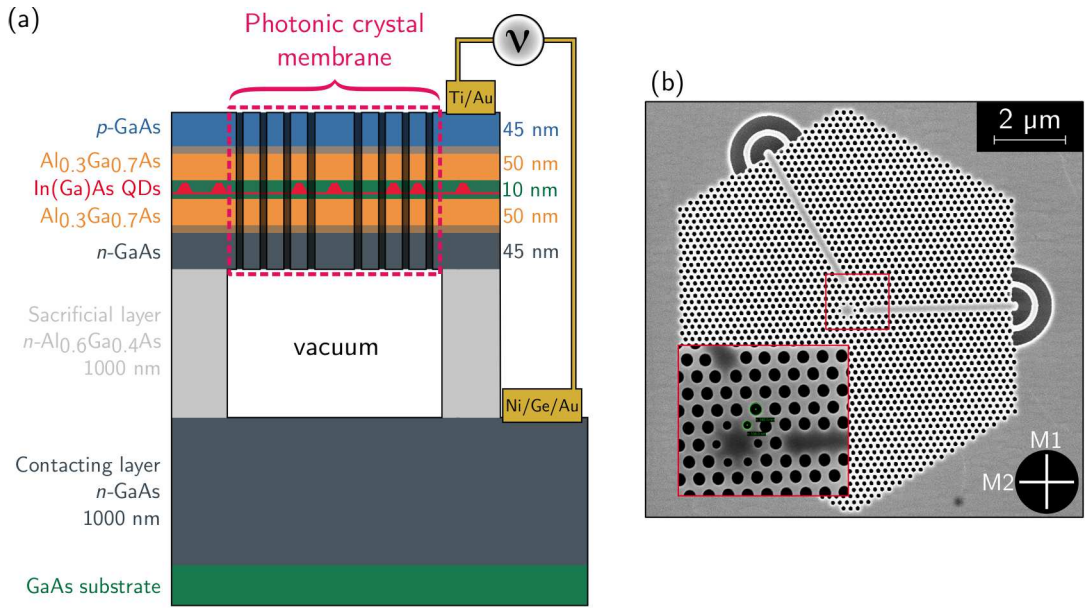

FIGURE 6.1. *(a) Side view cross-sectional schematic showing the wafer layers. Compare with figure 6.2. (b) SEM top view. A H1 photonic crystal cavity is visible in the centre and the polarizations of the primary E-field modes are indicated at the bottom right. M1 couples to the righthand waveguide, and M2 to the top-left. Inset: Zoomed image of the modified H1 cavity.*

6.1.1 Wafer

The wafer construction is shown in figure 6.1(a). Eleven layers are grown on top of the GaAs substrate. The first of these is a 1000 nm thick *n*-doped layer that will enable electrical connection. This is followed by an *n*-AlGaAs layer of the same thickness, a layer which will be selectively etched later so that the supported layers are partially freestanding. These membrane layers consist of *p*-GaAs and *n*-GaAs on the top and bottom respectively, between which an electric field is produced. The central intrinsic GaAs layer is 10 nm thick and contains the In(Ga)As QDs at its centre – these layers are separated from the doped layers by intrinsic AlGaAs barriers, and thin doped AlGaAs transition layers. The total membrane thickness is 200 nm.

6.1.2 Etched structures

Two-dimensional PhCs were created in the wafer by etching holes in a triangular lattice with period $a = 236$ nm, where the hole radii are between $0.31a$ and $0.34a$. In the centre of each hexagonal PhC membrane, one hole is not etched—producing the H1—and

two lines of holes near the waveguide are also unetched—giving the W1 waveguides. The ring of holes closest to the H1 is also modified by shifting their position a further $0.091a$ from the centre, and also reducing their radii by $0.091a$ [150]. This improves the confinement of light within the two transverse electric (TE)–like polarization modes of the cavity. The waveguides are positioned so as to achieve a balance of efficient waveguide coupling to the cavity modes and the reduction in cavity Q that results, and they end with a grating coupler to facilitate the scattering of light into and out of the plane. Thus a single TE-like cavity mode preferentially couples to one waveguide, and the light is guided in the waveguide's single TE-like mode before scattering out of the plane. An example of the final cavity-waveguide structure is shown in figure 6.1(b). The cavity modes M1 couple to the right waveguides, and their primary E-field orientation is as indicated [151]. This polarization is further strengthened for small to medium angles in the far-field [153]. Cavity modes M2 have an orthogonal polarization and are coupled to the top-left waveguides.

6.1.3 *p-i-n* diodes

The *p*-GaAs and *n*-GaAs layers are connected to a voltage source with the aid of contact pads and gold wire. An applied voltage creates a vertical electric field across the QD layer. Through the quantum-confined Stark effect (QCSE), the energy of the QD transitions may be tuned. The usable tuning range is increased through the inclusion of AlGaAs barriers [154]. These increase the range of electric field strength that can be applied before tunnelling out of the central QD layer occurs, and therefore they increase the maximum usable Stark shift. The cavity modes also shift, to a much lesser extent, owing to a small change of the refractive index with field. This in principle allows QDs to be widely tuned into and out of resonance with cavity [155] and waveguide cavity [156] modes. The electric field may also aid the stabilization of the charge environment, removing the necessity of stabilization through a non-resonant laser. The band structure under forward bias is shown in figure 6.2.

6.2 Initial characterization

The sample was loaded into the cryostat as shown in figure 6.3, and cooled to 4 K. Devices were initially characterized using excitation above the GaAs band gap, with which it is possible to see both the cavity modes (at higher power) and individual QDs (at lower power). In this way we can easily find out whether or not there are bright

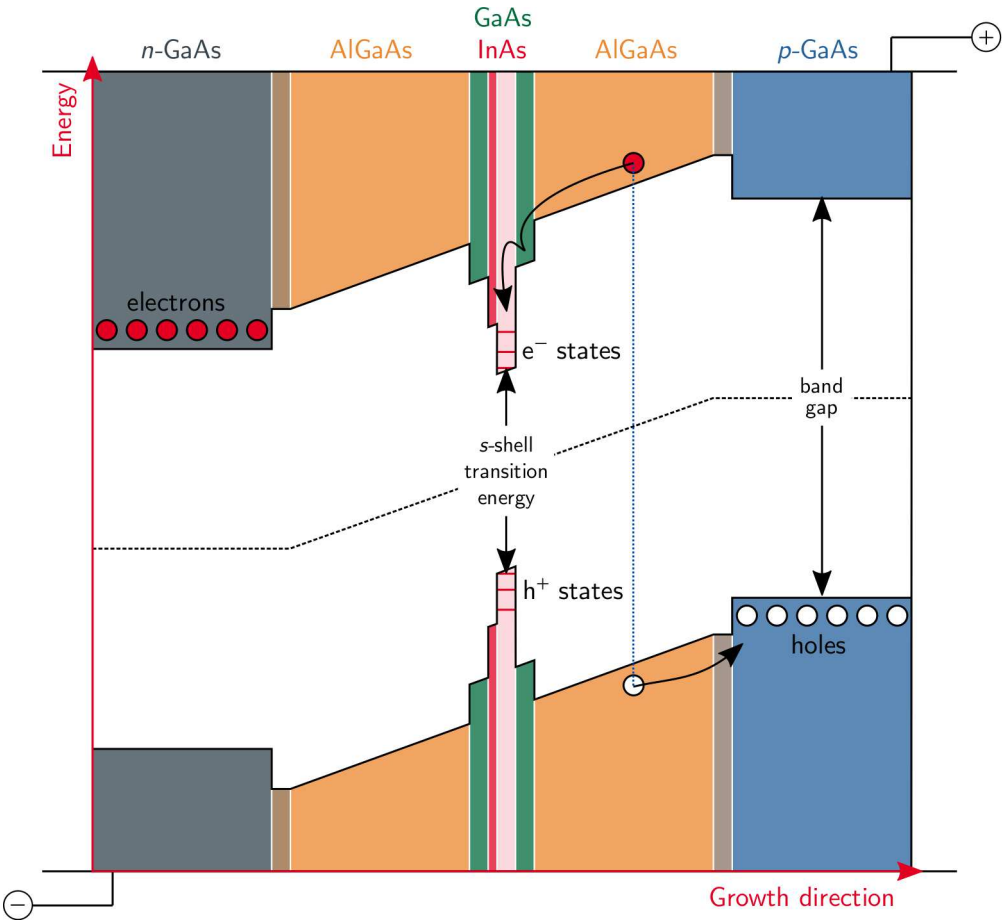

FIGURE 6.2. *Band structure of the photonic crystal membrane under forward bias, with the cross-section taken through a QD. The QD confinement results in atom-like energy levels. The excitation shown here is above the AlGaAs band gap.*

QD lines present within the cavity, both spectrally and spatially, since the few-µm sized laser spot ensures we only excite in the region close to the cavity. With the laser spot weakly exciting the cavity, the bias is scanned across a wide range in order to look for the brightening of a QD line as it moves into the cavity mode – the first obvious sign of a coupled QD-cavity system.

Figure 6.4(a) shows the two cavity modes of one of the devices. Cavity mode M1 has a Q-factor of 540 (Lorentz fit), and is centred at 1.3545 eV. Mode M2 has Q of 765 and is located 2.58 meV to higher energy. Often a small energy splitting is present due to fabrication errors and asymmetries in the structure, but here the large degeneracy was by design, since the sample was originally fabricated with photon routing in mind [152].

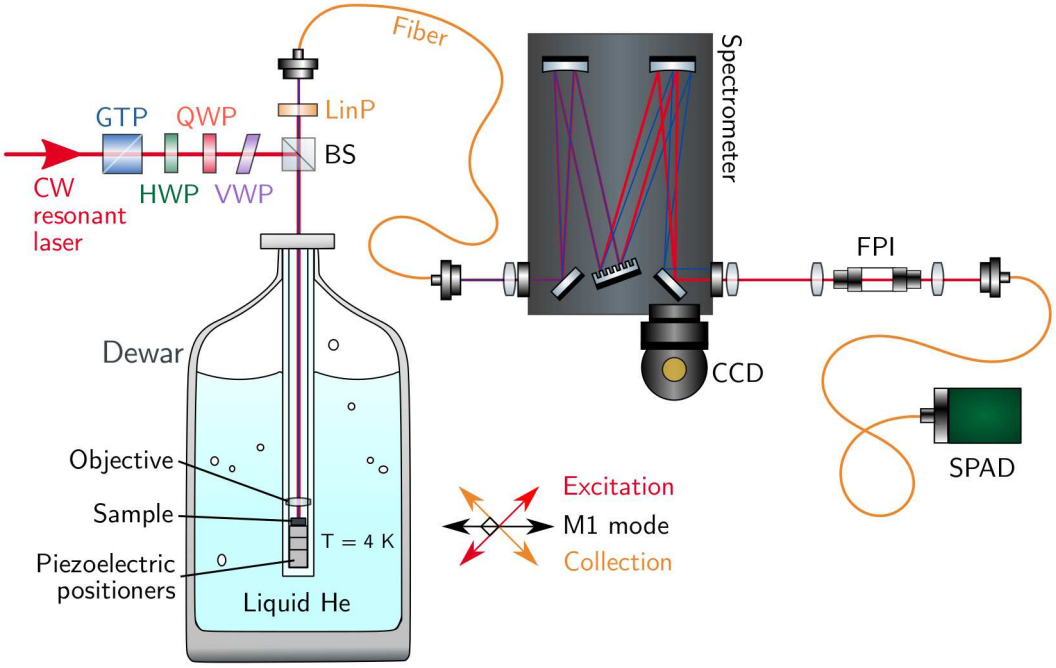

FIGURE 6.3. *Experimental setup for the coherent scattering measurements. The sample is cooled to* 4 K *in a bath cryostat. A continuous-wave (CW) single-mode laser travels through polarization optics and reaches the sample with a linear polarization 45 degrees to that of the cavity modes. A linear polarizer (LinP) in the collection path is aligned orthogonal to the excitation in order to filter out reflected laser from the signal. After spectral filtering, a Fabry–Pérot interferometer (FPI) scans the spectrum and the transmitted photons are detected with a single-photon avalance diode (SPAD). GTP: Glan–Taylor prism; HWP: half-wave plate; QWP: quarter-wave plate; VWP: variable wave plate; BS: beam splitter.*

When applying a voltage of approximately 0.85 V to the sample, a bright line appears in the centre of M1 (figure 6.4(b)). Investigating further, we find that it is one of the bright states of a neutral exciton, as we will show in the next section.

6.3 Exciton fine-structure splitting and eigenstate orientation

The charge species of the studied exciton was determined by measuring the exciton fine-structure splitting (FSS). To make this possible, the QD was Stark-tuned so that its emission energy was between that of the two cavity modes, and excited with weak above-bandgap excitation. Figure 6.5(a) shows the relative peak energy of the QD emission

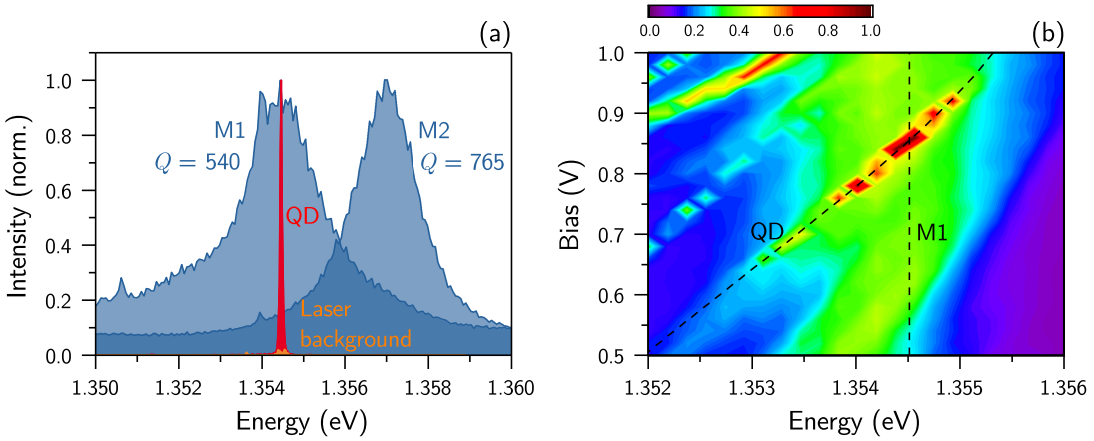

FIGURE 6.4. *(a) Independently normalized cavity mode (blue) and quantum dot spectra (red). The cavity mode spectra are obtained using high power above-bandgap excitation, and are seen at orthogonal linear collection polarizations (see also figure 6.5(b)). Although the quantum dot is excited with resonant laser pulses, there is little laser background (orange). (b) A colour map of the emission intensity under lower power above-bandgap excitation as a function of bias and emission energy. The quantum dot can be seen tuning across M1.*

as a function of the angle (θ) of the collection polarization. A FSS of 19 µeV is clearly observed, indicating that we are looking at the two orthogonally and linearly polarized bright transitions of a neutral exciton.

Figure 6.5(b) shows high power spectra of the two cavity modes measured when the polarizer is co-polarized with the M1 (blue line, $\theta = 168°$) and M2 (orange line, $\theta = 258°$). Importantly, these angles are the same as those that give the maximum and minimum QD peak energy in figure 6.5(a). This means that the two QD eigenstates are co-polarized with the two cavity modes respectively, which is expected since both the QD eigenstates and the fundamental modes of the H1 PhCCs were intended to be aligned parallel/perpendicular to the (110) crystal axes.

This explains why we were required to tune the QD to between the cavity modes in order to see the effect of the FSS – when centred on M1, one transition is greatly enhanced by the cavity mode interaction, and the other will be difficult to observe. This is true also in the following measurements, where we excite with linearly polarized resonant laser at 45° to the cavity mode axes. The fine-structure state aligned to M2 is detuned in energy from M2 by 2.58 meV. Therefore both the excitation efficiency and emission enhancement are much reduced compared to the state aligned with M1. Thus

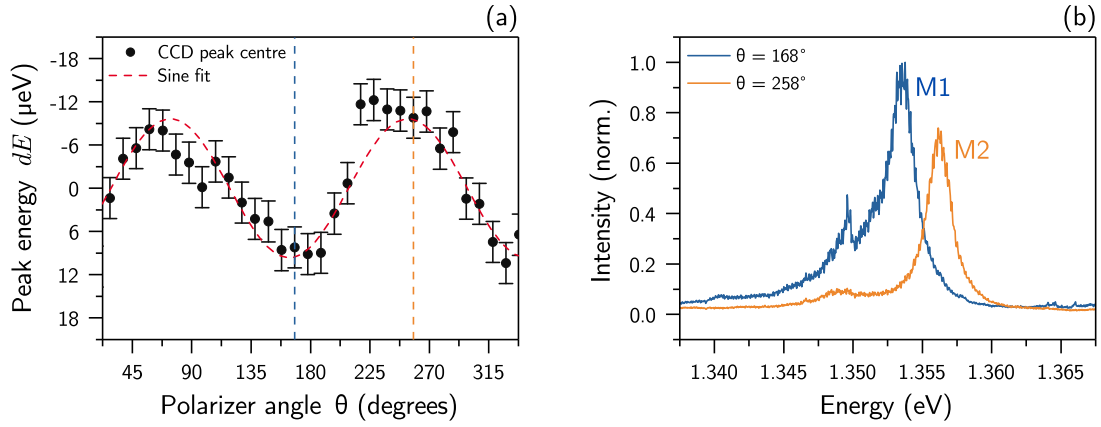

FIGURE 6.5. *(a) Relative peak position of the QD emission versus the angle (θ) of the detected polarization. The peak centres are obtained from Lorentz fits. Red dashed line: sine fit. (b) Photoluminescence spectra of the two cavity modes measured when the collection polarizer is co-polarized with mode M1 (blue line), and mode M2 (orange line). The spectra are normalized to the peak intensity of the M1 mode. The polarization axes of the cavity modes correspond to the polarization axes of the exciton fine-structure states.*

we are dealing with an approximately two-level system (2LS) consisting of the crystal ground state and the bright exciton aligned with M1.

6.4 Experimental procedure for resonant excitation measurements

The QD was excited resonantly with a continuous-wave tunable titanium-sapphire (Ti:S) laser, with linewidth $< 0.2\,\text{neV}$. The excitation was linearly polarized and set at 45° to the also linearly polarized cavity modes. This allows the collection polarizer to be orientated orthogonal to the excitation—enabling optimal suppression—and 45° to the cavity modes—allowing collection of the M1 cavity mode emission.

The emission was collected into a single-mode fiber. From there it was sent to a spectrometer, where, after dispersing the constituent energies with a grating, it could be observed on a charge-coupled device (CCD), or by flipping a mirror, sent to an output slit.

When sent through the output slit, the filtering window was 90 μeV and centred on the QD line. The beam then passes through the scanning-Fabry–Pérot interferometer

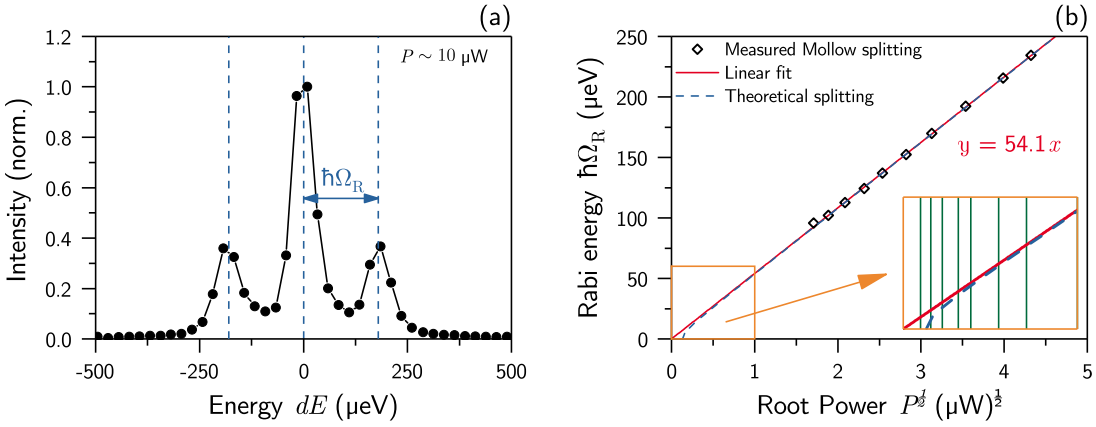

FIGURE 6.6. *(a) A high power ($\sim 10\,\mu$W) background-subtracted spectrum showing the very large Mollow splitting. (b) The measured dependence of the splitting on laser power and the deduced theoretical splitting from equation* (2.35)*. At very low powers the splitting is damped and no triplet occurs. Inset: Zoomed view of $P = 0\,\mu$W to $P = 1\,\mu$W. The powers used in the coherent scattering measurements are indicated by vertical green lines.*

(FPI), with the transmitted signal then being collected into a multi-mode fiber and guided to a single-photon avalanche diode (SPAD), as shown in figure 6.3.

For the FPI measurements, a function generator sweeps the FPI cavity length, with the start of each sweep cycle accompanied by a trigger pulse to a time-correlated single-photon counting (TCSPC) module. The photon-counting module then time-tags the arriving pulses from the SPAD relative to the trigger pulse. By repeating and summing many sweeps, we produce the transmission spectrum as a function of sweep time. The sweep amplitude was set such that several free spectral ranges (FSRs) of the cavity were traversed. Having measured the FSR as 41.3 μeV, we could then convert the sweep times to relative energies (spectral positions) using the multiple peaks in the FPI spectrum. In the measurements described, a single sweep took 10 s, and 300 such sweeps were combined. The resolution of the resulting spectra were $\sim 1\,\mu$eV.

6.5 Mollow triplet and Rabi frequencies

When the resonant driving field is strong, such that $(\Omega_R)^2 \gg \gamma_1\gamma_2$, and the damped Rabi frequency (equation (2.35)) becomes real, a Mollow triplet forms, as shown in Fig. 6.6(a). The splitting at high powers is proportional to the square root of the power and allows us to extrapolate the Rabi frequencies down to the low powers of the resonant Rayleigh

scattering (RRS) regime, as shown in Fig. 6.6(b). Indicated in the inset of the same figure are the excitation powers used in the following coherent scattering measurements. The Mollow splitting is very large, and as far as we are aware, the largest reported for a QD-cavity system. The splitting is 54.1 µeV with a continuous-wave (CW) input power of just 1 µW thanks to a large coupling strength g (calculated in the next chapter, in section 7.4).

6.6 Resonant Rayleigh scattering

As described in section 2.2.2.7, RRS refers to coherent scattering of single laser photons by a 2LS, in this case a single QD exciton [70]. The degree of coherent scattering from the QD, as with any 2LS, is highly sensitive to the $T_2/(2T_1)$ ratio. The emission from a single quantum emitter in the small Rabi frequency limit ($(\Omega_R)^2 \ll \gamma_1\gamma_2$) is dominated by RRS provided $T_2 > T_1$ [70, 157–160]. These coherently scattered photons are antibunched on the timescale of the emitter lifetime but retain the linewidth (and thus coherence) of the laser.

6.6.1 Background subtraction

For every excitation power, the FPI measurement procedure described above was performed twice, first with the QD resonant, and again with the QD detuned by about -1 meV. This allowed us to characterize the amount of background laser. This is important because, while the overall signal-to-background ratio (SBR) is very good, the small amount of reflected laser background is concentrated (by definition) in the same spectral region of the coherently scattered field. Figure 6.7 shows how the spectra obtained with the QD detuned were subtracted from the QD-resonant spectra to obtain the scattered field*.

6.6.2 Fitting the Fabry–Pérot spectra

The resulting background-subtracted Fabry–Pérot spectra consist of a series of peaks separated by the FSR. These have two components: RRS and spontaneous emission (SE).

*This procedure would be invalid if the *reflected* (as opposed to QD-scattered) signal also changed due to the presence or absence of the QD within the cavity. However separate measurements of the same QD-cavity system at comparable powers have shown that the amount of reflected signal does not vary whether the QD is detuned by -0.5 meV, -1 meV or -2 meV. Additionally, when using this background-subtraction procedure for pulsed excitation measurements, the obtained signal undergoes a Rabi oscillation and is also antibunched, implying it is indeed a result of interaction with the QD.

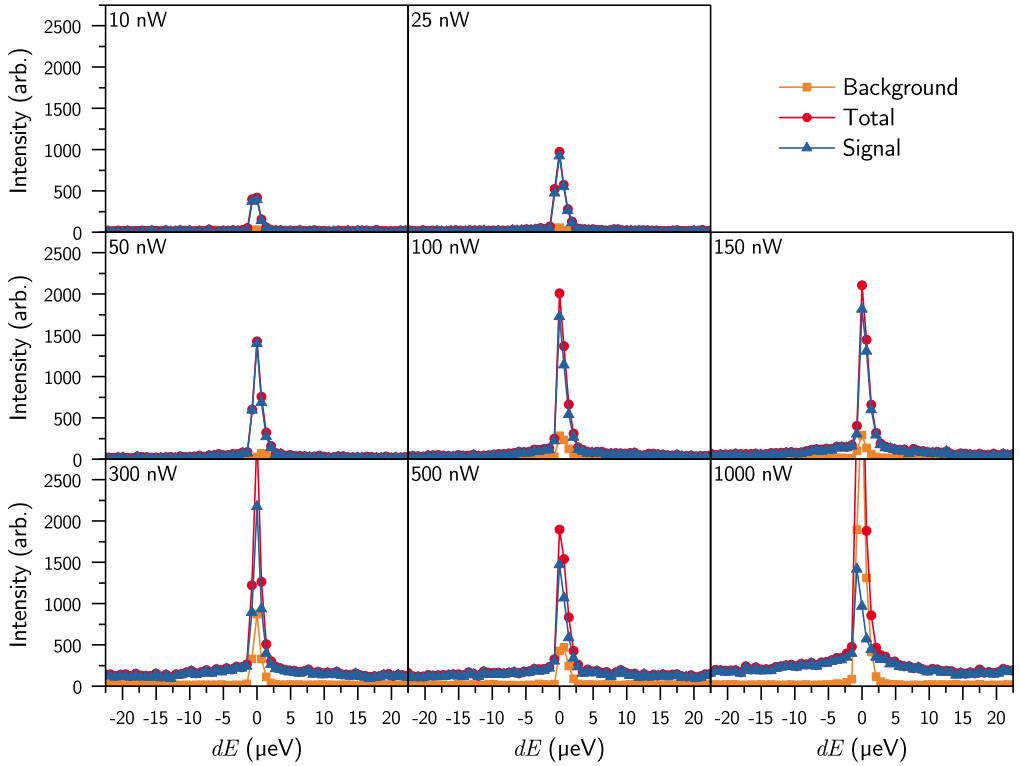

FIGURE 6.7. *Fabry–Pérot spectra of the scattered field as a function of excitation power. Two spectra are taken for each power – a spectrum with the quantum dot (QD) detuned, giving the reflected laser background (Background), and a spectrum with the QD in resonance (Total). Subtraction of the former from the latter gives the scattered field arising from interaction with the QD (Signal). For comparison all spectra are shown on the same linear scale.*

A function consisting of the sum of three Lorentzian (for the SE) and three Gaussian peaks (for the RRS) was fitted to the data. Here the Gaussian was used to approximate the Fabry–Pérot instrument response function (IRF), from which the sub-IRF linewidth coherent scatter cannot be distinguished. At low powers the SE component is spectrally broad with negligible intensity, and the fits are therefore constrained using a linewidth obtained from higher power measurements. At high powers the Mollow triplet begins to form and move – this was not clearly resolvable given the large SE linewidth relative to the FSR. Nevertheless, the fits were able to give a good estimate of the amount of signal between the narrow RRS peaks. The multi-peak fit is essential in this regard to account for contributions from neighbouring FSRs.

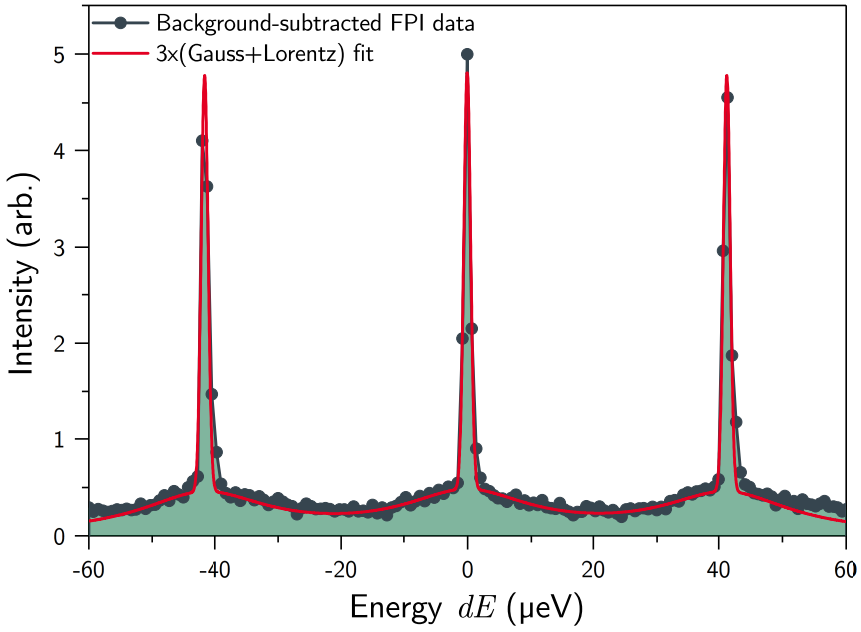

FIGURE 6.8. *An example background-subtracted Fabry–Pérot spectrum, showing the multi-peak fit. The spectrum is repeated every free spectral range.*

6.6.3 Coherent and Incoherent scatter

The Gaussian component of the fits corresponds to the coherent scatter (RRS), and the Lorentz component corresponds to the incoherent scatter (SE). Thus the ratio of the Gaussian area to the sum of the Gaussian and Lorentz areas gives the ratio of coherent to total scatter. This is plotted as a function of power and Rabi frequency in figure 6.9(a).

The 500 nW and 1000 nW SE components were adjusted to account for clipping of the signal as the Mollow side peaks approach the edge of the filtering window. At high driving strengths (figure 6.9(c)), the spectrum consists of a sub-μeV (FPI resolution-limited) component from RRS plus a broad contribution from SE which is not visible at lower driving strengths (figure 6.9(b)). The errors are large at low powers chiefly because of the difficultly of fitting this weak and spectrally broad SE component. The orange line in (a) is a fit of equation (2.39) to the extracted ratios, which is sometimes put directly in terms of T_1 and T_2 as:

$$\frac{I_{\mathrm{RRS}}}{I_{\mathrm{total}}} = \frac{T_2}{2T_1} \times \frac{1}{1 + T_1 T_2 (\Omega_{\mathrm{R}})^2}, \tag{6.1}$$

although this is no longer a dimensionless ratio because Ω_{R} still has units of angular

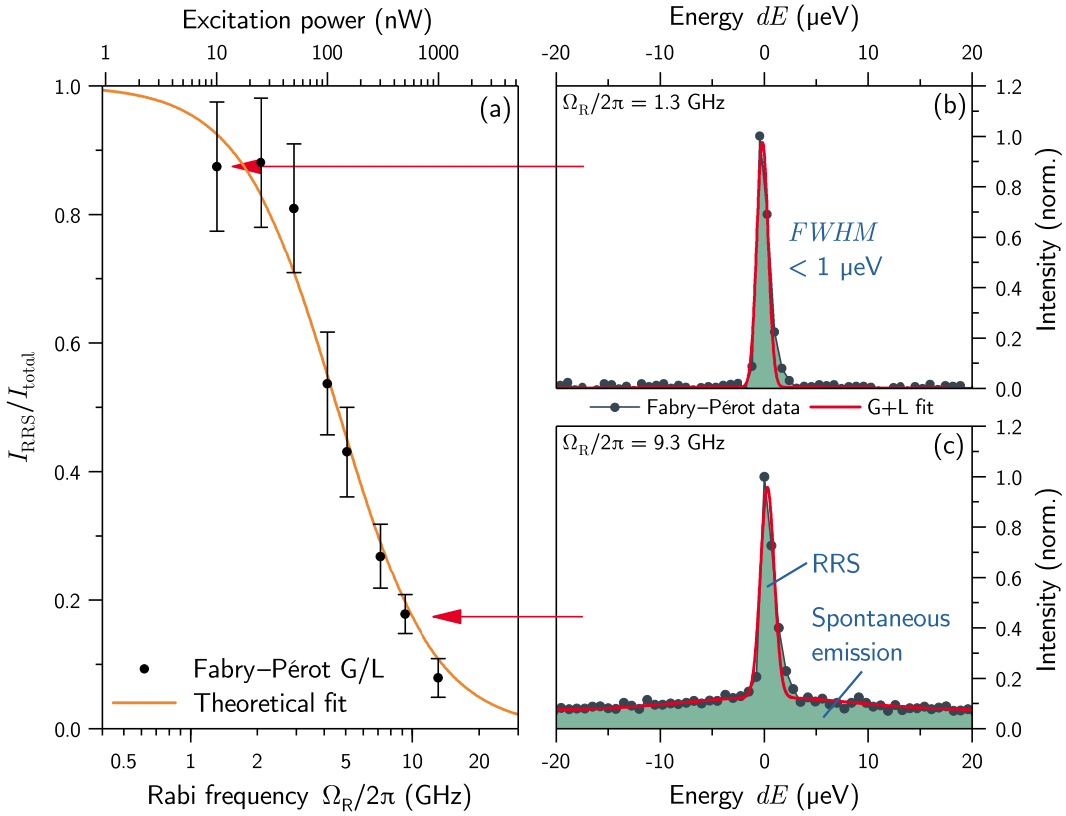

FIGURE 6.9. *(a) Plot of the ratio of the coherently scattered laser photons (I_{RRS}) to the total scatter ($I_{total} = I_{RRS} + I_{SE}$) as a function of Rabi frequency and CW excitation power. Orange line: Fit using equation 6.1. (b) and (c): High resolution spectra of the QD emission under (b) weak and (c) strong CW resonant driving, measured with a Fabry–Pérot interferometer. Red lines: Fits of the scattered field with a function that is the sum of Gaussian (G) and Lorentz (L) peaks.*

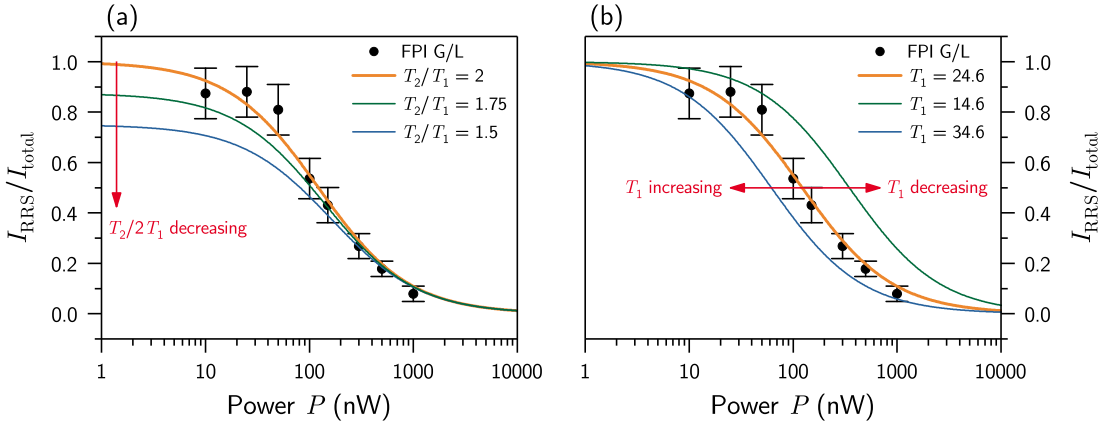

FIGURE 6.10. *Experimental I_{RRS}/I_{total} (black circles) and fits with equation 6.1 (coloured lines). (a) Illustration of the effect of reduced coherence. Here the curves have the same T_1 value, and together they show that a high fraction of coherent scatter at low power implies that the emitter coherence is very close to the lifetime limit. For $T_2/T_1 = 1.5$ (blue curve), for example, it is not possible to reach 80 % I_{RRS}. (b) Illustration of the effect of varying T_1 for lifetime-limited curves ($T_2 = 2T_1$). We see that the point at which coherent scattering gives way to incoherent scattering is strongly dependent on T_1. For both (a) and (b) the orange curve is the fit shown in figure 6.9(a).*

frequency. Nevertheless, it is numerically equivalent* and demonstrates that reducing T_1 through a large F_P value leads to an improved fraction of RRS.

The fit gives $T_1 = (24.6 \pm 1.6)$ ps and $T_2 = (49.2 \pm 5.4)$ ps, indicating that the emitter has very close to lifetime-limited coherence. Figure 6.10 shows that the theoretical curve is very sensitive to the values of both these quantities. The high fractions of RRS ($\sim 87\,\%$) observed at low power are only possible for an emitter operating close to the radiative limit, i.e. $T_2/(2T_1) \sim 1$ (figure 6.10(a)). Therefore the system displays a close to ideal value of $T_2/(2T_1)$. The point at which incoherent scattering begins to dominate is very sensitive to T_1 – with $T_1 = 14.6$ or 34.6 ps this occurs much too late or early respectively (figure 6.10(b)). This is a reflection of the fact that shorter lifetimes have higher saturation powers.

*A consequence of the relationship between lifetime and linewidth, see section 2.2.1.2.

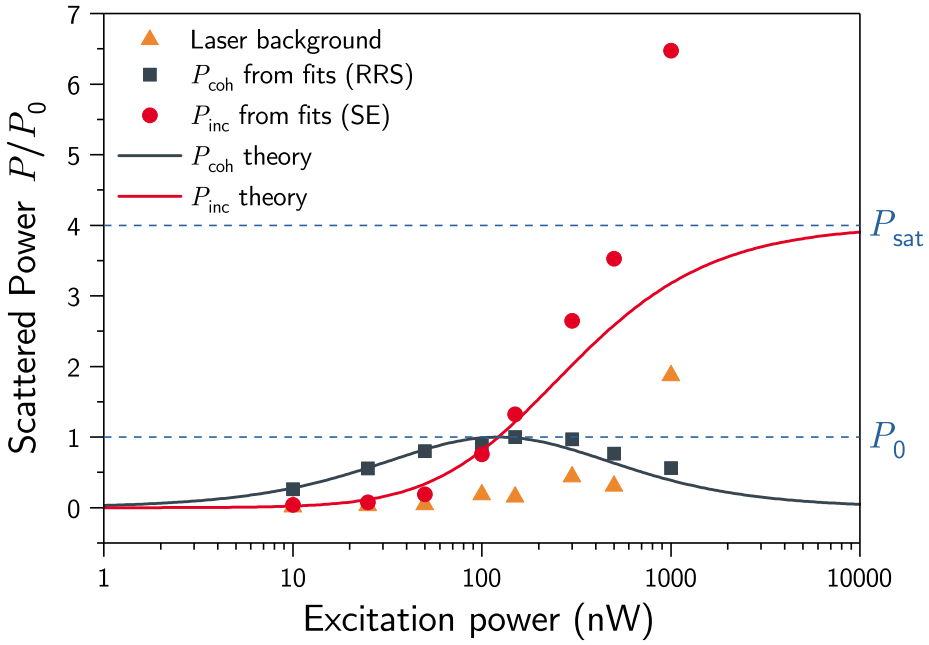

FIGURE 6.11. *The scattered field components as a function of incident field power. The coherent scatter data (P_{coh}) follows the expected trend – increasing up to P_0, and decreasing thereafter. The incoherent component (P_{inc}) appears to continue increasing beyond the expected point of saturation. Also shown is the amount of laser background that was present and subtracted from the spectra before the analysis.*

6.6.4 Further analysis

The equation for the ratio of coherent to total scattered field is derived from the formulae for the coherent and incoherent scatter separately, which are [161, 162]:

$$P_{\text{coh}} = \frac{\gamma_1}{4\gamma_2}\frac{S}{(1+S)^2}\Gamma_1\hbar\omega_a \quad \text{[W]} \quad (6.2a)$$

$$P_{\text{inc}} = \frac{S(\gamma_2+\gamma_2 S-\gamma_1/2)}{2\gamma_2(1+S)^2}\Gamma_1\hbar\omega_a \quad \text{[W]} \quad (6.2b)$$

where

$$S = \frac{(\Omega_{\text{R}})^2/(\gamma_1\gamma_2)}{1+\Delta^2/\gamma_2^2}, \quad (6.3)$$

and Δ is the detuning in $\text{rad}\,\text{s}^{-1}$ of the incident field from the 2LS transition energy ω_a.

These are plotted in figure 6.11 using the γ_1 and γ_2 parameters obtained from the fit in figure 6.9(a), alongside the values obtained from the individual components of the FPI fits. The data is normalized to the saturation parameter P_0, which is the power

Field component	Scattering	Linewidth (μeV)	Coherence time (ns)	Statistics	Max. photon rate (GHz)
Laser	N/A	0.0002	6400	P	$\gg 10$
SE	inelastic	29	0.046	AB	~ 10
RRS	elastic	0.0002	6400	AB	$\ll 10$

TABLE 6.1. *Values and properties of the different field components involved when the CW laser is incident upon the lifetime-limited In(Ga)As QD. The coherence times are inferred from the linewidths. SE = spontaneous emission; RRS = resonant Rayleigh scattering; P = Poissonian; AB = antibunched*

at which the coherent and incoherent components are equal, and this occurs at one quarter of the emitter's saturation power* $P_{\text{sat}} = \frac{1}{2}\Gamma_1\hbar\omega_a$ [W]. For the lower powers, both components follow the theory very closely. Above P_0 however, the incoherent scatter does not saturate as expected. It is not clear why, but one possible explanation is the phonon-assisted excitation and emission of other states at high powers. Also shown in figure 6.11 is the amount of laser background that was subtracted in each case before any analysis was performed (cf. section 6.6.1), which at the lowest powers is negligible (0.5 % for 10 nW).

The values and properties of the different field components are tabulated in table 6.1. The reflected laser can of course have incredibly high photon rates, but the statistics are Poissonian, limiting the use in quantum information processing (QIP) applications. The RRS retains the coherence of the laser, but with antibunched statistics. However it is limited to photon rates much less than that of the SE rate of the 2LS.

6.6.5 Waveguide signal-to-background and brightness

The measurements just described were obtained by collecting the emission from the top of the cavity. However the QD-cavity system is intended as a source of on-chip photons. We are therefore interested in the SBR and brightness in the waveguide. The first of these can be measured from the grating coupler, since this transmits the waveguide spectrum. Because in the waveguide no additional filter may be applied, we must look at the wide spectrum to determine the real SBR that we obtain.

As before, we determine the SBR by comparing the spectra seen when the QD is resonant with, and detuned from, the laser, which is centred on cavity mode M1. This

*Because of the CW coherent excitation, the maximum average population of the excited state is $\frac{1}{2}$.

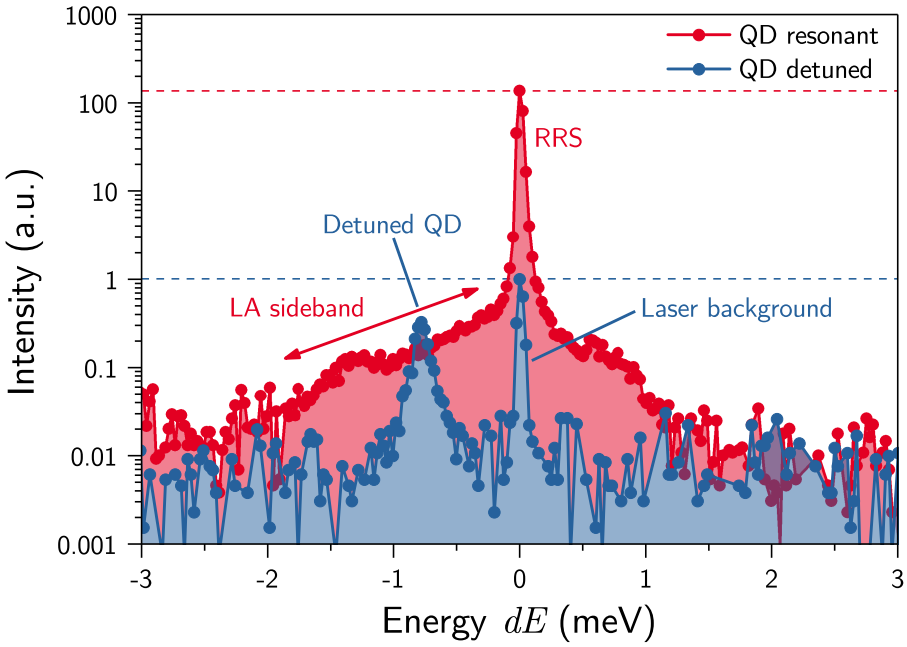

FIGURE 6.12. *Log-linear spectra of the device under weak resonant CW excitation (*25 nW, $\Omega_R/(2\pi) \sim 2$ GHz*) when the QD is either resonant (red data) or detuned by* -0.77 meV *(blue data) from the laser and M1 cavity mode. The cavity excitation / waveguide collection scheme was used here. As this spectrum was taken with a spectrometer and CCD (as opposed to the FPI) it is not possible to resolve the RRS and SE components as they are both resolution-limited by the instrument.*

is shown for the case of cavity excitation and waveguide outcoupler collection at an excitation power of 25 nW ($\Omega_R/(2\pi) \sim 2$ GHz) in figure 6.12. An RRS fraction of 87.4 % was found at this driving strength. In this case, it is necessary to plot the intensity on a logarithmic scale for the laser background peak to be visible. Comparison of the areas of the central peaks gives a SBR of approximately 150 : 1. When the QD is resonant, weak asymmetric sidebands corresponding to emission ($dE < 0$) or absorption ($dE > 0$) of a longitudinal acoustic (LA) phonon followed by SE can be observed. For typical In(Ga)As QDs, the phonon sideband may constitute ~ 10 % of the signal [163], with the rest from the zero-phonon line (ZPL). Here, because of the cavity enhancement, the phonon sideband is reduced to ~ 5 %. The sideband could potentially be filtered using on-chip PhC filters (see chapter 8). Otherwise, for interference measurements, the total spectrum SBR will be limited by its presence, in this case to approximately 20 : 1. In the detuned case a small amount of SE from the ZPL is still observed as the QD is weakly excited via LA phonon emission [164].

Element	**Efficiency**	**Photons** (/µs)	**Notes**
Waveguide	-	11.50	
Extraction	0.14	1.610	FDTD; Amount reaching objective from outcoupler
BS	0.50	0.805	Measured
LP	0.84	0.676	Measured for co-polarized input
SM fiber	0.23	0.156	FDTD
SPAD	0.43	0.067	Quantum efficiency at QD wavelength
Total	0.0058	0.067	

TABLE 6.2. *Measurements and simulations of optical element collection and transmission efficiencies enable calculation of the waveguide brightness.*

In order to determine the brightness in the waveguide in this regime where RRS is dominant, we measured the count rate under the same conditions as those in figure 6.12. To do this, a single SPAD was connected directly to the first collection fiber, and a count rate of 66.0 ± 0.8 kHz was observed. The total system collection efficiency of 0.58 % (table 6.2) leads to an estimated waveguide count rate of 11.5 ± 0.4 MHz at this high RRS fraction. Higher count rates are possible at the sacrifice of coherence. However it should be noted that the CW driving cannot produce on-demand single photons.

6.7 Discussion and summary

Antibunched coherent scattering is a uniquely quantum effect. With QDs, it allows on-chip generation of antibunched single photons with a coherence time significantly exceeding the radiative limit of the SE process. The high photon coherence and cavity-enhanced photon emission rate renders these photons ideal for on-chip applications such as probabilistic logic gates [165, 166] and generating distant entanglement between spins [167, 168]. However, the RRS limit of $(\Omega_R)^2 \ll \gamma_1\gamma_2$ means that even if the laser is modulated to produce optically triggered single photons, the emission probability per laser pulse is $< 10\%$ [169]. On-demand operation is possible only with π-pulse excitation (see below).

Here we have observed an RRS fraction of (87.4 ± 11.1) %, with a calculated waveguide count rate of 11.5 MHz and a SBR $> 150:1$. Thus we have shown how to produce highly coherent and antibunched on-chip single photons.

The high degree of coherent scattering implies that the emitter SE coherence is close to lifetime-limited. This is achieved even though the QD is located in a H1 cavity, close to many surfaces which can negatively affect coherence. The Purcell effect has mitigated such dephasing by reducing the emission lifetime far below the timescales of the dephasing processes. In terms of QD-QD Hong-Ou-Mandel (HOM) interference, a $T_2/(2T_1)$ ratio of unity is not sufficient. The long-time coherence of the emission is also important. That is to say that the emission must remain indistinguishable for the entire time that the train of photons is produced for interference. In this regard, the high Purcell factor would also be of benefit since it increases the lifetime-limited linewidth, and therefore decreases the effect of spectral wandering. In the FPI measurements, no wandering (within the FSR) was resolvable over periods of 50 min, a time corresponding to $> 10^{14} T_1$. This is discussed further in the next chapter.

This chapter has focused on the coherent scattering from the system. Other measurements of the same device are in agreement with the conclusions. In the next chapter we meet the double π-pulse resonance fluorescence (DPRF) technique, a novel method to measure ultrashort lifetimes. That obtains a value of $T_1 = (22.7 \pm 0.9)$ ps, in agreement with the value extracted from the coherent scattering fits. Thus we have also been able to determine a value for T_1 which is at the limit of state-of-the-art detectors and methods.

In summary, coherent scattering of laser light from a QD embedded in a H1 PhCC was observed. The effect of the cavity was to reduce the excited state radiative lifetime such that the effect of pure dephasing was mitigated. In terms of coherent scattering, the QD then behaves as a lifetime-limited 2LS with a high emission rate of $1/T_1 = \sim 40$ GHz. The QD-cavity system is coupled to PhC waveguides, and the coherent scattering is guided on-chip with low background.

CHAPTER 7

A WAVEGUIDE-COUPLED QUANTUM DOT–CAVITY SYSTEM AS AN ON-CHIP SINGLE-PHOTON SOURCE

So far we have looked at the interference of photons produced when a quantum dot (QD) is excited non-resonantly (in chapter 5), and the coherent scattering that results from weak resonant excitation (chapter 6). Both of these were under continuous-wave (CW) operation. In this chapter we examine issues related to pulsed excitation and thus a QD's use as an *on-demand* single-photon source (SPS) [170–172]. We do this through simulations based on the master equation developed in section 2.2. First we look at issues which may affect the measurement of state lifetimes. We then consider resonant excitation dynamics and a novel technique to measure very short lifetimes beyond the reach of conventional methods. In doing so we discover the influence of pulse area and duration on experimental Rabi oscillations and multi-photon emission. We use the lifetime to calculate the QD-cavity parameters. Lastly we consider the coherence of the source and its relation to Hong-Ou-Mandel (HOM) interference visibility.

7.1 Sample

The sample that provides the experimental data in this chapter is the same as that in chapter 6. In fact we will be looking at the very same QD-cavity system. Again we excite with a laser spot in the region of the cavity, and collect the scattered field from either the

cavity or the outcoupler.

7.2 Lifetime of a single-photon source

In the context of single-photon generation, an important quantity of a light source is its radiative lifetime, since this determines its maximum emission rate. However, a QD is not the ideal two-level system (2LS) that we looked at in chapter 2. Like electrons in an atomic system, excitons may be excited up several discrete energy levels before reaching a quasi-continuum of states. Additionally, phonons in the solid-state environment are on hand to add or remove quanta of energy, allowing evolution through transient "virtual states". We therefore have to be careful when we talk about the lifetime of the emitter, and be clear whether we mean the lifetime of the radiative state, or the lifetime of an evolution through several states, should that be applicable.

In the previous chapter we obtained the value of T_1 through analysis of the relative contribution of coherent and incoherent scatter to the signal field. This was possible because the close to ideal $T_2/(2T_1)$ ratio made the switch between coherent and incoherent regimes obvious. In less ideal cases, this may not be so clear, and additionally we would like independent verification of the T_1. Usually T_1 is obtained through a time-resolved photoluminescence (TRPL) measurement, as in chapter 5. We will now examine this technique and some potentially confounding factors in its application.

7.2.1 TRPL with resonant and non-resonant excitation

If we excite an emitter with a short pulse, and filter the photoluminescence of a specific transition, we can obtain the TRPL curve for a single transition. In the simplest case this curve shows a mono-exponential decay with a decay constant $\tau_{\mathrm{PL}} = 1/\Gamma_{\mathrm{r}}$. With the addition of non-radiative decays the situation becomes more complex. If there is a fast non-radiative channel, so that $\Gamma_{\mathrm{nr}} \gg \Gamma_{\mathrm{r}}$, the decay may still be single-exponential with $\tau_{\mathrm{PL}} = 1/\Gamma_{\mathrm{nr}}$. This illustrates that, although we measure only radiative events, we don't necessarily only measure the radiative lifetime, and so the time-resolved measurement really probes the time-dependent occupation of the excited state.

The TRPL curve may be further modified by evolution through additional states. Figure 7.1(a) shows the TRPL curves obtained when collecting the emission at the QD wavelength, and exciting either resonantly or above the band gap of GaAs. Also shown is an ensemble measurement of QDs outside the cavity. Considering first of all the above-bandgap measurements, the lifetime is reduced inside the cavity, as expected.

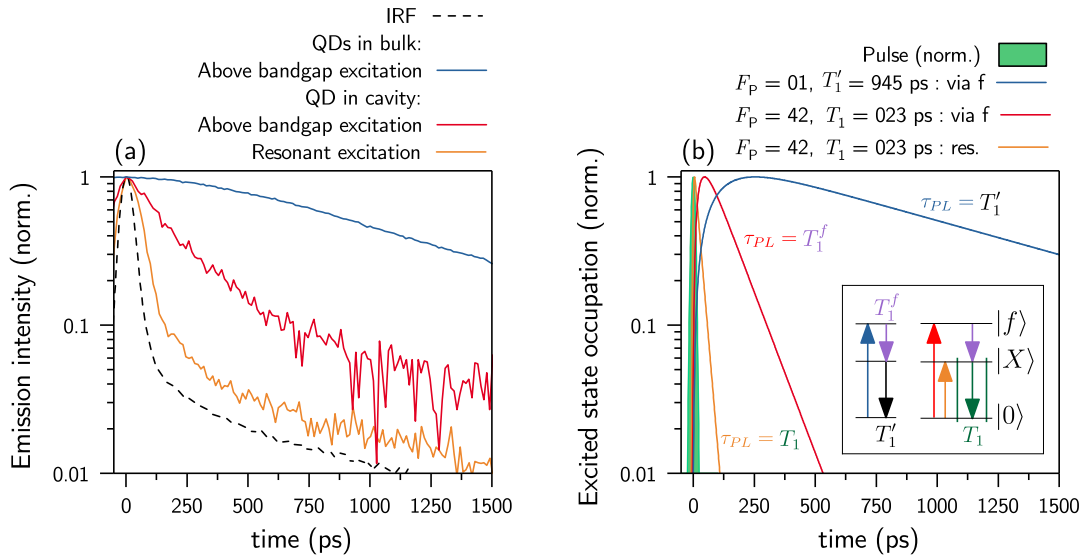

FIGURE 7.1. *(a) TRPL for different excitation energies of the QD in the cavity. A measurement of a QD ensemble outside the cavity is also shown. (b) Simulations of TRPL for a 3-level system. When exciting resonantly (orange curve), a fast rise and decay at the Purcell-enhanced rate (here* $T_1 = 23\,\text{ps}$ *with* $F_p = 42$*) is observed. For excitation via a higher energy state* $|f\rangle$ *(red curve) we see a slower rise and a decay rate of* 100 ps*, i.e. the decay rate in this case is determined by the slow filling rate of the state. If we turn off the Purcell enhancement to make the* $|X\rangle$ *decay time* 945 ps*, and again fill the state via the now relatively fast decaying third higher level (blue curve), we see a very slow rise but what we measure at long times is again the true* $|X\rangle$ *radiative decay time. Inset: Energy level diagram.*

However the decay is bi-exponential, with approximately equal decay components of time constants 100 ps and 320 ps, much longer than the T_1 determined in the previous chapter for the same QD-cavity system. Under resonant excitation, we obtain a curve close to the instrument response function (IRF). The mono-exponential decay (ignoring IRF tail) shows a convolved time constant of 46 ps, and therefore in much closer agreement to the expected T_1.

By considering a simple 3-level system—adding a state $|f\rangle$ above $|X\rangle$—we may illustrate why this occurs. The effect on the time-resolved $|X\rangle$ dynamics when exciting via this third higher energy state $|f\rangle$ is shown in figure 7.1(b). We use the master equation (2.47), but with an additional collapse operator to allow $|f\rangle \rightarrow |X\rangle$ decay at a rate $\Gamma_1^f = 1/T_1^f$, where T_1^f is the lifetime of the higher state. The excited population depends on the rate that it is filled (Γ_1^f) as well as its decay rate (Γ_1). With resonant pulses (exciting

$|0\rangle \rightarrow |X\rangle$ directly via the cavity mode), a fast rise and decay at the Purcell-enhanced rate is observed. When exciting $|X\rangle$ via $|0\rangle \rightarrow |f\rangle$ with $T_1^f > T_1$, the observed decay rate of the $|X\rangle$ population τ_{PL} is determined by the filling rate of the state, Γ_1^f, rather than the Purcell-enhanced decay rate Γ_1. For $T_1^f \ll T_1$, the TRPL curve approaches the resonant case. Also shown is the case without a cavity ($F_\mathrm{P} = 1$), which is analogous to the ensemble measurement. Since $T_1^f \ll T_1'$, the filling of the state does not significantly affect the TRPL curve.

Thus, a TRPL measurement will determine the radiative transition rate and hence Purcell factor only when the radiative rate is the slowest process in the excitation-emission cycle. If the population transfer from the excited to ground state is not the fastest process in the excitation-emission cycle, we may not be able to measure Γ_1 at all, even in the case that it arises from a mono-exponential decay. For slow filling of the excited state, the radiative emission acts as a probe for the rate at which the state is filled, and we have $\tau_\mathrm{PL} = T_1^f$, although a mono-exponential decay would again be a signature of a special case where one filling channel is dominant. This explains the observed difference in the TRPL decay rate observed under above-bandgap and resonant excitation shown in figure 7.1, in the case of slow carrier relaxation. Although we measure only radiative events, we observe the time-dependent occupation of the excited state due to all processes.

7.2.2 Resonant TRPL simulation and convolution

Having determined that the resonant excitation gives the true T_1, we can examine the resonant TRPL curve in more detail. Since the curve is comparable to the IRF, it is clear that we must deconvolve the system response. The IRF is primarily a Gaussian of width 82 ps. However in this case it cannot not be modelled as a Gaussian because the detector displays a non-negligible tail, which, while of small amplitude, has a long time constant. Therefore the master equation simulation (red curve, figure 7.1(b)) was convolved with the measured IRF obtained by using a sub-ps pulse (dashed line, figure 7.1(a)). The results of this procedure are shown in figure 7.2, and it is in good agreement with the experimental data. However this is obviously not ideal, and we would prefer not to operate so close to the limit of the detector, for reasons of both ease and accuracy of measurement, and to give more confidence in the result. In the next section we will look at resonant excitation dynamics and a new technique more suitable to this regime.

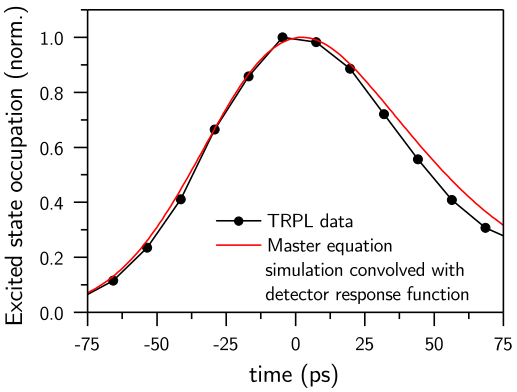

FIGURE 7.2. *TRPL data for a resonant π-pulse, and a master equation simulation of the system convolved with a measured IRF.*

7.3 Resonant dynamics

In order to investigate the new technique of double π-pulse resonance fluorescence (DPRF) it will be necessary to understand more about coherent resonant excitation, and in particular π-pulses. We will see that multiple emission events may complicate matters for non-negligible pulse durations.

7.3.1 Rabi oscillations and π-pulses

One of the features of resonant excitation is that it is a coherent excitation process. This means that the excitation field and 2LS are directly coupled such that population may transfer between the two at the coupling frequency. If the system is without loss, an initially excited 2LS will transfer all its population to the field, which will then transfer the population back to the 2LS. These oscillations are known as Rabi oscillations [173, 174]. For CW excitation, the population constantly cycles between the ground and excited states, giving a time-averaged excited population of $\frac{1}{2}$. With short pulses the field is transient, and the oscillation is turned on only for a short time. Thus we can transfer the populations to whatever state we please by controlling either the power or duration of the pulse. In other words, all pulses of equal "area" in the parameter space of intensity and duration affect the populations in an equivalent way. As we will see, this is not true for systems with finite decay. The pulse area is defined as the integral of the Rabi frequency (equation (2.24)) over time [54, p. 179]

$$\Theta = 2\frac{\mu}{\hbar}\int_{-\infty}^{\infty}\mathcal{E}(t)dt. \qquad \text{[rad]} \quad (7.1)$$

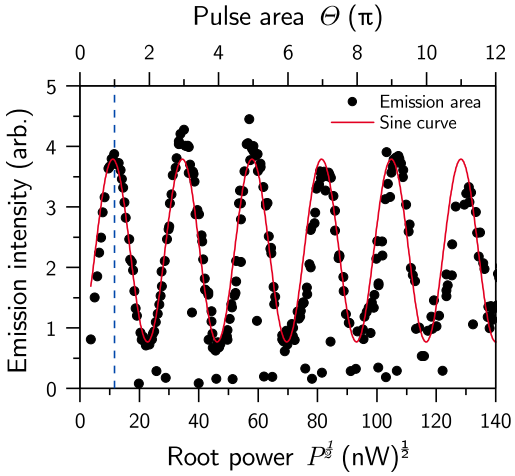

FIGURE 7.3. *Experimental Rabi oscillation showing six emission maxima and mimima.*

Its units of radians highlight that a particular pulse area causes the system to oscillate between the ground and excited states, eventually stopping at Θ radians.

An experimental pulsed Rabi oscillation is a series photoluminescence (PL) measurements for different pulse areas*. This is shown for our QD-cavity system in figure 7.3. We see that pulse areas of odd-multiples of π give maximum emission through inversion of the ground population to the excited state, perhaps multiple times. Even-multiples end the cycle with the population in the ground state. Interestingly, no excitation-induced dephasing [175] is observed even for very high areas. Now, it may be assumed that the first maximum of emission is the π-pulse in the sense of equation (7.1), i.e. under direct exciton driving, a pulse of pulse area $\Theta = \pi$ will produce this maximum of emission. If this is so, we can simulate the experimental maximum with a pulse area of π. We will show that because of the possibility of multiple emission events, this is not necessarily the case.

First let us look at what happens when we drive the 2LS with a pulse area of π for different pulse durations. This was simulated using equation (2.47) and solved via the Monte Carlo method, with the results shown in figure 7.4. P_n gives the probability that, as a result of the pulse, we will count n photons (assuming perfect detection efficiency). So P_0 means the probability that we will see zero photons, P_1 one photon, etc. We see in

*Because of the factor of 2 that appeared in equation (2.24), the pulse area to swap the populations is $\pi/2$, rather than π, as in the common terminology where the factor of 2 is not used. To avoid confusion, in this chapter all discussion and values are given in terms of the more common terminology by multiplying all Θ by 2.

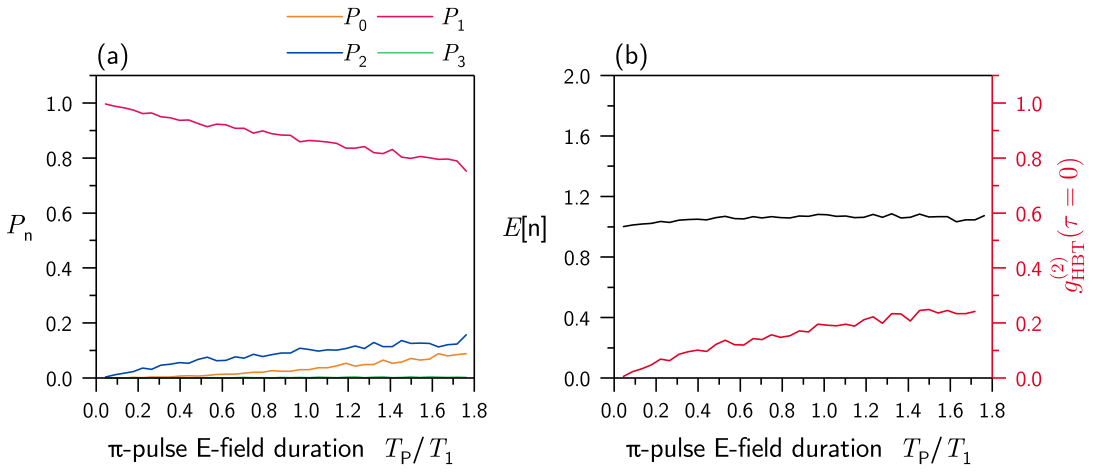

FIGURE 7.4. *Monte Carlo simulations. (a) Photocount probabilities as a function of π-pulse E-field duration T_P, given in units of T_1. As T_P increases, the emission becomes increasingly dominated by higher photon numbers. (b) Expected photocounts and $g^{(2)}_{HBT}(\tau = 0)$, as calculated from the P_n in (a).*

(a) that as the pulse gets longer, we get an increasing probability of multiple emission events per pulse. The effect of this is shown in (b) – the number of emissions per π-pulse $E[n]$ becomes greater than 1, and the $g^{(2)}_{\mathrm{HBT}}(\tau = 0)$ increases significantly, to the detriment of the SPS. $E[n]$ and $g^{(2)}_{\mathrm{HBT}}(\tau = 0)$ are calculated directly from the emission number probabilities in (a) through [176, 177]

$$E[n] = \sum_0^\infty n P_n, \tag{7.2}$$

and (recalling equation (2.9)),

$$g^{(2)}_{\mathrm{HBT}}(\tau = 0) = \frac{\sum_0^\infty n(n-1)P_n}{E[n]^2}. \tag{7.3}$$

Note that these formulae are in direct correspondence to those for Fock state photon number distributions. This correspondence is valid because for the experimental conditions, a 2-photon emission event is not distinguishable from two single-photon emissions. Now we must question whether the multiple emission events per pulse affect our analysis of experimental results. In figure 7.5, in order to see the effect clearly, we show an extreme case where the pulse duration $T_P = 1.76T_1$. P_n, $E[n]$, and $g^{(2)}_{\mathrm{HBT}}(\tau = 0)$ are plotted as before in (a) and (b), although now as a function of pulse area Θ. $E[n]$ corresponds to what would be observed in an experimental Rabi oscillation. We see several

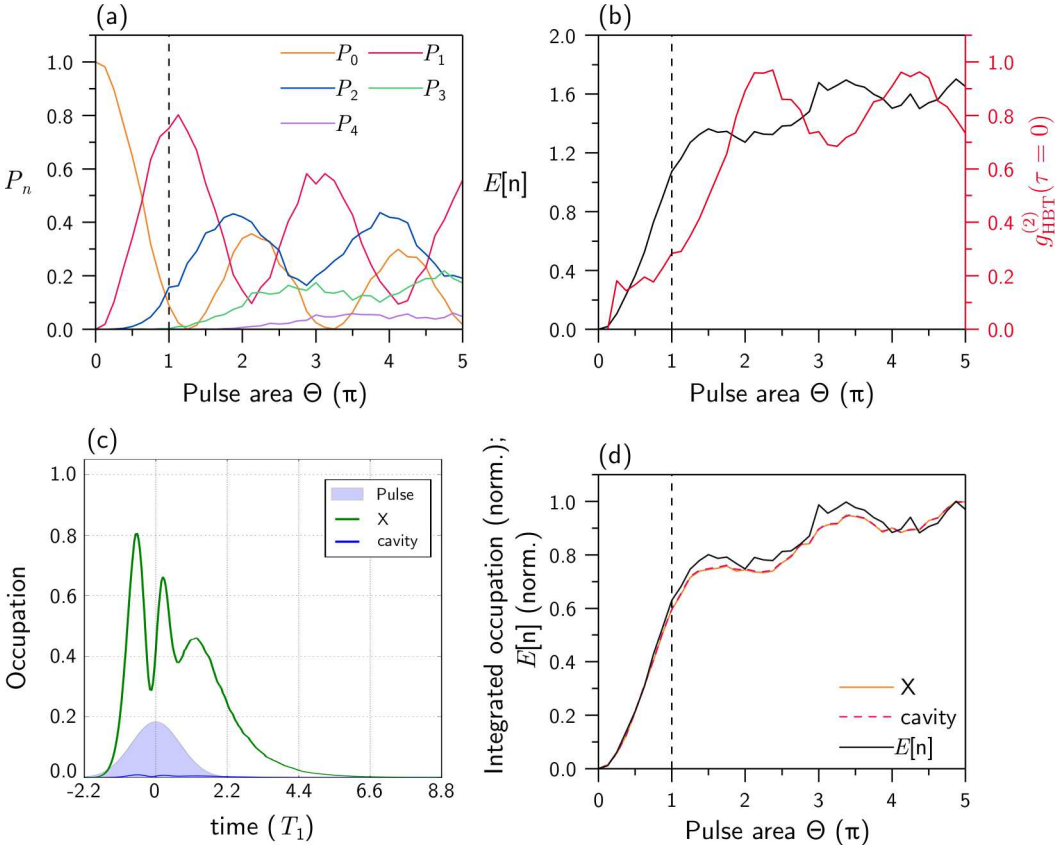

FIGURE 7.5. *Simulations with pulse duration $T_P = 1.76T_1$. (a) Emission number probabilities as a function of pulse area. (b) Expected number of photo-emissions from the system ($E[n]$), and calculated $g^{(2)}_{HBT}(\tau = 0)$. (c) Time-dependent state occupations with $\Theta = 5\pi$ (d) Normalized $E[n]$ compared to normalized integrated occupations.*

deviations from the ideal. The minima are greatly reduced, and the second maximum is greater than the first. The maxima and minima do not occur at pulse areas which are multiples of π, but are shifted to higher areas. Looking at (a), the reason for this is the increasing multiple emission probability and the divergence of the P_1 maxima from the P_0 minima. Experimentally then, for non-negligible pulse durations, it is technically incorrect to refer to the pulse power which gives the first maximum in the oscillation as the π-pulse. In (c) is shown the time-dependent occupation for the the final pulse power in (a) and (b), i.e. $\Theta = 5\pi$. The coherent population transfer cycle is visible, and is damped by the spontaneous emission of the excited state. Since in these simulations the 2LS is excited directly, it has a larger population than the cavity into which it decays. As (d) shows, integrating either the exciton or cavity populations is equivalent to calculating

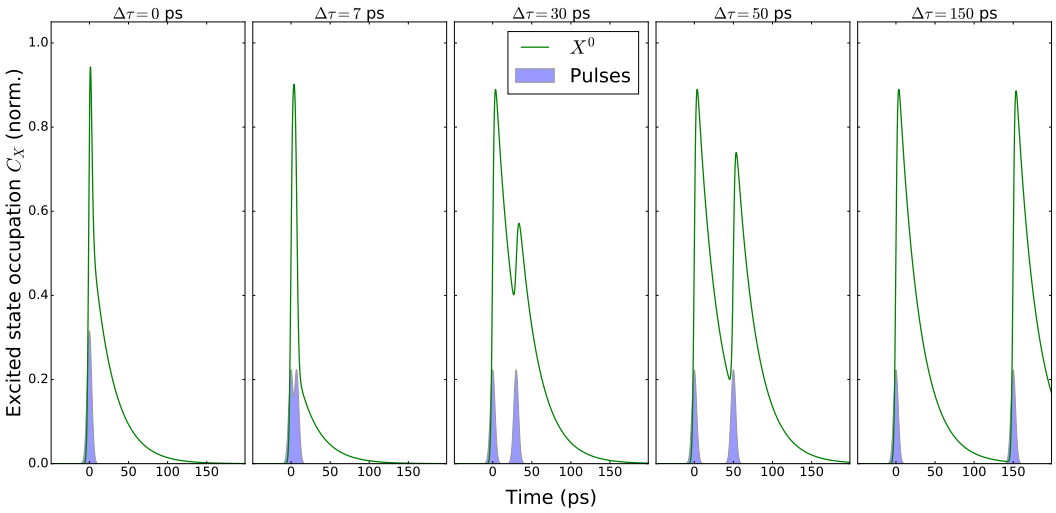

FIGURE 7.6. *The principle of the DPRF technique shown via master equation simulations of the system with two* $0.26T_1$ *π-pulses. The total occupation probability is minimum around* $\Delta t = 7$ *ps when the pulses just separate and can effectively populate and depopulate the state. The total population recovers exponentially with a time-constant given by the emitter lifetime.*

$E[n]$. In these models pure dephasing or excitation-induced dephasing was not included, since experimentally we can observe Rabi oscillations which have no dephasing (figure 7.3).

7.3.2 Double π-pulse resonance fluorescence

The very short lifetime of the QD-cavity system necessitated the development of a new high time-resolution measurement technique. This technique, DPRF, developed by Dr Alistair Brash, Dr Luis Martins, and Dr Feng Liu, is based on the coherent population transfer that we have just examined. In order to develop a clearer understanding, the technique was simulated using the master equation (2.47).

The basic principle is illustrated in figure 7.6, where the time dynamics of the excited state $|X\rangle$ are shown for several inter-pulse separations $\Delta\tau$. The first π-pulse* has the effect of moving the population of the 2LS from the ground to the excited state, where it

*For convenience we will continue to refer to the pulses which cause the first maximum in the experimental signature as π-pulses. However in all cases with π-pulse simulations, a Rabi oscillation has been simulated and the power at the first maximum taken as the π-pulse. For short pulses the discrepancy is small.

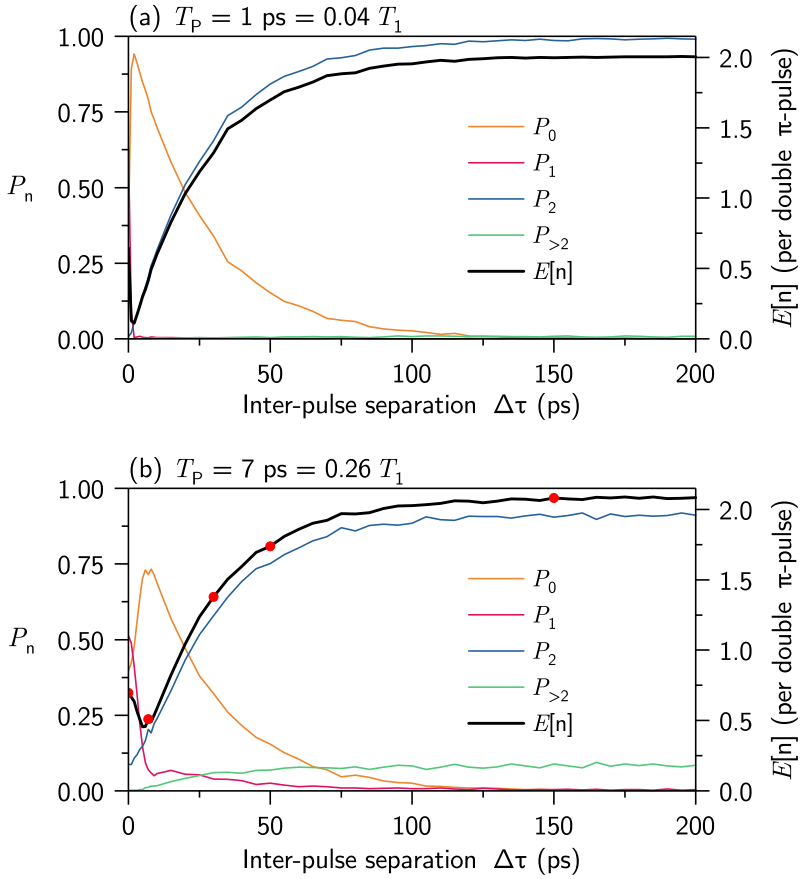

FIGURE 7.7. *Monte-Carlo simulations of the DPRF technique. The black curve shows the expected counts $E[n]$. The other curves show the composition of the expected counts in terms of emission number probabilities. The simulations reveal that the expected signal recovers on the timescale of the emitter lifetime, regardless of pulse duration. (a) The pulse duration T_P is $0.04T_1$. (b) $T_P = 0.26T_1$, and the red points refer to the pulse separations depicted in figure 7.6, which was obtained with the same parameters.*

will then decay spontaneously if left alone. A second π-pulse inverts the populations when it arrives. If we filter out the reflected excitation field, then, the intensity of the detected light will be proportional to the total population of the excited state over the course of the two pulses.

The main features of DPRF are determined by the emitter time-constant $T_1 = 1/(\Gamma_1 F_P)$, the pulse duration T_P, and the ratio of the two. The maximum instantaneous population inversion due to a single π-pulse is proportional to T_1/T_P. Thus the maximum depopulation due to the second π-pulse is also proportional to T_1/T_P, and the

point at which this occurs is determined by T_P, since at $\Delta\tau = 0$ the pulses combine to give a $\sqrt{2}\pi$-pulse. However, upon separation of the pulses, the recovery of the signal is determined only by T_1. As such, one can obtain the emitter lifetime even with $T_P > T_1$ provided one fits away from the region where the pulses overlap temporally. Experimentally, some additional noise may be seen around $\Delta t = 0$ due to interference between the pulses as they are combined in the optical setup.

Again using the Monte Carlo method, we simulate the emission number probabilities as a result of the two pulses. This is repeated for different inter-pulse separations. Figure 7.7 shows the emission number probabilities for different pulse separations and the average total number of emissions per trajectory $E[n]$. Separations indicated by red dots in (b) refer to those shown in figure 7.6. Close to $\Delta\tau = 0$, P_0 dominates, and for $\Delta\tau \gg 0$, P_2 is greatest. Except very close to zero, P_1 is very low – showing that in general the π-pulses either both create a photon each or else cancel each other out. In (a), with a very short pulse, $E[n] = 2$ for large $\Delta\tau$, as expected for two π-pulses. For the simulated pulse duration in (b), where $T_P = 0.26T_1$, there is a reasonable probability of multiple emissions for each π-pulse, and so the expected count is noticeably larger than two for large pulse separations.

Figure 7.8(a) shows the experimental result. The value obtained for T_1 is (22.7 ± 0.9) ps, in agreement with the coherent scattering value, but with less uncertainty. A simple exponential-dip fit to the experimental data is enough to extract the value. The measurement was repeated for several QD-cavity detunings, figure 7.8(b), with the dependence as expected for cavity Purcell enhancement. The π-pulse power as a function of QD-cavity detuning (not shown) has a very similar dependence, showing that there is a field enhancement for excitation as well as emission, and so is evidence that we are pumping through the cavity mode. In the next section the system parameters are further analysed.

7.4 Dipole-cavity coupling strength, position and orientation

Now that we have determined T_1, we may calculate the dipole-cavity coupling strength, position and orientation. For zero QD-cavity detuning and for perfect dipole positioning and orientation, the Purcell factor is given by equation (2.45). Q (and κ) are known from the high-power photoluminescence measurement shown in figure 6.4(a), and V_m is taken from finite-difference time-domain (FDTD) simulations approximating the real fabricated system rather than the ideal H1 value (giving 0.63 rather than 0.39 $(\lambda/n)^3$). These Q and V_m values give the ideal F_P for the fabricated cavity as 65. $\hbar g$ can then

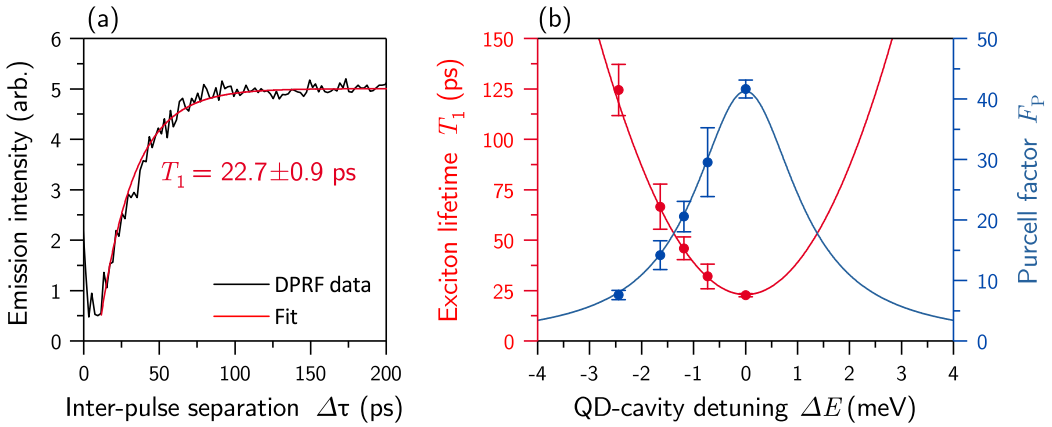

FIGURE 7.8. *(a) DPRF measurement at zero QD-cavity detuning. (b) Lifetime (and Purcell factor) dependence on QD-cavity detuning.*

be calculated to be 169 µeV for the ideal F_P (i.e. for ideal coupling), and 135 µeV for the measured QD-cavity system value of $F_P = 42$. Then, using the ensemble lifetime of QDs outside the cavity to obtain the emission rate before enhancement $\Gamma_1^b = 1/T_1^b$, and rearranging equation (2.16) to get:

$$|\vec{\mu}_{12}| = \sqrt{3\pi\hbar\varepsilon_0 \frac{\Gamma_1^b c^3}{n\omega^3}}, \qquad [\mathrm{C\,m}] \quad (7.4)$$

we obtain the QD dipole moment $|\vec{\mu}_{12}| = 27.6$ Debye. Combining with equation (2.42), and knowing that for the measured Purcell factor we have 135 µeV, where the maximum is 169 µeV, it follows that $|\vec{\epsilon}(\vec{r}_0) \cdot \vec{\mu}|^2 / |\vec{\mu}|^2 = 0.8^2$, i.e. the spatial overlap and alignment of the QD dipole and the cavity mode is $\sim 80\,\%$ ideal. This high degree of coupling is supported by both the very short lifetime (and associated relative brightness) and the very large Mollow splitting, discussed in section 6.5. The large cavity loss does however prevent the system entering the strong-coupling regime, i.e. vacuum Rabi-splitting. Recall that this occurs when equality (2.43) holds – a condition not satisfied for this g and γ until $Q > 2500$ and $F_P \sim 200$. The system thus remains in the weak coupling regime despite the large coupling strength.

In general we want $\kappa/2 > g \gg \gamma_1$ in order to obtain a highly coherent on-chip single-photon source, for the following reasons:

- $g \gg \gamma_1$ – cavity draws photon out of the system much faster than it naturally decays.

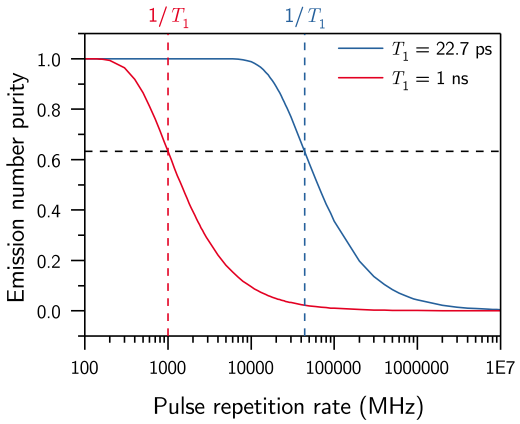

FIGURE 7.9. *Emission number purity versus pulse repetition rate under coherent excitation.*

- $\kappa/2 \ggg \gamma_1$ – cavity mode decays much much faster than the free dipole.
- $\kappa/2 > g$ – system remains weakly coupled.

When these conditions are all met, we obtain maximum extraction of coherent single-photons from the system. The spontaneous emission rate is greatly enhanced, and the photons escape the cavity rather than being trapped. We avoid the vacuum Rabi doublet and maintain a 2LS. The device reported here meets these conditions and has $\hbar\{2\kappa, g, \gamma_1\} = \{2510, 135, 0.7\}$ μeV.

7.5 Emission number purity

The double pulse simulations also highlight a point concerning emission number purity. As the blue line in figure 7.7 shows, the probability of two emissions increases with π-pulse separation on a time scale determined by the emitter lifetime. For negligibly short pulses

$$P_2 = 1 - e^{-\frac{\Delta\tau}{T_1}}. \tag{7.5}$$

For $\Delta\tau = 5T_1$ the "two-emission" purity is 99.3 %. By extension, very high emission number purity per pulse under N sequential π-pulses requires separations much longer than the emitter time constant. This therefore puts a stronger requirement on emitter lifetime for high π-pulse repetition rates. This is shown in figure 7.9 for a typical QD with lifetime 1 ns, and for this cavity-enhanced QD with lifetime 22.7 ps. While we have been considering coherent excitation, it is in general true and a consequence of the random

nature of spontaneous emission (SE). There is a limit to how much a random emission process can be made truly on-demand – but it is obvious that a higher emission rate is better.

7.6 Multi-photon emission and multiple emission events

In the above discussion on lifetimes, the average emission time was determined. For a single-photon source under CW driving we expect one photon, on average, every emission lifetime. The single-photon state is shown by a CW $g^{(2)}(\tau)$ which is zero at zero delay. Multi-photon emission is characterized by a non-zero $g^{(2)}(\tau = 0)$. However, under pulsed excitation, as is required for on-demand operation, we have seen that we may get more than one photon per pulse. This could be true even in the case that the CW $g^{(2)}(\tau = 0) = 0$, i.e. we may get multiple single-photon emission events. Therefore it is necessary to use short pulses to avoid multiple emission events*. However this may lead to other problems, as we will now discuss.

Although we approximate our pulse as monochromatic, a real pulse of finite temporal width has a finite spectral width. The *intensity* temporal FWHM Δt is related to the spectral FWHM Δf through [178]

$$\Delta t = \frac{K}{\Delta f}, \qquad \text{[s]} \quad (7.6)$$

where K is a constant that varies depending on the pulse shape. For a Gaussian pulse $K = 2\ln(2)/\pi \approx 0.441$. Experimentally then, to reduce the pulse duration, we must increase the spectral width. This means that we have a trade-off between the incident pulse's *degree of transience* D_t and its *degree of resonance* D_r with respect to the 2LS dipole. Taking $D_t = T_1/\Delta t$ and $D_r = \Delta\nu/\Delta f$, where $\Delta\nu$ is the lifetime-limited linewidth in linear frequency, we see that

$$D_t D_r = \frac{1}{4\ln(2)}. \quad (7.7)$$

Thus for a Gaussian pulse with duration equal to the emitter lifetime, so that $D_t = 1$, the spectral width is almost three times that of the emitter. If the pulse is spectrally matched to the emitter, so that $D_r = 1$, the pulse duration will be almost three times the emitter lifetime. A spectrally broad pulse may only result in a reduced excitation efficiency, however it does have the potential to increase the laser background and/or excite other unwanted states, both of which contribute photons that are detrimental to interference experiments.

*This has been confirmed by recent and ongoing measurements with this device.

In the previous chapter, the signal-to-background ratio (SBR) was seen to be very good, even in the waveguide. This is somewhat surprising, because the excitation dependence on the QD-cavity detuning described above implies we are primarily exciting through the cavity mode. As the system is weakly coupled, we should therefore expect to see many cavity photons, but we do not. Work is ongoing to understand how we can simultaneously operate in the regimes of weak coupling, cavity driving, and high SBRs.

7.7 Coherence and indistinguishability

We determined in the previous chapter that for this system $T_2/(2T_1) \sim 1$. This shows that the coherence of the emission is close to lifetime-limited, or in other words there is little *homogeneous* (Lorentzian) broadening beyond the natural linewidth. This is necessary for the production of indistinguishable photons. We have seen at the beginning of the chapter that the lifetime of the emission may be dependent on the excitation, since evolution through additional states may be slow. In fact slow relaxation will also reduce the indistinguishability of HOM interference, especially for large Purcell factors [179]. Thus for optimum indistinguishability we may require resonant excitation in addition to the cavity-enhanced radiative decay rate.

A further condition that arises in practice is that the central wavelength of emission should be stable. Changes in the charge environment can cause the line to move around in energy, a process known as spectral wandering or spectral diffusion [139–141]. This results in *inhomogeneous* (Gaussian) broadening, reducing the energy overlap of photon wavepackets, and leading to a decreased degree of interference. Spectral diffusion may also present itself by causing the absorption spectrum (section 2.2.2.5) to display a larger linewidth than the incoherent emission spectrum, even for weak driving fields.

7.8 Pulsed Hong-Ou-Mandel

The HOM interference measurement is in many ways a good test of an emitter's merit as a SPS for linear-optical quantum computing (LOQC), since it is the fundamental building block of many algorithms. More specifically we mean a pulsed HOM, since we require on-demand operation. Does an interference visibility of unity then imply an ideal SPS? In short, no. Recalling equation (1.2), the source quality is the product of the extraction efficiency per pulse, the indistinguishability, and the single-photon purity. A perfect HOM tells us nothing of the efficiency, since it is a normalized correlation function. It does tell us that the single-photon purity is ideal, and that multiple emissions do not

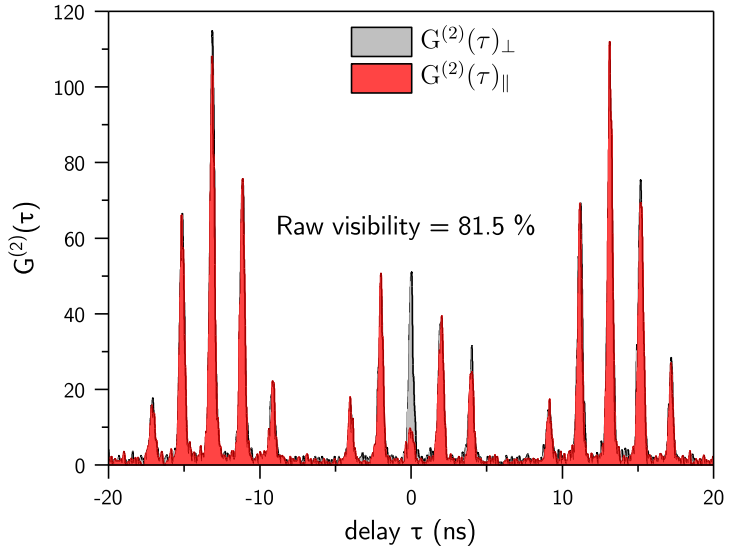

FIGURE 7.10. *Pulsed HOM with 2 ns pulse separation, every 13 ns. Obtained by Dr Alistair Brash and Catherine Phillips.*

occur during the pulse. As for the indistinguishability, the story is more complicated. While unity interference visibility implies perfect indistinguishability, it implies so only between the two photons that interfere. This means that these two photons are lifetime-limited, i.e. $T_2/(2T_1) = 1$, and indistinguishability is maintained over a time corresponding to the HOM time delay. Typically time delays might be nanoseconds, and the SPS may be subject to spectral wandering over longer timescales. Even if $T_2/(2T_1) = 1$ is maintained, photons compared over these timescales will become distinguishable in energy [61, 180–182]. Thus the HOM only tells us the degree of indistinguishability on the timescale of the experimental delay.

A pulsed HOM is shown for the QD-cavity system in figure 7.10. It is filtered at the QD wavelength (with bandwidth 55 µeV). The raw visibility is 81.5%. Correcting for interferometer imperfections we find that the (filtered) visibility at the level of the SPS is 89.4%. Accounting for multiple photon emissions [128, 183] (mostly from a non-negligible pulse duration) the visibility is $\sim 94\%$. This implies that the indistinguishability at 2 ns delay is $\sim 94\%$, and that $T_2/(2T_1) \sim 0.94$, in agreement with the value deduced from the resonant Rayleigh scattering (RRS) in the previous chapter. The filtering in this case removes the phonon sideband, which detrimentally contributes photons to the coincidence counts. It may also filter out an amount of wandering. The measurement is obtained from the outcoupler, demonstrating an on-chip, highly co-

herent, and on-demand SPS. Work is ongoing to optimize the excitation parameters in order to improve the HOM visibility, and learn more about the operation as a source of quantum fields and photons.

7.9 Conclusion

In this chapter we have looked at the QD-cavity system under pulsed excitation. We have analysed TRPL measurements and seen how complications may arise, and be solved, when determining the emission rate in this way. A new technique to measure very short lifetimes beyond conventional methods was investigated. We have simulated how multiple emission events per pulse might confound simulations and experiments and how to avoid them. Finally we have looked at the system as an on-chip, highly coherent, and on-demand SPS through a pulsed HOM. Work continues in order to optimize the experimental conditions and learn as much as possible about the system's functioning as a SPS. When this is complete, we can begin integrating the improved sources with the other circuit elements, such as the beam splitter of chapter 5. In the next chapter we look at the preliminary integration of other key components of a LOQC circuit.

CHAPTER 8

EXTENDING AND SCALING THE ON-CHIP III-V PLATFORM

So far we have looked at a number of experiments integrating on-chip sources, cavities, waveguides and beam splitters. In this chapter we will discuss preliminary work towards integrating the remaining essential components, and other efforts to improve the scalability of the platform. Firstly we look at the integration of on-chip detectors in the form of NbTiN nanowires. Then we look at the benefits of creating directional couplers in a *p-i-n* diode wafer.

8.1 Superconducting nanowire single-photon detectors

An important addition to the optical computing architecture are on-chip detectors. At present the quantum light is generally collected off chip by a lens and guided to standalone tabletop detectors. In the past these have been photo-multiplier tubes, which were superseded by single-photon avalanche diodes (SPADs), which in turn are in the process of being superseded by superconducting nanowire single-photon detectors (SNSPDs). In this section we will look at some efforts to integrate this new technology in the III-V nanobeam waveguide system.

8.1.1 NbTiN nanowire detectors

Thin films of niobium-titanium nitride (NbTiN) display type-II superconducting behaviour [184]. When such a film absorbs a photon, a small resistive hotspot forms. By

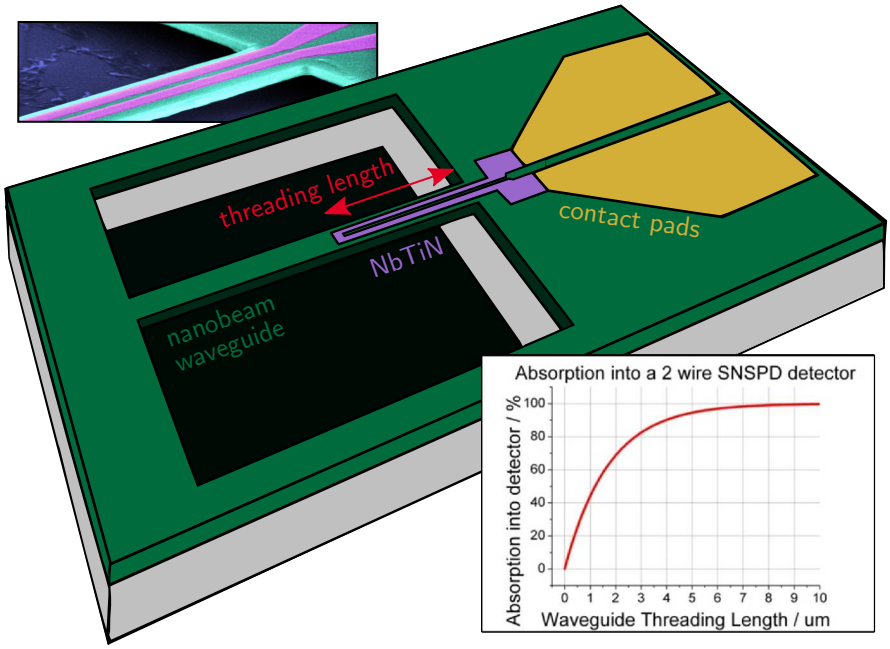

FIGURE 8.1. *A sketch of a superconducting nanowire hairpin single-photon detector on a suspended nanobeam waveguide. Bottom right: A simulation of the amount of light abosrbed from the waveguide into the detector (University of Glasgow). Top left: A colourized SEM image of a NbTiN hairpin on a GaAs waveguide.*

patterning the film into wires with nanoscale dimensions, and holding the nanowires well below the critical temperature, but just below the critical current, the hotspots trigger a sequence of events that leads to a resistive barrier across the entire width of the nanowire. The change from a superconductive to resistive state can be used to trigger an output electrical pulse, and in this way the nanowire may be used as a SNSPD [185]. The time-resolution is typically tens of picoseconds. The critical temperature of the nanowires reduces relative to the original film, but can still be above liquid helium temperatures [186], and the devices can display high efficiency at telecommunication wavelengths [187].

8.1.2 Superconducting nanowire single-photon detectors on waveguides

In our III-V architecture, light is guided along single-mode waveguides. We would like to detect this with high efficiency at the end of the circuit, rather than scatter it off chip and incur significant signal losses. For this reason the direct integration of detectors with waveguides is strongly desirable. One approach is to place a nanowire atop the

waveguide [188, 189], where absorption from the waveguide into the nanowire as the light propagates triggers detection events. Simulations indicate that a NbTiN nanowire threaded just 10 µm into a nanobeam GaAs waveguide results in approximately 100 % absorption from the waveguide mode, figure 8.1.

In collaboration with Prof. Robert Hadfield's Quantum Sensor group at the University of Glasgow, we investigated the functioning of NbTiN nanowire detectors on suspended nanobeam waveguides composed of GaAs and containing quantum dots (QDs). The wafer was grown at the National Epitaxy Facility in Sheffield and a 7 nm thick NbTiN film was deposited on top by StarCryo. The remaining steps were performed at the National Epitaxy Facility as well as at the James Watt Nanofabrication Centre in Glasgow. Several patterning-etching cycles are required – first the NbTiN is patterned and etched, then the GaAs, and finally the AlGaAs is removed. In practice the alignment of the nanowire on a waveguide presents a significant fabrication challenge. This is especially true if they are placed on thin single-mode suspended nanobeams.

An SEM image of one of the completed devices and its wafer structure is shown in figures 8.2(a) and (b). In this case the waveguides had a length of 15 µm, and a width of 500 nm to more easily align the detector and waveguide. Four devices were studied—arbitrarily labelled *North*, *East*, *South*, *West*—with two having threading lengths of 5 µm (East and South), and two having 10 µm lengths (North and West). In general the presence of the threaded nanowire caused the nanobeam to bend vertically, possibly due to strain. This was not found to alter the functioning of the waveguide or detector.

As an initial test, we looked at the optical absorption of the detectors. These measurements were performed in a flow cryostat. Instead of electrical readout, the waveguides had a grating coupler at each end. One waveguide had a nanowire, the "absorber" waveguide, and another was a normal waveguide, the "control". By exciting QDs with a HeNe laser in the region of the input coupler, as shown in figure 8.2(c), and performing a raster scan of the device, we were able to determine the amount of light that was being absorbed into the detector material. An example series of raster scans is shown in figure 8.2(d).

A 900 nm longpass filter ensures that the signal is from the QD ensemble, as shown in 8.3(a) for one waveguide. Figure 8.3(b) shows the percentage transmission through the absorber relative to the control waveguide. The values are first normalized to the signal seen at the input waveguides. For both 5 µm and 10 µm detector lengths, the transmission is between 2 and 3 %. Figure 8.3(c) shows that the signal at the input is generally slightly higher in the absorber than the control, perhaps indicating that reflection accounts for a small amount of the decreased transmission. Even allowing for

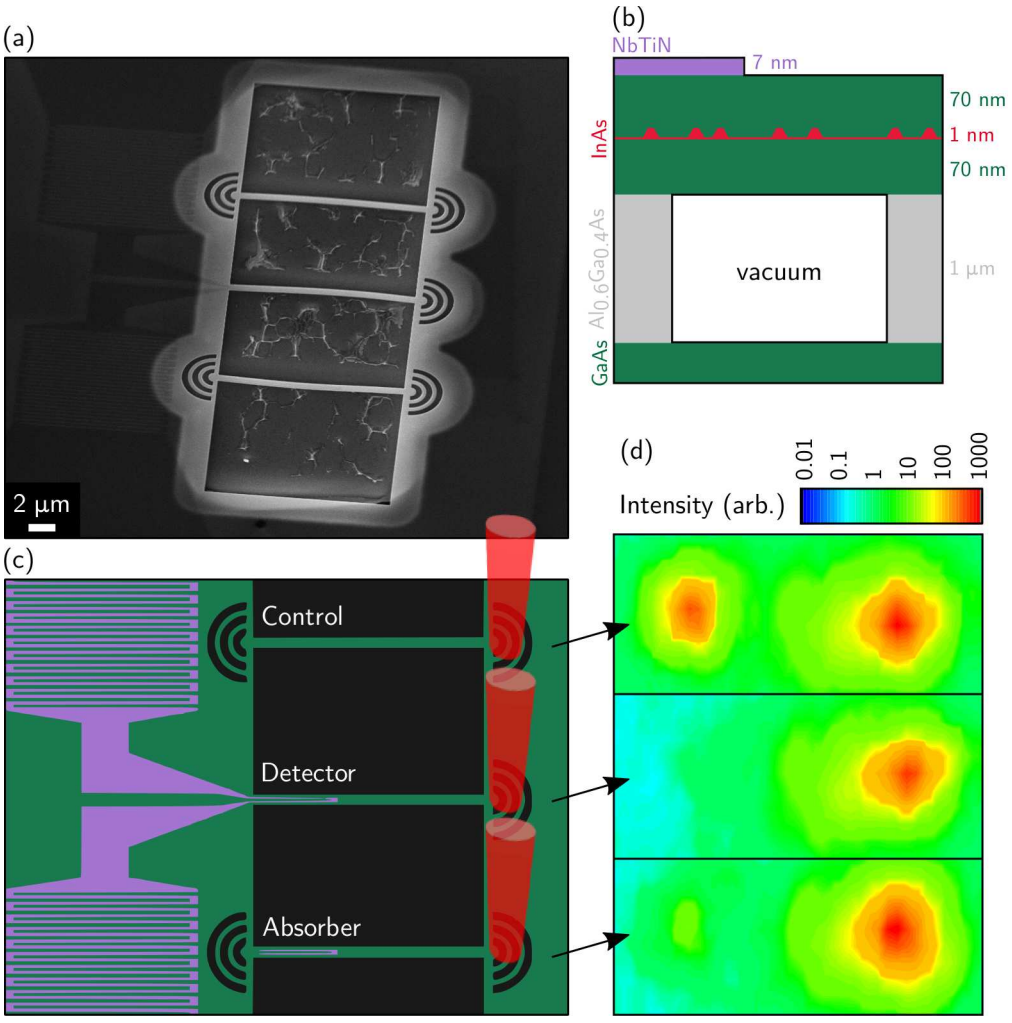

FIGURE 8.2. *(a) An SEM image of one of the devices, consisting of three waveguides, two of which have a NbTiN nanowire, and one of which is a full detector. (b) Wafer structure of the sample. (c) Sketch of a device, indicating the position of the HeNe excitation used for the raster scans. (d) QD photoluminescence raster scans of the "East" device waveguides, logarithmic scale.*

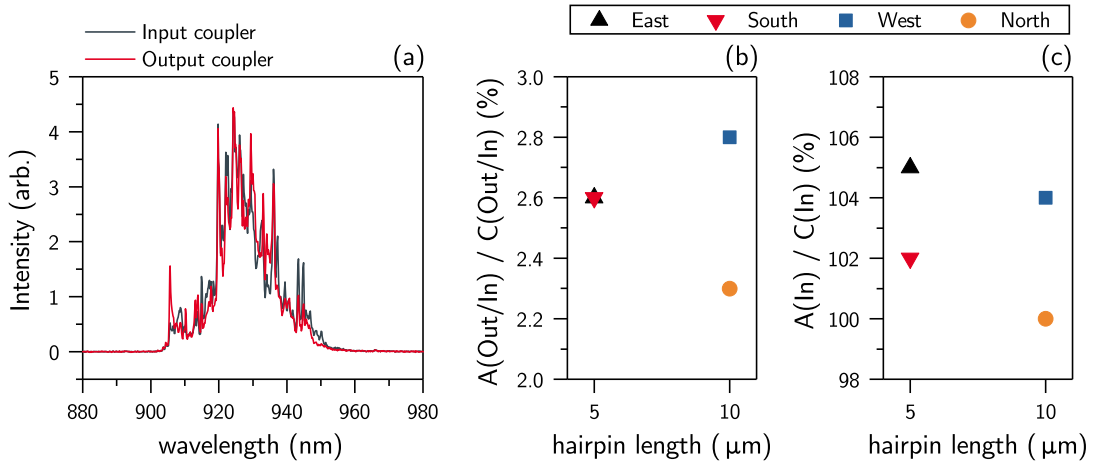

FIGURE 8.3. *(a) Spectra of the QD emission from the input and output coupler of the "control" waveguide of the East group. (b) Transmission through the "absorber" waveguides relative to their corresponding controls, after normalization of the waveguides' outputs relative to their inputs. (c) Signal at the input of the absorbers relative to the corresponding controls.*

this, the absorption is >90 %. This analysis uses the maximum values obtained in the raster scan – if integrated areas are used instead (not shown), the transmission values are virtually unchanged, falling between 2 and 3.5 %, and there is no indication of reflection within the uncertainty. The almost total absorption of the waveguide field is in good agreement with the simulations shown in 8.1. Additional measurements (not shown) with a resonant laser confirm the result, and no noticeable difference in the optical absorption is seen when comparing measurements at "4 K" and "25 K", temperatures that are at either side of the superconducting transition temperature of the NbTiN nanowire.

Not every absorbed photon will result in a detector pulse. An important figure-of-merit is the overall system detection efficiency (SDE), which in this case can be said to be given by the ratio of photons entering the waveguide to counts from the detector. In Glasgow, measurements with a laser coupled into the waveguide showed a SDE of 6.7 %, much better than SDEs obtained when coupling off-chip to tabletop detectors (cf. table 6.2).

8.1.3 Integration with directional coupler and filters

Next we were interested in utilizing the detectors in a device which would enable a fully on-chip $g^{(2)}(\tau)$ measurement. Building on the design of the device reported in chapter 5, we replaced the two output gratings with two NbTiN SNSPD detectors. The device is shown in figure 8.4(a). As before, the output arms were elongated to minimize detection of laser scatter. If the supercritical point drying step of the fabrication is successful, devices of this size should remain suspended. However, if the drying is non-ideal, or the sample is subsequently stressed for whatever reason, it helps to have additional supports. Here we used regions of photonic crystal (PhC) waveguides as supports for the nanobeams, as shown in figure 8.4(a) and (b).

In the off-chip detection system, there is typically a filter (such as a monochromator) which is used to remove light outside the spectral region of interest. Here we required an on-chip alternative. Zofia K Bishop simulated and measured nanobeam PhC cavities [190] for use as on-chip waveguide compatible filters. Such filters display a trade-off between bandwidth and transmission – a higher Q cavity will act as a narrower filter, but it will also trap and scatter more light into unwanted modes. As such, we used "three-hole" filters that had a photonic bandgap of several hundred meV, and a transmission bandwidth in the middle of this of around 5 meV – enough to isolate a single QD, but still sufficiently transmissive (around 50 %) to be able to perform correlation measurements. Any loss in transmission would be more than compensated for by the fact that we can avoid the severe losses associated with extracting light off the chip and through tabletop optics. A filter was etched into one of the input arms of each device (figure 8.4(b)). In principle one could excite the QDs non-resonantly or quasi-resonantly, and the filter will transmit only a single QD's emission through to the directional coupler and the detectors. Of course the QD needs to be sufficently spectrally isolated from the rest of the QDs, and its emission needs to be resonant with the filter.

In order to readout from the detectors, radio frequency coaxial cable ran from the outside of the insert tube down to the sample mount. The cables were then linked to the detector contact pads via gold wires (figure 8.4(c)). When cooled to $\sim$4 K, output pulses could be observed due to stray light, showing that the detectors were below the critical temperature and biased below the critical current. Unfortunately, problems with the piezostages required removing the sample, and subsequent attempts failed to recreate these conditions. It is possible that the sample degraded. It is also possible that the equilibrium temperature at the sample failed to reach $\sim$4 K, and so the superconducting transition could not be crossed. This work, while incomplete, has made steps toward

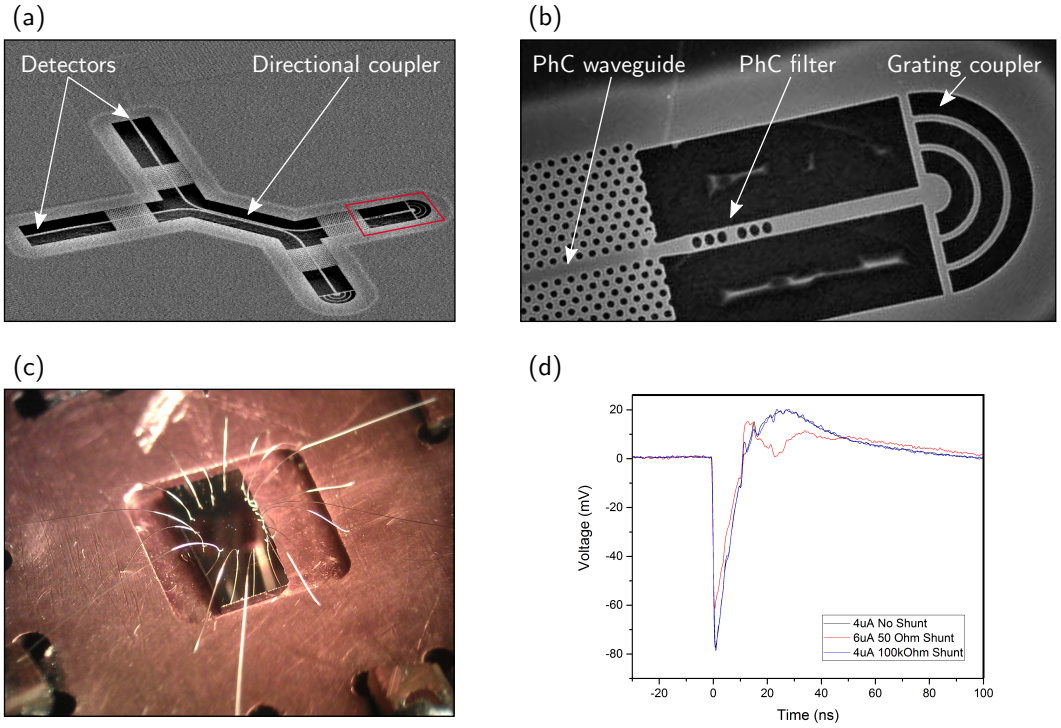

FIGURE 8.4. *(a) An SEM image of a device. (b) Zoom of region indicated by the red rectangle in (a). PhC = Photonic crystal. (c) Photo of the chip. Gold wires extend from the detectors to bond pads, which are in turn connected to radio frequency cable. (d) Averages of hundreds of output pulses from one of the detectors (University of Glasgow).*

furthering the capabilities of the GaAs suspended nanobeam architecture with integrated detectors [191].

8.2 Diode directional couplers

In this section we look at ways of evolving the directional coupler device of chapter 5 along other directions, by etching the design into a *p-i-n* wafer. This creates the possibility of electrically exciting the QDs and also the possibility of tuning the emission energy.

8.2.1 Electroluminescent single-photon source

In the measurements previously described, the single-photon source (SPS) was excited optically. A laser was focused onto the region of a single QD, and an obvious barrier

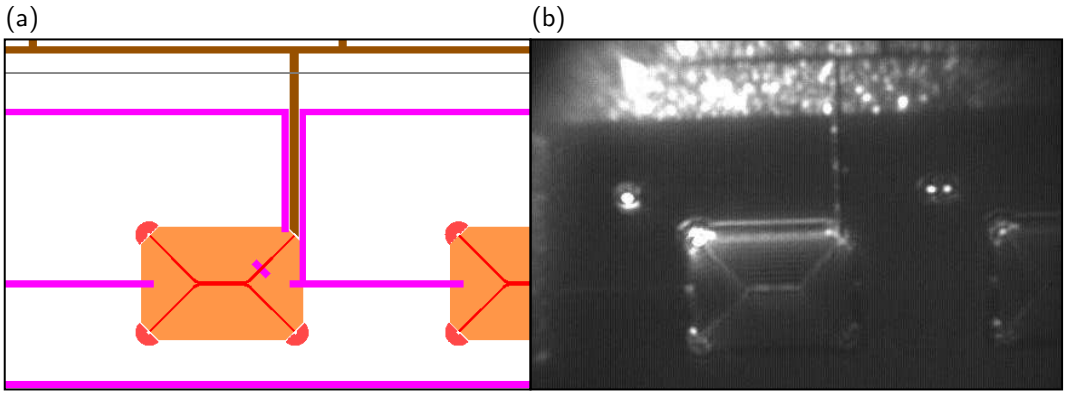

FIGURE 8.5. *(a) Design of the electroluminescent directional coupler devices. (b) Optical image of fabricated device illuminated solely by the electroluminescence.*

to scalability seems to be the need for a bulky laser and external optics for each QD. One way around this is with on-chip demultiplexing, so that one QD acts as a source for many interfering photons [148], or alternatively many QDs may be excited with on-chip microlasers [192].

Yet another possible solution is to excite the QDs electrically, where the optical emission is then referred to as electroluminescence (EL). By applying a strong field across the device, excitons are created that can fall into the potential well. It is in general much easier to excite locally in multiple locations using electrical contacts rather than optical beams, meaning many QDs dispersed across a single chip could be harnessed.

The mechanism by which the dots are usually excited is in many ways equivalent to above-bandgap optical excitation – electrons and holes flow in the conduction and valence bands of GaAs and cascade down to form the quantum dot exciton state $|X\rangle$ – and so the doorway is open to a variety of decoherence mechanisms. For this reason two-photon interference (TPI) experiments with electrical excitation, even if cavity-enhanced [193], have reported relatively low levels of interference.

However it is possible to bias devices such that resonant tunnelling occurs into single QD states [194]. So although narrow linewidths have been observed with non-resonant electrical injection [129, 195], in order to attain truly transform-limited dots it may be necessary to use (quasi-)resonant electrical excitation within a carefully designed and cleanly fabricated structure.

The electroluminescent directional coupler (DC) device was fabricated using a wafer of similar composition to that shown in figure 6.1. Working with Dominic Hallett, EL has been observed and characterization of the single-photon source and directional coupler

functionality has begun. Figure 8.5 shows the device design and an optical image of the device illuminated by its own EL.

8.2.2 Stark-tunable interference

The work in chapter 5 was presented as an iterative step towards on-chip QD-QD interference. Another forward step could be to show the same effect but via tuning of the QD through the quantum-confined Stark effect (QCSE). The tuning of the QDs is likely to be of high importance when we come to QD-QD interference, where we must overcome the variability of Stranski–Krastanov (SK) QDs. In chapters 6 and 7 we investigated a diode system, and the QD was tunable across a range of several meV, about one hundred times its linewidth. Integrating multiple independent diodes within a single device will allow the tuning of multiple QDs into resonance.

If the QDs are in relatively low-Q cavities, the Purcell enhancement may be maintained over a wide range. This is enabled by the fact that the QDs tune much further than the cavity modes for a given applied field. However this also means that the cavities may not be tuned into resonance with one another by this method. One possibility is to use gas deposition to change the cavity size, however this will not easily be implemented for multiple cavities on the same chip – without some way of isolating individual cavities they will all shift together. For this reason it will be highly desirable for the cavities to be fabricated with little variation in mode energy.

For the sample investigated in chapters 6 and 7, of 19 cavities, with and without waveguides, 11 show clear cavity modes below the longpass filter threshold of 1.3778 eV. Of these 11, the higher energy cavity polarization mode has a mean position of 1.3642 eV with an average absolute deviation from the mean of 7.0 meV. The orthogonally polarized lower energy cavity mode has a mean position of 1.3612 eV with an average absolute deviation from the mean of 7.7 meV. The separation between the two modes has a mean value of 3.8 meV with an average absolute deviation from the mean of 1.5 meV. Variation tends to correlate with spatial position, rather than for example between those with and without waveguides, suggesting that the variation is primarily due to fabrication gradients. For a cavity adjacent to the one studied in chapters 6 and 7, the mode energies differ by only 0.3 meV and 0.7 meV respectively, so that both the higher and lower polarization modes of the two adjacent cavities overlap.

It has previously been shown that it is possible to fabricate photonic crystal cavity (PhCC) samples where cavities differ on average by no more than a few meV [196]. Here we have seen that neighbouring QD–cavity systems may differ by less than the mode

linewidths, and as technology advances this consistency will no doubt become more readily achievable. The mode overlap is made less difficult by the use of relatively low-Q cavities. However, if post-fabrication cavity tuning is required, then microelectromechanical systems (MEMS) devices may be employed as a solution [197].

8.2.3 Tuning the splitting ratio

Using MEMS devices, it becomes possible to control the properties of traditionally static components such as beam splitters and filters. For the work considered here, the primary advantage of this would be in the ability to compensate for random variations or defects in fabrication. Then a beam splitter could be adjusted to the required splitting ratio, and a filter's spectral and transmissive properties may be tuned exactly to where it is needed. Additionally, one could use the devices to dynamically switch between two sources or modes.

8.3 Conclusion

In this chapter we have looked at ways of extending the III-V platform further. The inclusion of PhCs and SNSPDs can provide on-chip filters and detectors, and etched diode structures enable electrical excitation and tunability of the circuit components. This work is not yet complete, but it shows some clear paths towards the goal of on-chip linear-optical quantum computing (LOQC) in the III-V architecture.

Part III

Summary and Outlook

CHAPTER 9

SUMMARY AND OUTLOOK

In this thesis, we have looked at several experiments to increase the understanding of, and make steps towards, integrated III-V semiconductor circuits for quantum information processing. In this chapter we summarize the work, and look at what can be done in future to make further progress.

9.1 Quantum dots as single-photon sources

The key requirement for any quantum photonic circuit is a means to produce quantum states of light. As such, much of this thesis has focused on improving and demonstrating quantum dots (QDs) as on-chip sources. In chapter 6, through observation of coherent scatter and two-photon interference, we looked at how a cavity may be used to improve the coherence of the QD single-photon source (SPS). We observed a very short lifetime due to a large Purcell enhancement, and found that this greatly mitigated the effect of nanostructure related dephasing. On-demand operation was explored in chapter 7. It was seen that the lifetime may be dependent on the type of excitation used, a fact which has important implications for the coherence. Resonant excitation avoids additional states and their complications, but also introduces a greater experimental challenge. We have also seen a new technique to measure very short lifetimes beyond the range of conventional methods, and explored the effect of excitation pulse duration on key SPS properties.

9.2 Component integration

Having explored how best to create quantum states of light in a single-mode waveguide using QD and QD-cavity systems, we then want to integrate the sources with the other essential components of linear-optical quantum computing (LOQC). In chapter 5 we integrated a QD SPS with a beam splitter in the form of a directional coupler. We verified its functionality through Hanbury Brown & Twiss (HBT) measurements and on-chip interference measurements between QDs and a laser coupled into the device. Further steps towards extending the platform were detailed in chapter 8. Most ambitiously we began designing, manufacturing and testing devices that should allow completely on-chip $g^{(2)}(\tau)$ measurements. These devices consisted of QD SPSs, directional coupler beam splitters, nanobeam photonic crystal (PhC) cavity filters, and NbTiN superconducting nanowire single-photon detectors (SNSPDs).

9.3 Future work

In chapter 8 we also described some preliminary steps towards adjustable and reconfigurable III-V circuits. These could include tunable sources, tunable beam splitters, delays and filters. Having obtained valuable information on how to improve the QDs capabilities as an on-chip on-demand SPS, we can further optimize the QD-cavity system seen in chapters 6 and 7, and integrate this with the directional coupler devices of chapters 5 and 8. The device would then resemble that shown in figure 9.1(a), and be a major step towards scalable LOQC circuits, as sketched in 9.1(b).

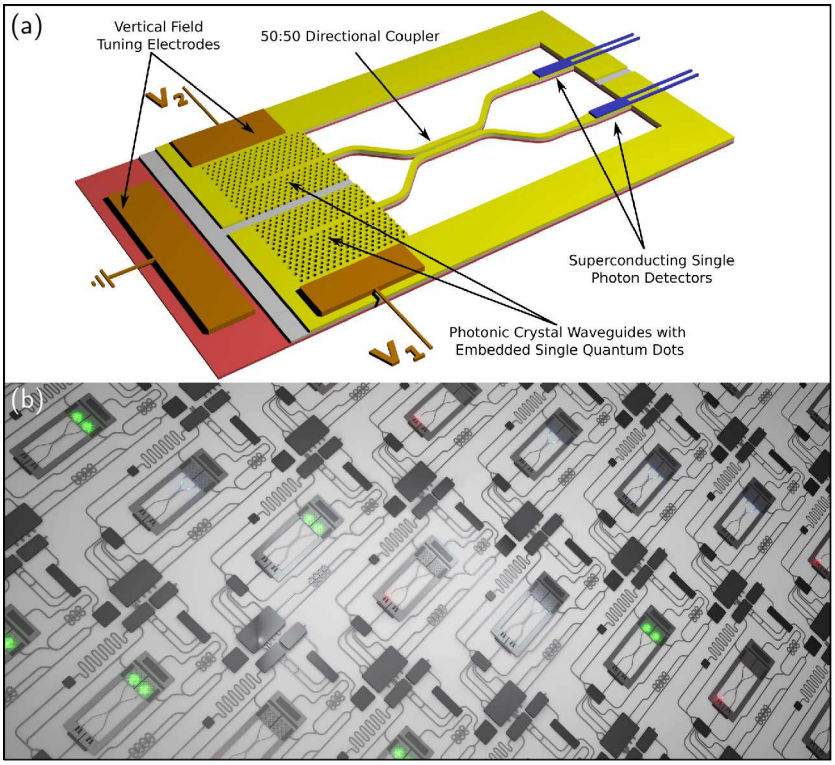

FIGURE 9.1. *(a) A model of a device that would allow fully on-chip $g^{(2)}(\tau)$ measurements to be performed (Dr Rikki Coles). (b) An artist's impression of a LOQC circuit, giving some idea of how the circuits are constructed from a high density of a few base components (23i.co.uk).*

BIBLIOGRAPHY

[1] J. S. Bell, "On the einstein podolsky rosen paradox", Physics **1**, 195–200 (1964) (cit. on p. 3).

[2] S. J. Freedman and J. F. Clauser, "Experimental test of local hidden-variable theories", Physical Review Letters **28**, 938–941 (1972) 10.1103/PhysRevLett.28.938 (cit. on p. 3).

[3] A. Aspect, P. Grangier, and G. Roger, "Experimental tests of realistic local theories via bell's theorem", Physical Review Letters **47**, 460–463 (1981) 10.1103/PhysRevLett.47.460 (cit. on p. 3).

[4] R. P. Feynman, "Simulating physics with computers", International Journal of Theoretical Physics **21**, 467–488 (1982) (cit. on pp. 3, 4).

[5] D. Deutsch, "Quantum theory, the church-turing principle and the universal quantum computer", Proceedings of the Royal Society A: Mathematical, Physical and Engineering Sciences **400**, 97–117 (1985) (cit. on p. 3).

[6] A. Peres, "Reversible logic and quantum computers", Physical Review A **32**, 3266 (1985) (cit. on p. 3).

[7] M. A. Nielsen and I. L. Chuang, *Quantum computation and quantum information*, 10th Anniversary (Cambridge University Press, Cambridge; New York, 2010) (cit. on p. 3).

[8] C. H. Bennett and D. P. DiVincenzo, "Quantum information and computation", Nature **404**, 247–255 (2000) (cit. on p. 3).

[9] D. P. DiVincenzo, "Quantum computation", Science **270**, 255–261 (1995) 10.1126/science.270.5234.255 (cit. on p. 3).

[10] I. L. Markov, "Limits on fundamental limits to computation", Nature **512**, 147–154 (2014) 10.1038/nature13570 (cit. on p. 3).

[11] J. J. L. Morton, D. R. McCamey, M. A. Eriksson, and S. A. Lyon, "Embracing the quantum limit in silicon computing", Nature **479**, 345–353 (2011) 10.1038/nature10681 (cit. on p. 4).

[12]D. Bacon and W. Van Dam, "Recent progress in quantum algorithms", Communications of the ACM **53**, 84–93 (2010) (cit. on p. 4).

[13]*A comprehensive catalog of quantum algorithms is available at the quantum algorithm zoo*, math.nist.gov/quantum/zoo/ (cit. on p. 4).

[14]P. W. Shor, "Algorithms for quantum computation: discrete logarithms and factoring", in IEEE (1994), pp. 124–134 (cit. on p. 4).

[15]E. Martín-López, A. Laing, T. Lawson, R. Alvarez, X.-Q. Zhou, and J. L. O'Brien, "Experimental realization of shor's quantum factoring algorithm using qubit recycling", Nature Photonics **6**, 773–776 (2012) 10.1038/nphoton.2012.259 (cit. on p. 4).

[16]P. Shadbolt, J. C. F. Mathews, A. Laing, and J. L. O'Brien, "Testing foundations of quantum mechanics with photons", Nature Physics **10**, 278–286 (2014) 10.1038/nphys2931 (cit. on p. 4).

[17]S. Pirandola, J. Eisert, C. Weedbrook, A. Furusawa, and S. L. Braunstein, "Advances in quantum teleportation", Nature Photonics **9**, 641–652 (2015) 10.1038/nphoton.2015.154 (cit. on p. 4).

[18]M. Arndt and K. Hornberger, "Testing the limits of quantum mechanical superpositions", Nature Physics **10**, 271–277 (2014) 10.1038/nphys2863 (cit. on p. 4).

[19]S. Boixo, T. F. Rønnow, S. V. Isakov, Z. Wang, D. Wecker, D. A. Lidar, J. M. Martinis, and M. Troyer, "Evidence for quantum annealing with more than one hundred qubits", Nature Physics **10**, 218–224 (2014) 10.1038/nphys2900 (cit. on p. 4).

[20]G. E. Santoro and E. Tosatti, "Optimization using quantum mechanics: quantum annealing through adiabatic evolution", Journal of Physics A: Mathematical and General **39**, R393–R431 (2006) 10.1088/0305-4470/39/36/R01 (cit. on p. 4).

[21]A. Das and B. Chakrabarti, "Colloquium: quantum annealing and analog quantum computation", Reviews of Modern Physics **80**, 1061–1081 (2008) 10.1103/RevModPhys.80.1061 (cit. on p. 4).

[22]U. L. Andersen, J. S. Neergaard-Nielsen, P. van Loock, and A. Furusawa, "Hybrid discrete- and continuous-variable quantum information", Nature Physics **11**, 713–719 (2015) 10.1038/nphys3410 (cit. on p. 5).

[23]T. D. Ladd, F. Jelezko, R. Laflamme, Y. Nakamura, C. Monroe, and J. L. O'Brien, "Quantum computers", Nature **464**, 45–53 (2010) 10.1038/nature08812 (cit. on p. 5).

[24]V. Vedral and M. B. Plenio, "Basics of quantum computation", Progress in Quantum Electronics **22**, 1–39 (1998) (cit. on p. 5).

[25]F. Schmidt-Kaler, H. Häffner, M. Riebe, S. Gulde, G. P. T. Lancaster, T. Deuschle, C. Becher, C. F. Roos, J. Eschner, and R. Blatt, "Realization of the cirac–zoller controlled-NOT quantum gate", Nature **422**, 408–411 (2003) 10.1038/nature01494 (cit. on p. 5).

[26]Y. Nakamura, Y. A. Pashkin, and J. S. Tsai, "Coherent control of macroscopic quantum states in a single-cooper-pair box", Nature **398**, 786–788 (1999) (cit. on p. 5).

[27]Y. Makhlin, G. Schön, and A. Shnirman, "Quantum-state engineering with josephson-junction devices", Reviews of Modern Physics **73**, 357 (2001) (cit. on p. 5).

[28]K. D. Greve, D. Press, P. L. McMahon, and Y. Yamamoto, "Ultrafast optical control of individual quantum dot spin qubits", Reports on Progress in Physics **76**, 092501 (2013) 10.1088/0034-4885/76/9/092501 (cit. on p. 5).

[29]T. E. Northup and R. Blatt, "Quantum information transfer using photons", Nature Photonics **8**, 356–363 (2014) 10.1038/nphoton.2014.53 (cit. on p. 5).

[30]D. E. Chang, V. Vuletić, and M. D. Lukin, "Quantum nonlinear optics — photon by photon", Nature Photonics **8**, 685–694 (2014) 10.1038/nphoton.2014.192 (cit. on p. 6).

[31]E. Knill, R. Laflamme, and G. J. Milburn, "A scheme for efficient quantum computation with linear optics", Nature **409**, 46–52 (2001) (cit. on p. 6).

[32]T. Ralph, N. Langford, T. Bell, and A. White, "Linear optical controlled-NOT gate in the coincidence basis", Physical Review A **65** (2002) 10.1103/PhysRevA.65.062324 (cit. on p. 6).

[33]J. L. O'Brien, G. J. Pryde, A. G. White, T. C. Ralph, and D. Branning, "Demonstration of an all-optical quantum controlled-NOT gate", Nature **426**, 264–267 (2003) 10.1038/nature02054 (cit. on p. 6).

[34]P. Kok, K. Nemoto, T. C. Ralph, J. P. Dowling, and G. J. Milburn, "Linear optical quantum computing with photonic qubits", Reviews of Modern Physics **79**, 135–174 (2007) 10.1103/RevModPhys.79.135 (cit. on p. 6).

[35]J. L. O'Brien, "Optical quantum computing", Science **318**, 1567–1570 (2007) 10.1126/science.1142892 (cit. on p. 6).

[36]P. Kok, "Photonic quantum information processing", Contemporary Physics, 1–19 (2016) 10.1080/00107514.2016.1178472 (cit. on p. 6).

[37]H. J. Briegel, D. E. Browne, W. Dür, R. Raussendorf, and M. Van den Nest, "Measurement-based quantum computation", Nature Physics, 19–26 (2009) 10.1038/nphys1157 (cit. on p. 6).

[38]Y. L. Lim, S. D. Barrett, A. Beige, P. Kok, and L. C. Kwek, "Repeat-until-success quantum computing using stationary and flying qubits", Physical Review A **73** (2006) 10.1103/PhysRevA.73.012304 (cit. on pp. 6, 43).

[39]A. Aspuru-Guzik and P. Walther, "Photonic quantum simulators", Nature Physics **8**, 285–291 (2012) 10.1038/nphys2253 (cit. on p. 6).

[40]S. Aaronson and A. Arkhipov, "The computational complexity of linear optics", in Proceedings of the forty-third annual ACM symposium on theory of computing, STOC '11 (2011), pp. 333–342, 10.1145/1993636.1993682 (cit. on p. 6).

[41]M. C. Tichy, "Interference of identical particles from entanglement to boson-sampling", Journal of Physics B: Atomic, Molecular and Optical Physics **47**, 103001 (2014) 10.1088/0953-4075/47/10/103001 (cit. on pp. 6, 17).

[42]A. Neville, C. Sparrow, R. Clifford, E. Johnston, P. M. Birchall, A. Montanaro, and A. Laing, "Classical boson sampling algorithms with superior performance to near-term experiments", Nature Physics **advance online publication** (2017) 10.1038/nphys4270 (cit. on p. 7).

[43]M. D. Eisaman, J. Fan, A. Migdall, and S. V. Polyakov, "Invited review article: single-photon sources and detectors", Review of Scientific Instruments **82**, 071101 (2011) 10.1063/1.3610677 (cit. on p. 7).

[44]E. Wolf, *Progress in optics vol. 54*, OCLC: 794443618 (Elsevier Science, Place of publication not identified, 2009) (cit. on p. 7).

[45]M. Thompson, A. Politi, J. Matthews, and J. O'Brien, "Integrated waveguide circuits for optical quantum computing", IET Circuits, Devices & Systems **5**, 94 (2011) 10.1049/iet-cds.2010.0108 (cit. on pp. 8, 34).

[46]J. Wang, A. Santamato, P. Jiang, D. Bonneau, E. Engin, J. W. Silverstone, M. Lermer, J. Beetz, M. Kamp, S. Höfling, M. G. Tanner, C. M. Natarajan, R. H. Hadfield, S. N. Dorenbos, V. Zwiller, J. L. O'Brien, and M. G. Thompson, "Gallium arsenide (GaAs) quantum photonic waveguide circuits", Optics Communications **327**, 49–55 (2014) 10.1016/j.optcom.2014.02.040 (cit. on pp. 8, 57, 58).

[47]L. Midolo, S. L. Hansen, W. Zhang, C. Papon, R. Schott, A. Ludwig, A. D. Wieck, P. Lodahl, and S. Stobbe, "Electro-optic routing of photons from single quantum dots in photonic integrated circuits", arXiv:1707.06522 [physics, physics:quant-ph] (2017) (cit. on p. 8).

[48]R. H. Hadfield, "Single-photon detectors for optical quantum information applications", Nature Photonics **3**, 696–705 (2009) 10.1038/nphoton.2009.230 (cit. on p. 9).

[49]M. Gimeno-Segovia, P. Shadbolt, D. E. Browne, and T. Rudolph, "From three-photon greenberger-horne-zeilinger states to ballistic universal quantum computation", Physical Review Letters **115** (2015) 10.1103/PhysRevLett.115.020502 (cit. on p. 9).

[50]T. Rudolph, "Why i am optimistic about the silicon-photonic route to quantum computing", APL Photonics **2**, 030901 (2017) 10.1063/1.4976737 (cit. on p. 10).

[51]J. L. O'Brien, A. Furusawa, and J. Vučković, "Photonic quantum technologies", Nature Photonics **3**, 687–695 (2009) 10.1038/nphoton.2009.229 (cit. on p. 10).

[52]J. I. Cirac and H. J. Kimble, "Quantum optics, what next?", Nature Photonics **11**, 18–20 (2017) 10.1038/nphoton.2016.259 (cit. on p. 11).

[53]H. J. Carmichael, *Statistical methods in quantum optics 1: master equations and fokker-planck equations* (Springer Berlin Heidelberg, Berlin, Heidelberg, 1999) (cit. on pp. 13, 18, 21, 24).

[54]Mark Fox, *Quantum optics: an introduction* (Oxford University Press, Oxford; New York, 2006) (cit. on pp. 13, 16, 18, 20, 36, 99).

[55]R. Hanbury Brown and R. Q. Twiss, "Correlation between photons in two coherent beams of light", Nature **177**, 27–29 (1956) 10.1038/177027a0 (cit. on p. 16).

[56]X. Zou and L. Mandel, "Photon-antibunching and sub-poissonian photon statistics", Physical Review A **41**, 475–476 (1990) 10.1103/PhysRevA.41.475 (cit. on p. 16).

[57]R. Brouri, A. Beveratos, J.-P. Poizat, and P. Grangier, "Photon antibunching in the fluorescence of individual color centers in diamond", Optics Letters **25**, 1294–1296 (2000) (cit. on p. 17).

[58]C. K. Hong, Z. Y. Ou, and L. Mandel, "Measurement of subpicosecond time intervals between two photons by interference", Physical Review Letters **59**, 2044–2046 (1987) 10.1103/PhysRevLett.59.2044 (cit. on p. 17).

[59]T. Legero, T. Wilk, A. Kuhn, and G. Rempe, "Time-resolved two-photon quantum interference", Applied Physics B: Lasers and Optics **77**, 797–802 (2003) 10.1007/s00340-003-1337-x (cit. on p. 17).

[60]T. Legero, T. Wilk, M. Hennrich, G. Rempe, and A. Kuhn, "Quantum beat of two single photons", Physical Review Letters **93** (2004) 10.1103/PhysRevLett.93.070503 (cit. on pp. 17, 70).

[61]J. Bylander, I. Robert-Philip, and I. Abram, "Interference and correlation of two independent photons", The European Physical Journal D - Atomic, Molecular and Optical Physics **22**, 295–301 (2003) 10.1140/epjd/e2002-00236-6 (cit. on pp. 17, 110).

[62]H. J. Carmichael, *Statistical methods in quantum optics 2: non-classical fields*, Statistical methods in quantum optics (Springer, Berlin, 2008), 540 pp. (cit. on pp. 18, 32).

[63]D. A. Steck, *Quantum and atom optics* (2007) (cit. on pp. 18, 19, 23).

[64]R. Loudon, *The quantum theory of light*, 3rd ed, Oxford science publications (Oxford University Press, Oxford ; New York, 2000), 438 pp. (cit. on pp. 18, 25, 27).

[65]P. Meystre and M. Sargent, *Elements of quantum optics*, 4th ed (Springer, Berlin ; New York, 2007), 507 pp. (cit. on pp. 18, 28).

[66]A. Bohm, N. L. Harshman, and H. Walther, "Relating the lorentzian and exponential: fermi's approximation, the fourier transform, and causality", Physical Review A **66**, 012107 (2002) 10.1103/PhysRevA.66.012107 (cit. on p. 20).

[67]J. M. Cassels, *Basic quantum mechanics* (Palgrave Macmillan UK, London, 1982), 10.1007/978-1-349-16671-8 (cit. on p. 25).

[68]W. Heitler, *The quantum theory of radiation*, 3rd ed (Oxford Clarendon Press, 1954) (cit. on pp. 27, 77).

[69]B. R. Mollow, "Power spectrum of light scattered by two-level systems", Physical Review **188**, 1969–1975 (1969) 10.1103/PhysRev.188.1969 (cit. on pp. 27, 77).

[70]C. Matthiesen, A. N. Vamivakas, and M. Atatüre, "Subnatural linewidth single photons from a quantum dot", Physical Review Letters **108** (2012) 10.1103/PhysRevLett.108.093602 (cit. on pp. 27, 85).

[71]A. Muller, E. B. Flagg, P. Bianucci, X. Y. Wang, D. G. Deppe, W. Ma, J. Zhang, G. J. Salamo, M. Xiao, and C. K. Shih, "Resonance fluorescence from a coherently driven semiconductor quantum dot in a cavity", Physical Review Letters **99** (2007) 10.1103/PhysRevLett.99.187402 (cit. on p. 28).

[72]A. Ulhaq, S. Weiler, C. Roy, S. M. Ulrich, M. Jetter, S. Hughes, and P. Michler, "Detuning-dependent mollow triplet of a coherently-driven single quantum dot", Optics Express **21**, 4382 (2013) 10.1364/OE.21.004382 (cit. on p. 28).

[73]J. P. Reithmaier, G. Sęk, A. Löffler, C. Hofmann, S. Kuhn, S. Reitzenstein, L. V. Keldysh, V. D. Kulakovskii, T. L. Reinecke, and A. Forchel, "Strong coupling in a single quantum dot–semiconductor microcavity system", Nature **432**, 197–200 (2004) (cit. on p. 30).

[74]E. M. Purcell, "Spontaneous emission probabilities at radio frequencies", Physical Review **69**, 681 (1946) 10.1103/PhysRev.69.674.2 (cit. on p. 30).

[75]D. Kleppner, "Inhibited spontaneous emission", Physical Review Letters **47**, 233–236 (1981) 10.1103/PhysRevLett.47.233 (cit. on p. 31).

[76]G. Gabrielse and H. Dehmelt, "Observation of inhibited spontaneous emission", Physical Review Letters **55**, 67–70 (1985) 10.1103/PhysRevLett.55.67 (cit. on p. 31).

[77]D. J. Heinzen, J. J. Childs, J. E. Thomas, and M. S. Feld, "Enhanced and inhibited visible spontaneous emission by atoms in a confocal resonator", Physical Review Letters **58**, 1320–1323 (1987) 10.1103/PhysRevLett.58.1320 (cit. on p. 31).

[78]D. Englund, D. Fattal, E. Waks, G. Solomon, B. Zhang, T. Nakaoka, Y. Arakawa, Y. Yamamoto, and J. Vučković, "Controlling the spontaneous emission rate of single quantum dots in a two-dimensional photonic crystal", Physical Review Letters **95** (2005) 10.1103/PhysRevLett.95.013904 (cit. on p. 31).

[79]G. S. Agarwal, "Vacuum-field rabi oscillations of atoms in a cavity", JOSA B **2**, 480–485 (1985) 10.1364/JOSAB.2.000480 (cit. on p. 31).

[80]H. J. Kimble, "Strong interactions of single atoms and photons in cavity QED", Physica Scripta **1998**, 127 (1998) 10.1238/Physica.Topical.076a00127 (cit. on p. 31).

[81]V. Loo, C. Arnold, O. Gazzano, A. Lemaître, I. Sagnes, O. Krebs, P. Voisin, P. Senellart, and L. Lanco, "Optical nonlinearity for few-photon pulses on a quantum dot-pillar cavity device", Physical Review Letters **109** (2012) 10.1103/PhysRevLett.109.166806 (cit. on p. 31).

[82]M. Pelton, "Modified spontaneous emission in nanophotonic structures", Nature Photonics **9**, 427–435 (2015) 10.1038/nphoton.2015.103 (cit. on p. 33).

[83]G. Khitrova, H. M. Gibbs, M. Kira, S. W. Koch, and A. Scherer, "Vacuum rabi splitting in semiconductors", Nature Physics **2**, 81–90 (2006) (cit. on p. 33).

[84]P. Lodahl, S. Mahmoodian, and S. Stobbe, "Interfacing single photons and single quantum dots with photonic nanostructures", Reviews of Modern Physics **87**, 347–400 (2015) 10.1103/RevModPhys.87.347 (cit. on p. 34).

[85]C. P. Dietrich, A. Fiore, M. G. Thompson, M. Kamp, and S. Höfling, "GaAs integrated quantum photonics: towards compact and multi-functional quantum photonic integrated circuits", Laser & Photonics Reviews **10**, 870–894 (2016) 10.1002/lpor.201500321 (cit. on p. 34).

[86]M. Bayer, G. Ortner, O. Stern, A. Kuther, A. Gorbunov, A. Forchel, P. Hawrylak, S. Fafard, K. Hinzer, T. Reinecke, S. Walck, J. Reithmaier, F. Klopf, and F. Schäfer, "Fine structure of neutral and charged excitons in self-assembled in(ga)as/(al)GaAs quantum dots", Physical Review B **65** (2002) 10.1103/PhysRevB.65.195315 (cit. on p. 36).

[87]H. Tong and M. W. Wu, "Theory of excitons in cubic III-v semiconductor GaAs, InAs and GaN quantum dots: fine structure and spin relaxation", Physical Review B **83**, 235323 (2011) 10.1103/PhysRevB.83.235323 (cit. on p. 36).

[88]J. Johansen, B. Julsgaard, S. Stobbe, J. M. Hvam, and P. Lodahl, "Probing long-lived dark excitons in self-assembled quantum dots", Physical Review B **81** (2010) 10.1103/PhysRevB.81.081304 (cit. on p. 37).

[89]Y.-H. Liao, J. I. Climente, and S.-J. Cheng, "Dominant channels of exciton spin relaxation in photoexcited self-assembled (in,ga)as quantum dots", Physical Review B **83**, 165317 (2011) 10.1103/PhysRevB.83.165317 (cit. on p. 37).

[90]H. Wei, G.-C. Guo, and L. He, "Slow exciton spin relaxation in single self-assembled ${\mathrm{in}}_{1\ensuremath{-}x}{\mathrm{ga}}_{x}\mathrm{as/GaAs}$ quantum dots", Physical Review B **89**, 245305 (2014) 10.1103/PhysRevB.89.245305 (cit. on p. 37).

[91]R. Seguin, A. Schliwa, S. Rodt, K. Pötschke, U. W. Pohl, and D. Bimberg, "Size-dependent fine-structure splitting in self-organized InAs / GaAs quantum dots", Physical Review Letters **95** (2005) 10.1103/PhysRevLett.95.257402 (cit. on p. 37).

[92]R. Seguin, A. Schliwa, T. D. Germann, S. Rodt, K. Pötschke, A. Strittmatter, U. W. Pohl, D. Bimberg, M. Winkelnkemper, T. Hammerschmidt, and P. Kratzer, "Control of fine-structure splitting and excitonic binding energies in selected individual InAs/GaAs quantum dots", Applied Physics Letters **89**, 263109 (2006) 10.1063/1.2424446 (cit. on p. 37).

[93]T. Berstermann, T. Auer, H. Kurtze, M. Schwab, D. R. Yakovlev, M. Bayer, J. Wiersig, C. Gies, F. Jahnke, D. Reuter, and A. D. Wieck, "Systematic study of carrier correlations in the electron-hole recombination dynamics of quantum dots", Physical Review B **76**, 165318 (2007) 10.1103/PhysRevB.76.165318 (cit. on p. 37).

[94]E. Moreau, I. Robert, L. Manin, V. Thierry-Mieg, J. Gérard, and I. Abram, "Quantum cascade of photons in semiconductor quantum dots", Physical Review Letters **87** (2001) 10.1103/PhysRevLett.87.183601 (cit. on p. 37).

[95]M. Müller, S. Bounouar, K. D. Jöns, M. Glässl, and P. Michler, "On-demand generation of indistinguishable polarization-entangled photon pairs", Nature Photonics **8**, 224–228 (2014) 10.1038/nphoton.2013.377 (cit. on p. 37).

[96]A. Orieux, M. A. M. Versteegh, K. D. Jöns, and S. Ducci, "Semiconductor devices for entangled photon pair generation: a review", Reports on Progress in Physics **80**, 076001 (2017) 10.1088/1361-6633/aa6955 (cit. on p. 37).

[97] Y. Benny, Y. Kodriano, E. Poem, S. Khatsevitch, D. Gershoni, and P. M. Petroff, "Two-photon photoluminescence excitation spectroscopy of single quantum dots", Physical Review B **84**, 075473 (2011) 10.1103/PhysRevB.84.075473 (cit. on p. 37).

[98] Y. Benny, Y. Kodriano, E. Poem, D. Gershoni, T. A. Truong, and P. M. Petroff, "Excitation spectroscopy of single quantum dots at tunable positive, neutral, and negative charge states", Physical Review B **86** (2012) 10.1103/PhysRevB.86.085306 (cit. on p. 37).

[99] R. Heitz, M. Grundmann, N. N. Ledentsov, L. Eckey, M. Veit, D. Bimberg, V. M. Ustinov, A. Y. Egorov, A. E. Zhukov, P. S. Kop'ev, and Z. I. Alferov, "Multiphonon-relaxation processes in self-organized InAs/GaAs quantum dots", Applied Physics Letters **68**, 361 (1996) 10.1063/1.116716 (cit. on p. 37).

[100] R. Heitz, M. Veit, N. N. Ledentsov, A. Hoffmann, D. Bimberg, V. M. Ustinov, P. S. Kop'ev, and Z. I. Alferov, "Energy relaxation by multiphonon processes in InAs/GaAs quantum dots", Physical Review B **56**, 10435 (1997) (cit. on p. 37).

[101] I. Favero, G. Cassabois, C. Voisin, C. Delalande, P. Roussignol, R. Ferreira, C. Couteau, J. Poizat, and J. Gérard, "Fast exciton spin relaxation in single quantum dots", Physical Review B **71** (2005) 10.1103/PhysRevB.71.233304 (cit. on p. 37).

[102] A. Kurzmann, B. Merkel, P. A. Labud, A. Ludwig, A. D. Wieck, A. Lorke, and M. Geller, "Optical blocking of electron tunneling into a single self-assembled quantum dot", Physical Review Letters **117**, 017401 (2016) 10.1103/PhysRevLett.117.017401 (cit. on p. 37).

[103] O. Benson, C. Santori, M. Pelton, and Y. Yamamoto, "Regulated and entangled photons from a single quantum dot", Physical Review Letters **84**, 2513 (2000) (cit. on p. 38).

[104] C. Santori, D. Fattal, M. Pelton, G. S. Solomon, and Y. Yamamoto, "Polarization-correlated photon pairs from a single quantum dot", Physical Review B **66** (2002) 10.1103/PhysRevB.66.045308 (cit. on p. 38).

[105] A. Högele, S. Seidl, M. Kroner, K. Karrai, R. J. Warburton, B. D. Gerardot, and P. M. Petroff, "Voltage-controlled optics of a quantum dot", Physical Review Letters **93** (2004) 10.1103/PhysRevLett.93.217401 (cit. on p. 38).

[106] E. Poem, Y. Kodriano, C. Tradonsky, B. D. Gerardot, P. M. Petroff, and D. Gershoni, "Radiative cascades from charged semiconductor quantum dots", Physical Review B **81** (2010) 10.1103/PhysRevB.81.085306 (cit. on p. 38).

[107]N. Prtljaga, R. J. Coles, J. OHara, B. Royall, E. Clarke, A. M. Fox, and M. S. Skolnick, "Monolithic integration of a quantum emitter with a compact on-chip beam-splitter (submission)", arXiv preprint arXiv:1404.0518 (2014) (cit. on pp. 40, 58, 59).

[108]K. D. Jöns, U. Rengstl, M. Oster, F. Hargart, M. Heldmaier, S. Bounouar, S. M. Ulrich, M. Jetter, and P. Michler, "Monolithic on-chip integration of semiconductor waveguides, beamsplitters and single-photon sources", Journal of Physics D: Applied Physics **48**, 085101 (2015) 10.1088/0022-3727/48/8/085101 (cit. on pp. 40, 58).

[109]U. Rengstl, M. Schwartz, T. Herzog, F. Hargart, M. Paul, S. L. Portalupi, M. Jetter, and P. Michler, "On-chip beamsplitter operation on single photons from quasi-resonantly excited quantum dots embedded in GaAs rib waveguides", Applied Physics Letters **107**, 021101 (2015) 10.1063/1.4926729 (cit. on p. 40).

[110]M. Notomi, "Manipulating light with strongly modulated photonic crystals", Reports on Progress in Physics **73**, 096501 (2010) 10.1088/0034-4885/73/9/096501 (cit. on p. 40).

[111]M. Notomi, A. Shinya, K. Nozaki, T. Tanabe, S. Matsuo, E. Kuramochi, T. Sato, H. Taniyama, and H. Sumikura, "Low-power nanophotonic devices based on photonic crystals towards dense photonic network on chip", IET Circuits, Devices & Systems **5**, 84 (2011) 10.1049/iet-cds.2010.0159 (cit. on p. 41).

[112]W. Bogaerts and D. Vermeulen, "Chapter 3: off-chip coupling", in *Handbook of silicon photonics*, edited by L. Vivien and L. Pavesi, Series in Optics and Optoelectronics (Taylor & Francis, Apr. 30, 2013), pp. 97–138 (cit. on p. 41).

[113]A. Faraon, I. Fushman, D. Englund, N. Stoltz, P. Petroff, and J. Vuckovic, "Dipole induced transparency in waveguide coupled photonic crystal cavities", Optics Express **16**, 12154–12162 (2008) (cit. on p. 42).

[114]W. B. Gao, A. Imamoglu, H. Bernien, and R. Hanson, "Coherent manipulation, measurement and entanglement of individual solid-state spins using optical fields", Nature Photonics **9**, 363–373 (2015) 10.1038/nphoton.2015.58 (cit. on p. 43).

[115]I. Luxmoore, N. Wasley, A. Ramsay, A. Thijssen, R. Oulton, M. Hugues, S. Kasture, V. Achanta, A. Fox, and M. Skolnick, "Interfacing spins in an InGaAs quantum dot to a semiconductor waveguide circuit using emitted photons", Physical Review Letters **110** (2013) 10.1103/PhysRevLett.110.037402 (cit. on p. 43).

[116]R. J. Coles, D. M. Price, J. E. Dixon, B. Royall, E. Clarke, P. Kok, M. S. Skolnick, A. M. Fox, and M. N. Makhonin, "Chirality of nanophotonic waveguide with embedded quantum emitter for unidirectional spin transfer", Nature Communications **7**, 11183 (2016) 10.1038/ncomms11183 (cit. on p. 43).

[117]I. Söllner, S. Mahmoodian, S. L. Hansen, L. Midolo, A. Javadi, G. Kiršanskė, T. Pregnolato, H. El-Ella, E. H. Lee, J. D. Song, S. Stobbe, and P. Lodahl, "Deterministic photon–emitter coupling in chiral photonic circuits", Nature Nanotechnology **10**, 775–778 (2015) 10.1038/nnano.2015.159 (cit. on p. 43).

[118]O. Benson, "Assembly of hybrid photonic architectures from nanophotonic constituents", Nature **480**, 193–199 (2011) 10.1038/nature10610 (cit. on p. 43).

[119]*Lumerical inc. FDTD solutions*, http://www.lumerical.com/tcad-products/fdtd/ (cit. on p. 48).

[120]*Lumerical inc. MODE solutions*, http://www.lumerical.com/tcad-products/mode (cit. on p. 48).

[121]J. R. Johansson, P. D. Nation, and F. Nori, "QuTiP: an open-source python framework for the dynamics of open quantum systems", Computer Physics Communications **183**, 1760–1772 (2012) 10.1016/j.cpc.2012.02.021 (cit. on p. 49).

[122]J. Johansson, P. Nation, and F. Nori, "QuTiP 2: a python framework for the dynamics of open quantum systems", Computer Physics Communications **184**, 1234–1240 (2013) 10.1016/j.cpc.2012.11.019 (cit. on p. 49).

[123]A. Y. Cho and J. R. Arthur, "Molecular beam epitaxy", Progress in solid state chemistry **10**, 157–191 (1975) (cit. on p. 50).

[124]B. A. Joyce, "Molecular beam epitaxy", Reports on Progress in Physics **48**, 1637–1697 (1985) 10.1088/0034-4885/48/12/002 (cit. on p. 50).

[125]F. Grazioso, B. R. Patton, and J. M. Smith, "A high stability beam-scanning confocal optical microscope for low temperature operation", Review of Scientific Instruments **81**, 093705 (2010) 10.1063/1.3484140 (cit. on p. 52).

[126]W. Becker, ed., *Advanced time-correlated single photon counting applications*, Vol. 111, Springer Series in Chemical Physics (Springer International Publishing, Cham, 2015) (cit. on p. 53).

[127]N. Prtljaga, C. Bentham, J. O'Hara, B. Royall, E. Clarke, L. R. Wilson, M. S. Skolnick, and A. M. Fox, "On-chip interference of single photons from an embedded quantum dot and an external laser", Applied Physics Letters **108**, 251101 (2016) 10.1063/1.4954220 (cit. on pp. 57, 58).

[128]C. Santori, D. Fattal, J. Vučković, G. S. Solomon, and Y. Yamamoto, "Indistinguishable photons from a single-photon device", Nature **419**, 594–597 (2002) (cit. on pp. 57, 58, 110).

[129]R. Patel, A. Bennett, K. Cooper, P. Atkinson, C. Nicoll, D. Ritchie, and A. Shields, "Postselective two-photon interference from a continuous nonclassical stream of photons emitted by a quantum dot", Physical Review Letters **100** (2008) 10.1103/PhysRevLett.100.207405 (cit. on pp. 57, 58, 120).

[130]S. Ates, S. Ulrich, S. Reitzenstein, A. Löffler, A. Forchel, and P. Michler, "Post-selected indistinguishable photons from the resonance fluorescence of a single quantum dot in a microcavity", Physical Review Letters **103** (2009) 10.1103/PhysRevLett.103.167402 (cit. on p. 57).

[131]R. B. Patel, A. J. Bennett, K. Cooper, P. Atkinson, C. A. Nicoll, D. A. Ritchie, and A. J. Shields, "Quantum interference of electrically generated single photons from a quantum dot", Nanotechnology **21**, 274011 (2010) 10.1088/0957-4484/21/27/274011 (cit. on p. 57).

[132]E. B. Flagg, A. Muller, S. V. Polyakov, A. Ling, A. Migdall, and G. S. Solomon, "Interference of single photons from two separate semiconductor quantum dots", Physical Review Letters **104** (2010) 10.1103/PhysRevLett.104.137401 (cit. on pp. 57, 58).

[133]R. B. Patel, A. J. Bennett, I. Farrer, C. A. Nicoll, D. A. Ritchie, and A. J. Shields, "Two-photon interference of the emission from electrically tunable remote quantum dots", Nature Photonics **4**, 632–635 (2010) 10.1038/nphoton.2010.161 (cit. on p. 57).

[134]S. V. Polyakov, A. Muller, E. B. Flagg, A. Ling, N. Borjemscaia, E. Van Keuren, A. Migdall, and G. S. Solomon, "Coalescence of single photons emitted by disparate single-photon sources: the example of InAs quantum dots and parametric down-conversion sources", Physical Review Letters **107** (2011) 10.1103/PhysRevLett.107.157402 (cit. on p. 57).

[135]J.-H. Kim, C. J. K. Richardson, R. P. Leavitt, and E. Waks, "Two-photon interference from the far-field emission of chip-integrated cavity-coupled emitters", Nano Letters **16**, 7061–7066 (2016) 10.1021/acs.nanolett.6b03295 (cit. on pp. 57, 58).

[136]A. J. Bennett, R. B. Patel, C. A. Nicoll, D. A. Ritchie, and A. J. Shields, "Interference of dissimilar photon sources", Nature Physics **5**, 715–717 (2009) 10.1038/nphys1373 (cit. on pp. 58, 68).

[137]R. M. Stevenson, J. Nilsson, A. J. Bennett, J. Skiba-Szymanska, I. Farrer, D. A. Ritchie, and A. J. Shields, "Quantum teleportation of laser-generated photons with an entangled-light-emitting diode", Nature Communications **4** (2013) 10.1038/ncomms3859 (cit. on pp. 58, 74).

[138]M. Felle, J. Huwer, R. M. Stevenson, J. Skiba-Szymanska, M. B. Ward, I. Farrer, R. V. Penty, D. A. Ritchie, and A. J. Shields, "Interference with a quantum dot single-photon source and a laser at telecom wavelength", Applied Physics Letters **107**, 131106 (2015) 10.1063/1.4931729 (cit. on p. 58).

[139]A. V. Kuhlmann, J. Houel, A. Ludwig, L. Greuter, D. Reuter, A. D. Wieck, M. Poggio, and R. J. Warburton, "Charge noise and spin noise in a semiconductor quantum device", Nature Physics **9**, 570–575 (2013) 10.1038/nphys2688 (cit. on pp. 62, 109).

[140]C. F. Wang, A. Badolato, I. Wilson-Rae, P. M. Petroff, E. Hu, J. Urayama, and A. Imamoğlu, "Optical properties of single InAs quantum dots in close proximity to surfaces", Applied Physics Letters **85**, 3423 (2004) 10.1063/1.1806251 (cit. on pp. 62, 109).

[141]N. Ha, T. Mano, Y.-L. Chou, Y.-N. Wu, S.-J. Cheng, J. Bocquel, P. M. Koenraad, A. Ohtake, Y. Sakuma, K. Sakoda, et al., "Size-dependent line broadening in the emission spectra of single GaAs quantum dots: impact of surface charge on spectral diffusion", Physical Review B **92**, 075306 (2015) (cit. on pp. 62, 109).

[142]C. Santori, D. Fattal, J. Vučković, G. S. Solomon, E. Waks, and Y. Yamamoto, "Sub-microsecond correlations in photoluminescence from InAs quantum dots", Physical Review B **69** (2004) 10.1103/PhysRevB.69.205324 (cit. on p. 66).

[143]M. Grundmann and D. Bimberg, "Theory of random population for quantum dots", Physical Review B **55**, 9740–9745 (1997) 10.1103/PhysRevB.55.9740 (cit. on p. 66).

[144]H. Nakajima, H. Kumano, H. Iijima, and I. Suemune, "Anomalous dip observed in intensity autocorrelation function as an inherent nature of single-photon emitters", Applied Physics Letters **101**, 161107 (2012) 10.1063/1.4760222 (cit. on p. 66).

[145]H. Nakajima, H. Kumano, H. Iijima, S. Odashima, and I. Suemune, "Carrier-transfer dynamics between neutral and charged excitonic states in a single quantum dot probed with second-order photon correlation measurements", Physical Review B **88** (2013) 10.1103/PhysRevB.88.045324 (cit. on p. 66).

[146]H. S. Nguyen, G. Sallen, M. Abbarchi, R. Ferreira, C. Voisin, P. Roussignol, G. Cassabois, and C. Diederichs, "Photoneutralization and slow capture of carriers in quantum dots probed by resonant excitation spectroscopy", Physical Review B **87**, 115305 (2013) 10.1103/PhysRevB.87.115305 (cit. on p. 66).

[147]B. H. Liu, F. W. Sun, Y. X. Gong, Y. F. Huang, Z. Y. Ou, and G. C. Guo, "Investigation of the role of indistinguishability in photon bunching and stimulated emission", Physical Review A **79** (2009) 10.1103/PhysRevA.79.053846 (cit. on p. 74).

[148]H. Wang, Y. He, Y.-H. Li, Z.-E. Su, B. Li, H.-L. Huang, X. Ding, M.-C. Chen, C. Liu, J. Qin, J.-P. Li, Y.-M. He, C. Schneider, M. Kamp, C.-Z. Peng, S. Höfling, C.-Y. Lu, and J.-W. Pan, "High-efficiency multiphoton boson sampling", Nature Photonics **11**, 361–365 (2017) 10.1038/nphoton.2017.63 (cit. on pp. 76, 120).

[149]F. Liu, A. J. Brash, J. O'Hara, L. M. P. P. Martins, C. L. Phillips, R. J. Coles, B. Royall, E. Clarke, C. Bentham, N. Prtljaga, I. E. Itskevich, L. R. Wilson, M. S. Skolnick, and A. M. Fox, "High purcell factor generation of coherent on-chip single photons", arXiv:1706.04422 [quant-ph] (2017) (cit. on p. 77).

[150]M. Shirane, S. Kono, J. Ushida, S. Ohkouchi, N. Ikeda, Y. Sugimoto, and A. Tomita, "Mode identification of high-quality-factor single-defect nanocavities in quantum dot-embedded photonic crystals", Journal of Applied Physics **101**, 073107 (2007) 10.1063/1.2714644 (cit. on pp. 77, 79).

[151]R. J. Coles, N. Prtljaga, B. Royall, I. J. Luxmoore, A. M. Fox, and M. S. Skolnick, "Waveguide-coupled photonic crystal cavity for quantum dot spin readout", Optics Express **22**, 2376 (2014) 10.1364/OE.22.002376 (cit. on pp. 77, 79).

[152]C. Bentham, I. E. Itskevich, R. J. Coles, B. Royall, E. Clarke, J. O'Hara, N. Prtljaga, A. M. Fox, M. S. Skolnick, and L. R. Wilson, "On-chip electrically controlled routing of photons from a single quantum dot", Applied Physics Letters **106**, 221101 (2015) 10.1063/1.4922041 (cit. on pp. 77, 80).

[153]J. Hagemeier, C. Bonato, T.-A. Truong, H. Kim, G. J. Beirne, M. Bakker, M. P. van Exter, Y. Luo, P. Petroff, and D. Bouwmeester, "H1 photonic crystal cavities for hybrid quantum information protocols", Optics Express **20**, 24714 (2012) 10.1364/OE.20.024714 (cit. on p. 79).

[154]A. J. Bennett, R. B. Patel, J. Skiba-Szymanska, C. A. Nicoll, I. Farrer, D. A. Ritchie, and A. J. Shields, "Giant stark effect in the emission of single semiconductor quantum dots", Applied Physics Letters **97**, 031104 (2010) 10.1063/1.3460912 (cit. on p. 79).

[155]A. Laucht, F. Hofbauer, N. Hauke, J. Angele, S. Stobbe, M. Kaniber, G. Böhm, P. Lodahl, M.-C. Amann, and J. J. Finley, "Electrical control of spontaneous emission and strong coupling for a single quantum dot", New Journal of Physics **11**, 023034 (2009) 10.1088/1367-2630/11/2/023034 (cit. on p. 79).

[156]T. B. Hoang, J. Beetz, M. Lermer, L. Midolo, M. Kamp, S. Höfling, and A. Fiore, "Widely tunable, efficient on-chip single photon sources at telecommunication wavelengths", Optics Express **20**, 21758–21765 (2012) 10.1364/OE.20.021758 (cit. on p. 79).

[157]H. S. Nguyen, G. Sallen, C. Voisin, P. Roussignol, C. Diederichs, and G. Cassabois, "Ultra-coherent single photon source", Applied Physics Letters **99**, 261904 (2011) 10.1063/1.3672034 (cit. on p. 85).

[158]R. Proux, M. Maragkou, E. Baudin, C. Voisin, P. Roussignol, and C. Diederichs, "Measuring the photon coalescence time window in the continuous-wave regime for resonantly driven semiconductor quantum dots", Physical Review Letters **114** (2015) 10.1103/PhysRevLett.114.067401 (cit. on p. 85).

[159]A. J. Bennett, J. P. Lee, D. J. P. Ellis, T. Meany, E. Murray, F. F. Floether, J. P. Griffths, I. Farrer, D. A. Ritchie, and A. J. Shields, "Cavity-enhanced coherent light scattering from a quantum dot", Science Advances **2**, e1501256–e1501256 (2016) 10.1126/sciadv.1501256 (cit. on p. 85).

[160]K. Konthasinghe, J. Walker, M. Peiris, C. K. Shih, Y. Yu, M. F. Li, J. F. He, L. J. Wang, H. Q. Ni, Z. C. Niu, and A. Muller, "Coherent versus incoherent light scattering from a quantum dot", Physical Review B **85** (2012) 10.1103/PhysRevB.85.235315 (cit. on p. 85).

[161]C. Cohen-Tannoudji, J. Dupont-Roc, and G. Grynberg, *Atom-photon interactions: basic processes and applications* (Wiley, New York, 1992), 656 pp. (cit. on p. 90).

[162]G. Wrigge, "Coherent and incoherent light scattering in the resonance fluorescence of a single molecule", PhD thesis (Diss., Eidgenössische Technische Hochschule ETH Zürich, Nr. 17684, 2008) (cit. on p. 90).

[163]A. Reigue, J. Iles-Smith, F. Lux, L. Monniello, M. Bernard, F. Margaillan, A. Lemaitre, A. Martinez, D. P. S. McCutcheon, J. Mørk, R. Hostein, and V. Voliotis, "Probing electron-phonon interaction through two-photon interference in resonantly driven semiconductor quantum dots", Physical Review Letters **118**, 233602 (2017) 10.1103/PhysRevLett.118.233602 (cit. on p. 92).

[164]J. H. Quilter, A. J. Brash, F. Liu, M. Glässl, A. M. Barth, V. M. Axt, A. J. Ramsay, M. S. Skolnick, and A. M. Fox, "Phonon-assisted population inversion of a single $\mathrm{InGaAs}/\mathrm{GaAs}$ quantum dot by pulsed laser excitation", Physical Review Letters **114**, 137401 (2015) 10.1103/PhysRevLett.114.137401 (cit. on p. 92).

[165]L.-M. Duan and R. Raussendorf, "Efficient quantum computation with probabilistic quantum gates", Physical Review Letters **95**, 080503 (2005) 10.1103/PhysRevLett.95.080503 (cit. on p. 93).

[166]L.-M. Duan, M. J. Madsen, D. L. Moehring, P. Maunz, R. N. Kohn, and C. Monroe, "Probabilistic quantum gates between remote atoms through interference of optical frequency qubits", Physical Review A **73**, 062324 (2006) 10.1103/PhysRevA.73.062324 (cit. on p. 93).

[167]C. Cabrillo, J. I. Cirac, P. García-Fernández, and P. Zoller, "Creation of entangled states of distant atoms by interference", Physical Review A **59**, 1025–1033 (1999) 10.1103/PhysRevA.59.1025 (cit. on p. 93).

[168]R. Stockill, M. J. Stanley, L. Huthmacher, E. Clarke, M. Hugues, A. J. Miller, C. Matthiesen, C. Le Gall, and M. Atatüre, "Phase-tuned entangled state generation between distant spin qubits", Physical Review Letters **119**, 010503 (2017) 10.1103/PhysRevLett.119.010503 (cit. on p. 93).

[169]C. Matthiesen, M. Geller, C. H. H. Schulte, C. L. Gall, J. Hansom, Z. Li, M. Hugues, E. Clarke, and M. Atatüre, "Phase-locked indistinguishable photons with synthesized waveforms from a solid-state source", Nature Communications **4**, ncomms2601 (2013) 10.1038/ncomms2601 (cit. on p. 93).

[170]Y.-M. He, Y. He, Y.-J. Wei, D. Wu, M. Atatüre, C. Schneider, S. Höfling, M. Kamp, C.-Y. Lu, and J.-W. Pan, "On-demand semiconductor single-photon source with near-unity indistinguishability", Nature Nanotechnology **8**, 213–217 (2013) 10.1038/nnano.2012.262 (cit. on p. 95).

[171]X. Ding, Y. He, Z.-C. Duan, N. Gregersen, M.-C. Chen, S. Unsleber, S. Maier, C. Schneider, M. Kamp, S. Höfling, et al., "On-demand single photons with high extraction efficiency and near-unity indistinguishability from a resonantly driven quantum dot in a micropillar", Physical Review Letters **116**, 020401 (2016) (cit. on p. 95).

[172]S. Unsleber, Y.-M. He, S. Gerhardt, S. Maier, C.-Y. Lu, J.-W. Pan, N. Gregersen, M. Kamp, C. Schneider, and S. Höfling, "Highly indistinguishable on-demand resonance fluorescence photons from a deterministic quantum dot micropillar device with 74% extraction efficiency", Optics Express **24**, 8539–8546 (2016) 10.1364/OE.24.008539 (cit. on p. 95).

[173]T. H. Stievater, X. Li, D. G. Steel, D. Gammon, D. S. Katzer, D. Park, C. Piermarocchi, and L. J. Sham, "Rabi oscillations of excitons in single quantum dots", Physical Review Letters **87**, 133603 (2001) 10.1103/PhysRevLett.87.133603 (cit. on p. 99).

[174]A. Zrenner, E. Beham, S. Stufler, F. Findeis, M. Bichler, and G. Abstreiter, "Coherent properties of a two-level system based on a quantum-dot photodiode", Nature **418**, 612–614 (2002) 10.1038/nature00912 (cit. on p. 99).

[175]L. Monniello, C. Tonin, R. Hostein, A. Lemaitre, A. Martinez, V. Voliotis, and R. Grousson, "Excitation-induced dephasing in a resonantly driven InAs / GaAs quantum dot", Physical Review Letters **111** (2013) 10.1103/PhysRevLett.111.026403 (cit. on p. 100).

[176]H. Carmichael, *An open systems approach to quantum optics: lectures presented at the université libre de bruxelles october 28 to november 4, 1991*, OCLC: 801006488 (Springer Berlin Heidelberg : Springer e-books, 1993) (cit. on p. 101).

[177]K. A. Fischer, L. Hanschke, J. Wierzbowski, T. Simmet, C. Dory, J. J. Finley, J. Vučković, and K. Müller, "Signatures of two-photon pulses from a quantum two-level system", Nature Physics (2017) 10.1038/nphys4052 (cit. on p. 101).

[178]A. Webster, "Useful mathematical formulas for transform limited pulses", (2012) (cit. on p. 108).

[179]A. Kiraz, M. Atatüre, and A. Imamoğlu, "Quantum-dot single-photon sources: prospects for applications in linear optics quantum-information processing", Physical Review A **69** (2004) 10.1103/PhysRevA.69.032305 (cit. on p. 109).

[180]A. Thoma, P. Schnauber, M. Gschrey, M. Seifried, J. Wolters, J.-H. Schulze, A. Strittmatter, S. Rodt, A. Carmele, A. Knorr, T. Heindel, and S. Reitzenstein, "Exploring dephasing of a solid-state quantum emitter via time- and temperature-dependent hong-ou-mandel experiments", Physical Review Letters **116**, 033601 (2016) 10.1103/PhysRevLett.116.033601 (cit. on p. 110).

[181]H. Wang, Z.-C. Duan, Y.-H. Li, S. Chen, J.-P. Li, Y.-M. He, M.-C. Chen, Y. He, X. Ding, C.-Z. Peng, C. Schneider, M. Kamp, S. Höfling, C.-Y. Lu, and J.-W. Pan, "Near-transform-limited single photons from an efficient solid-state quantum emitter", Physical Review Letters **116** (2016) 10.1103/PhysRevLett.116.213601 (cit. on p. 110).

[182]J. C. Loredo, N. A. Zakaria, N. Somaschi, C. Anton, L. de Santis, V. Giesz, T. Grange, M. A. Broome, O. Gazzano, G. Coppola, I. Sagnes, A. Lemaitre, A. Auffeves, P. Senellart, M. P. Almeida, and A. G. White, "Scalable performance in solid-state single-photon sources", Optica **3**, 433 (2016) 10.1364/OPTICA.3.000433 (cit. on p. 110).

[183]N. Somaschi, V. Giesz, L. De Santis, J. C. Loredo, M. P. Almeida, G. Hornecker, S. L. Portalupi, T. Grange, C. Antón, J. Demory, C. Gómez, I. Sagnes, N. D. Lanzillotti-Kimura, A. Lemaítre, A. Auffeves, A. G. White, L. Lanco, and P. Senellart, "Near-optimal single-photon sources in the solid state", Nature Photonics **10**, 340–345 (2016) 10.1038/nphoton.2016.23 (cit. on p. 110).

[184]R. D. Leo, A. Nigro, G. Nobile, and R. Vaglio, "Niboium-titanium nitride thin films for superconducting rf accelerator cavities", Journal of Low Temperature Physics **78**, 41–50 (1990) 10.1007/BF00682108 (cit. on p. 113).

[185]G. N. Gol'tsman, O. Okunev, G. Chulkova, A. Lipatov, A. Semenov, K. Smirnov, B. Voronov, A. Dzardanov, C. Williams, and R. Sobolewski, "Picosecond superconducting single-photon optical detector", Applied Physics Letters **79**, 705–707 (2001) 10.1063/1.1388868 (cit. on p. 114).

[186]T. Shiino, S. Shiba, N. Sakai, T. Yamakura, L. Jiang, Y. Uzawa, H. Maezawa, and S. Yamamoto, "Improvement of the critical temperature of superconducting NbTiN and NbN thin films using the AlN buffer layer", Superconductor Science and Technology **23**, 045004 (2010) 10.1088/0953-2048/23/4/045004 (cit. on p. 114).

[187]A. Divochiy, F. Marsili, D. Bitauld, A. Gaggero, R. Leoni, F. Mattioli, A. Korneev, V. Seleznev, N. Kaurova, O. Minaeva, G. Gol'tsman, K. G. Lagoudakis, M. Benkhaoul, F. Lévy, and A. Fiore, "Superconducting nanowire photon-number-resolving detector at telecommunication wavelengths", Nature Photonics **2**, 302–306 (2008) 10.1038/nphoton.2008.51 (cit. on p. 114).

[188]J. P. Sprengers, A. Gaggero, D. Sahin, S. Jahanmirinejad, G. Frucci, F. Mattioli, R. Leoni, J. Beetz, M. Lermer, M. Kamp, S. Höfling, R. Sanjines, and A. Fiore, "Waveguide superconducting single-photon detectors for integrated quantum photonic circuits", Applied Physics Letters **99**, 181110 (2011) 10.1063/1.3657518 (cit. on p. 115).

[189]G. Reithmaier, S. Lichtmannecker, T. Reichert, P. Hasch, K. Müller, M. Bichler, R. Gross, and J. J. Finley, "On-chip time resolved detection of quantum dot emission using integrated superconducting single photon detectors", Scientific Reports **3** (2013) 10.1038/srep01901 (cit. on p. 115).

[190]J. Chen, H. Haus, Shanhui Fan, P. Villeneuve, and J. Joannopoulos, "Optical filters from photonic band gap air bridges", Journal of Lightwave Technology **14**, 2575–2580 (1996) 10.1109/50.548157 (cit. on p. 118).

[191]G. Reithmaier, M. Kaniber, F. Flassig, S. Lichtmannecker, K. Müller, A. Andrejew, J. Vučković, R. Gross, and J. J. Finley, "On-chip generation, routing, and detection of resonance fluorescence", Nano Letters, 150710123855007 (2015) 10.1021/acs.nanolett.5b01444 (cit. on p. 119).

[192]P. Munnelly, T. Heindel, M. M. Karow, S. Hofling, M. Kamp, C. Schneider, and S. Reitzenstein, "A pulsed nonclassical light source driven by an integrated electrically triggered quantum dot microlaser", IEEE Journal of Selected Topics in Quantum Electronics **21**, 681–689 (2015) 10.1109/JSTQE.2015.2418219 (cit. on p. 120).

[193]A. Schlehahn, A. Thoma, P. Munnelly, M. Kamp, S. Höfling, T. Heindel, C. Schneider, and S. Reitzenstein, "An electrically driven cavity-enhanced source of indistinguishable photons with 61% overall efficiency", APL Photonics **1**, 011301 (2016) 10.1063/1.4939831 (cit. on p. 120).

[194]M. J. Conterio, N. Sköld, D. J. P. Ellis, I. Farrer, D. A. Ritchie, and A. J. Shields, "A quantum dot single photon source driven by resonant electrical injection", Applied Physics Letters **103**, 162108 (2013) 10.1063/1.4825208 (cit. on p. 120).

[195]C. Bentham, D. Hallett, N. Prtljaga, B. Royall, D. Vaitiekus, R. J. Coles, E. Clarke, A. M. Fox, M. S. Skolnick, I. E. Itskevich, and L. R. Wilson, "Single-photon electroluminescence for on-chip quantum networks", Applied Physics Letters **109**, 161101 (2016) 10.1063/1.4965295 (cit. on p. 120).

[196]A. R. A. Chalcraft, S. Lam, D. O'Brien, T. F. Krauss, M. Sahin, D. Szymanski, D. Sanvitto, R. Oulton, M. S. Skolnick, A. M. Fox, D. M. Whittaker, H.-Y. Liu, and M. Hopkinson, "Mode structure of the l3 photonic crystal cavity", Applied Physics Letters **90**, 241117 (2007) 10.1063/1.2748310 (cit. on p. 121).

[197]M. Petruzzella, T. Xia, F. Pagliano, S. Birindelli, L. Midolo, Z. Zobenica, L. H. Li, E. H. Linfield, and A. Fiore, "Fully tuneable, purcell-enhanced solid-state quantum emitters", Applied Physics Letters **107**, 141109 (2015) 10.1063/1.4932946 (cit. on p. 122).

GLOSSARY

2LS	two-level system. 18–20, 23–29, 31, 32, 36, 37, 49, 83, 85, 89, 91, 94, 96, 99, 100, 102, 103, 107, 108
BS	beam splitter. 7, 8, 10, 13, 14, 16, 17, 39, 57, 58, 62, 66, 69, 74, 76
cavQED	cavity quantum electrodynamics. 29
CCD	charge-coupled device. 54, 83
CW	continuous-wave. 56, 60, 61, 66, 70, 85, 90, 92, 95, 99, 108
DC	directional coupler. 34, 39–41, 58–60, 62, 74, 75, 120
DPRF	double π-pulse resonance fluorescence. 94, 99, 103, 104
EBL	electron beam lithography. 50
EL	electroluminescence. 43, 120
FDTD	finite-difference time-domain. 48, 105
FPI	Fabry–Pérot interferometer. 54, 74, 83–85, 87, 90, 93
FSR	free spectral range. 54, 84–86, 93
FSS	fine-structure splitting. 37, 38, 55, 61, 81, 82
FWHM	full width at half maximum. 20, 24, 28, 64

HBT Hanbury Brown & Twiss. 14–17, 62, 65, 66, 126
HOM Hong-Ou-Mandel. 10, 14, 15, 17, 18, 57, 58, 62, 68, 70, 74, 75, 93, 95, 109–111

ICP inductively coupled plasma. 50
IRF instrument response function. 86, 97–99

KLM Knill, Laflamme & Milburn. 6, 7

LA longitudinal acoustic. 91, 92
LO longitudinal optical. 54
LOQC linear-optical quantum computing. 6, 7, 9, 10, 17, 33, 34, 57, 76, 109, 111, 122, 126

MBE molecular beam epitaxy. 50, 58
MEMS microelectromechanical systems. 8, 121, 122

OPL optical path length. 8

PhC photonic crystal. 34, 41, 50, 77, 78, 91, 94, 118, 122, 126
PhCC photonic crystal cavity. 30, 34, 77, 82, 94, 121
PIC photonic integrated circuit. 6–8, 10, 33
PL photoluminescence. 24, 41, 51, 54, 55, 61, 62, 100, 105
PLE photoluminescence excitation spectroscopy. 60

QCSE quantum-confined Stark effect. 42, 79, 121
QD quantum dot. xv, 3, 6, 7, 16, 17, 29, 31, 34–38, 41–43, 47, 49, 54, 55, 57–62, 64, 66, 68, 70, 71, 74–83, 85, 91–97, 100, 103, 105–107, 110, 111, 115, 118–121, 125, 126

QED quantum electrodynamics. 3, 32, 49
QIP quantum information processing. 3, 4, 6, 7, 10, 12, 38, 43, 49, 60, 90
QuTiP quantum toolbox in python. 49

RF resonance fluorescence. 24
RIE reactive-ion etching. 50
RRS resonant Rayleigh scattering. 27, 84–88, 90–93, 110
RWA rotating-wave approximation. 23

SBR signal-to-background ratio. 85, 91, 93, 109
SDE system detection efficiency. 117
SE spontaneous emission. 24, 27, 29, 85–87, 91–93, 108
SEM scanning electron microscope. 51, 59
SK Stranski–Krastanov. 35, 37, 60, 76, 121
SNSPD superconducting nanowire single-photon detector. 34, 113, 114, 118, 122, 126
SPAD single-photon avalanche diode. 34, 54, 84, 92, 113
SPS single-photon source. 7, 9, 10, 38, 40, 56, 76, 95, 101, 109–111, 119, 125, 126

TCSPC time-correlated single-photon counting. 53, 74, 84
TE transverse electric. 59, 79
Ti:S titanium-sapphire. 60, 83
TPI two-photon interference. 17, 120
TRPL time-resolved photoluminescence. 38, 53, 54, 65, 96, 98, 111

ZPL zero-phonon line. 91